UNIVERSITY OF CALIFORNIA, SAN DIEGO

Plasmonic Colloidal Nanoantennas for Tip-Enhanced Raman Spectrocopy

A dissertation submitted in partial satisfaction of the
requirements for the degree of Doctor of Philosophy

in

NanoEngineering

by

Tyler J. Dill

Committee in charge:

Professor Andrea Tao, Chair
Professor Donald Sirbuly, Co-Chair
Professor Prabhakar Bandaru
Professor Eric Fullerton
Professor Michael Tauber

2017

The dissertation of Tyler J. Dill is approved, and it is acceptable in quality and form for publication on microfilm and electronically:

_____

_____

_____

_____

Co-Chair

_____

Chair

University of California, San Diego

2017

DEDICATION

This dissertation is dedicated to my family. They have always pushed me to think rationally and be curious about the natural world. The guidance of my parents and their own curiosity about the world has led me down my path in science, and to a career I am proud of.

EPIGRAPH

"If I have seen further, it is by standing on the shoulders of giants."
-Sir Isaac Newton

TABLE OF CONTENTS

LIST OF ABBREVIATIONS

AFM	Atomic Force Microscope
AgNCs	Silver nanocubes
AgNSs	Silver nanospheres
BCB	Brilliant cresyl blue
CNT	Carbon nanotube
dHDT	deuterated 1-hexadecanethiol
DI	deionized
DMAB	p,p'-dimercaptoazobisbenzene
EF	Enhancement factor
HDT	1-hexadecanethiol
H_2TBPP	meso-tetrakis(3,5-di-tertiarybutylphenyl)-porphyrin
IR	Infrared
LB	Langmuir-Blodgett
LSPR	Localized surface plasmon resonance
PhSH	Thiophenol
pNTP	p-nitrothiophenol
PVP	Polyvinylpyrrolidone
R6G	Rhodamine 6G
RA	Raman analyte
RBM	Radial breathing mode
SAM	Self-assembled monolayer

SEM	Scanning electron microscope
SERS	Surface-enhanced Raman spectroscopy
SFG	Sum frequency generation
SM	Single molecule
SNR	Signal-to-noise ratio
STM	Scanning tunneling microscopy
TEF	Tip-enhanced fluorescence
TERS	Tip-enhanced Raman spectroscopy
TPT	Terphenyl thiol
UV	Ultraviolet

LIST OF FIGURES

LIST OF TABLES

ACKNOWLEDGEMENTS

I would like to thank my advisor and mentor Professor Andrea Tao. Through her tireless efforts to produce the best science possible, she has made me into the scientist I am today. She always pushed me to do my best work both in the lab as well as in my writing and presentations. I have become a much stronger writer and presenter because of her. Professor Tao also gave me the freedom I needed to explore projects that interested me, while forcing me to think about why I was doing them and what my end goal was. All of her work has sculpted me into an independent researcher who can comfortably present my work in front of large audiences.

I would also like to thank Matt Rozin and Whitney Bryks for enduring alongside me the long and arduous road that is a Ph.D. Both in research and our own lives, the three of us helped push each other to always strive for better. I will never forget our years living together, sharing an office, and commuting daily. I think that we may have actually spent too much time together… I wish you guys the best in your own defenses and future careers, and sincerely hope we remain good friends.

Finally I would like to thank Stephen Palani, Darwin Zwissler, and Sam Spraker. You guys were my team, you were always interested in your work and that helped keep me excited about our progress. I wish you all the best in continuing our research and in your own futures.

Chapter 2 is a reformatted reprint in full, of the material from: **Dill, T. J.**, Rozin, M. J.; Palani, S.; Tao, A. R., Colloidal Nanoantennas for Hyperspectral

Chemical Mapping." *ACS Nano* 2016, 10 (8), 7523-7531. The dissertation author was the principal researcher and author of this paper.

Chapter 3, in full, is currently being prepared for submission for publication of the material. **Dill, T. J.**, Tao, A. R. The dissertation author was the principal researcher and author of this material.

Chapter 4, in full, is currently being prepared for submission for publication of the material. **Dill, T. J.**, Rozin, M. J., Rodarte, A. L., Brown, E. R., Palani, S., Tao, A. R. The dissertation author was the principal researcher and author of this material.

Chapter 5 is a reformatted reprint in full, of the material from: **Dill, T. J.**, Rozin, M. J., Brown, E. R., Palani, S., Tao. A. R., Investigating the Effects of Polydispersity on Gap-Mode SERS Enhancement Factors. *The Analyst* **2016**, 141 (12), 3916-3924. The dissertation author was the principal researcher and author of this paper.

Chapter 6, in full, is currently being prepared for submission for publication of the material. Dill, T. J., Rodarte, A. L., Tao, A. R. The dissertation author was the principal researcher and author of this material.

VITA

2010 Bachelor of Science, University of California, San Diego

2011 Master of Science, University of Illinois at Urbana-Champaign

2017 Doctor of Philosophy, University of California, San Diego

PUBLICATIONS

Forati, E.; Dill, T. J.; Tao, A. R.; Sievenpiper, D., Photoemission-based Microelectronic Devices. *Nature Communications* **2016,** *7*, 13399.

Dill, T. J.; Rozin, M. J.; Palani, S.; Tao, A. R., Colloidal Nanoantennas for Hyperspectral Chemical Mapping. *ACS Nano* **2016,** *10* (8), 7523-7531.

Dill, T. J.; Rozin, M. J.; Brown, E. R.; Palani, S.; Tao, A. R., Investigating the Effect of Ag Nanocube Polydispersity on Gap-Mode SERS Enhancement Factors. *Analyst* **2016,** *141* (12), 3916-3924.

Rozin, M. J.; Rosen, D. A.; Dill, T. J.; Tao, A. R., Colloidal Metasurfaces Displaying Near-Ideal and Tunable Light Absorbance in the Infrared. *Nat Communications* **2015,** *6*.

Zaretski, A. V.; Marin, B. C.; Moetazedi, H.; Dill, T. J.; Jibril, L.; Kong, C.; Tao, A. R.; Lipomi, D. J., Using the Thickness of Graphene to Template Lateral Subnanometer Gaps between Gold Nanostructures. *Nano Letters* **2015,** *15* (1), 635-640.

FIELDS OF STUDY

Major Field: NanoEngineering

Studies in colloidal synthesis, plasmonics, self-assembly, and spectroscopy

Professor Andrea Tao

ABSTRACT OF THE DISSERTATION

Plasmonic Colloidal Nanoantennas for Tip-Enhanced Raman Spectrocopy

by

Tyler J. Dill

Doctor of Philosophy in NanoEngineering

University of California, San Diego, 2017

Professor Andrea Tao, Chair

Professor Donald Sirbuly, Co-Chair

Plasmonic nanoantennas that a support localized surface plasmon resonance (LSPR) are capable of confining visible light to subwavelength dimensions due to strong electromagnetic field enhancement at the probe tip. Nanoantenna enable optical methods such as tip-enhanced Raman spectroscopy (TERS), a technique that uses

scanning probe microscopy tips to provide chemical information with nanoscale spatial resolution and single-molecule sensitivities. The LSPR supported by the probe tip is extremely sensitive to the nanoscale morphology of the nanoantenna. Control of nanoscale morphology is notoriously difficult to achieve, resulting in TERS probes with poor reproducibility. In my thesis, I demonstrate high-performance, predictable, and broadband nanospectroscopy probes that are fabricated by self-assembly. Shaped metal nanoparticles are organized into dense layers and deposited onto scanning probe tips. When coupled to a metal substrate, these probes support a strong optical resonance in the gap between the substrate and the probe, producing dramatic field enhancements. I show through experiment and electromagnetic modeling that close-packed but electrically isolated nanoparticles are electromagnetically coupled. Hybridized LSPRs supported by self-assembled nanoparticles with a broadband optical response, giving colloidal nanoantenna a high tolerance for geometric variation resulting from fabrication. I find that coupled nanoparticles act as a waveguide, transferring energy from many neighboring nanoparticles towards the active TERS apex. I also use surface-enhanced Raman spectroscopy (SERS) to characterize the effects of nanoparticle polydispersity and gap height on the Raman enhancement. These colloidal probes have consistently achieved dramatic Raman enhancements in the range of 10^8–10^9 with sub-50 nm spatial resolution. Furthermore, in contrast to other nanospectroscopy probes, these colloidal probes can be fabricated in a scalable fashion with a batch-to-batch reproducibility of ~80%. This body of work serves as an important demonstration that bottom-up engineering can be used for batch

fabricatation of high-performance and high-reliability devices using inexpensive equipment and materials.

Chapter 1

Introduction

1.1. Overview

In my thesis, I have developed new ways to assemble and utilize a class of nanoparticles for applications in optical spectroscopy, with the end goal of developing new platforms that are capable of probing the surface chemistry with single-molecule sensitivity and nanometer precision. Nanomaterials, in general, are a major impetus for technological growth; in the field of optical materials, the power to control nanostructure can lead to new ways of manipulating electromagnetic radiation.[1-7] A particularly important opportunity for nanotechnology is to enhance the spectroscopic techniques currently being used to study the properties of bulk matter and at material surfaces. Unlike microscopy, which allows for the visualization of diffraction limited physical features, spectroscopy gives additional information, about the chemical and material properties of those features. There is a long history of using spectroscopy to identify molecules and elemental composition, and to determine material structure. It is more difficult, however to apply spectroscopy to features on the nanoscale, in thin-films, wherever the numbers of molecules is small, or limited by physical dimensions. Optical spectroscopy in particular is limited by the resolution to which you can focus light. Similarly, thin-films or trace amounts of molecules or material can be difficult to detect.

I began my Ph. D. thesis work with the goal of enabling nanospectroscopy, a type of optical spectroscopy in which the spatial resolution is less than its traditional optical limit. Specifically, I focused on tip-enhanced Raman spectroscopy (TERS). TERS is a technique that has demonstrated chemical spectroscopy with < 1 nm

resolution and single-molecule detection abilities.[8-11] My goal was to develop and characterize a new type of robust optical probe, or *nanoantenna*, that would be simple to fabricate reproducibly in batches. Prior to our work, probes that could be easily fabricated had low reproducibility, [12-14] while high-performance probes required expensive vacuum equipment and could only be produced in low numbers.[15-17] Achieving this would help make TERS into a routine analytical technique that would be accessible to research groups spanning all aspects of science, engineering, and technology.

We fabricated TERS probes using chemically synthesized nanoparticle solutions. Our design eliminates the need for costly vacuum and cleanroom equipment in the fabrication process. With inexpensive equipment and chemicals, our methods allow us to fabricate batches of nanoantennas that are highly reproducible, an important goal on the way to commercialization of any technology. With these probes, we have demonstrated extraordinary enhancements of Raman signals, in addition to achieving spatial resolutions better than 40 nm. We have thoroughly studied their optical properties and understand the mechanisms for this performance, which will allow us to intelligently engineer the next generation of nanoantennas as well as nanoantennas for specific applications.

During the course of my research on TERS, we also explored surface-enhanced Raman spectroscopy (SERS). SERS operates on similar physical principles as TERS, but sacrifices spatial resolution for higher spectroscopic signals due to larger probing areas. We studied SERS because there were some analytes for which TERS

enhancements were insufficient to provide signal. But the higher spectroscopic signals originating from SERS measurements were able to provide a signal. The SERS platforms developed through my research served as a model system to explore the effects of optical resonance mode structure as well as quantum effects. We found these differences by investigating changes in nanoparticle arrangement between the TERS and SERS systems as well as between spherical and cubic nanoparticles. Although this work has not been directly translated back to TERS, we find it likely that this research has implications for the design rules of TERS probes.

Below, I provide a detailed background of TERS applications and current TERS probe fabrication methods. I also provide supporting background theory. This serves as the foundation for the bulk of my thesis research leading to the development of novel nanocrystals TERS probes.

1.2. Background

1.2.1. Raman Spectroscopy

Raman spectroscopy is a vibrational spectroscopy technique that gives information about the structures of chemicals, their orientations, and their interactions with each other and with their surroundings. Raman spectroscopy is a commonly utilized analytical technique in chemistry, biology and materials science because it provides chemistry-specific vibrational signatures of analytes,[18] is capable of operating over a large illumination wavelength range,[18] can be implemented using portable instrumentation,[19] and is well-suited to detection in aqueous environments.[20]

Raman spectroscopy examines changes in vibrational structure within an

electronic state, so-called a *virtual state*. Raman scattering occurs as a result of an induced dipole within a molecule. An incident electromagnetic field will slightly shift the position of atomic charges from equilibrium, changing the polarizability. The deformation of the charge distribution leads to an induced dipole, which resonates at the frequency of the vibrational mode, scattering Raman-shifted light. Raman scattering can be broken down into Stokes and anti-Stokes scattering processes. The Stokes process is when a photon is scattered with less energy than the exciting photon, while the anti-Stokes process produces a scattered photon with a higher energy than the exciting photon. The anti-Stokes process requires an already excited molecule, which exist in populations defined by the Boltzmann distribution. As there are generally fewer molecules in this excited state, Anti-stokes scattering is significantly weaker. A comparison of the two scattering processes can be used to provide thermodynamic information about a sample.

Raman spectroscopy can identify particular molecules through the molecular fingerprint, the set of vibrational modes unique to that particular molecule. In the vast majority of molecules and materials, there are multiple vibrational modes that are simultaneously excited. These modes represent atomic motions such as stretching, bending, rocking, twisting, and wagging, and can be symmetric or anti-symmetric. Vibrational modes can incorporate multiple atoms or entire functional groups, making them powerful tools for unique identification. As a result, Raman is used to detect analyte molecules with high specificity, and often can be implemented to do so in real-time. Raman has been important in fields as diverse as art,

archaeology, biosciences, analytical chemistry, gemology, crystallography, nanomaterials, pharmaceuticals, high-pressure science, and forensic analysis.[21]

Raman spectroscopy suffers from the inability to easily detect small numbers of molecules due to low scattering efficiencies, a key goal in analytical chemistry and materials science. Typical values for Raman scattering cross-sections are low compared to other optical processes, ranging between 10^{-31}–10^{-29} cm^2/molecule. In comparison, fluorescence cross-sections can reach as high as 10^{-16} cm^2/molecule.[20] Methods such as surface- and tip-enhanced Raman spectroscopy have been developed to increase Raman scattering by orders of magnitude.

1.2.2. Localized Surface Plasmon Resonance (LSPR)

Many TERS and SERS platforms are enabled by structures that support localized surface plasmon resonances (LSPRs). LSPR excitation occurs when incident light hitting the surface of a nanostructure, made of certain plasmonic materials, excites the nanostructure's conduction electrons into a collective oscillation. As a result, optical and electronic properties of a nanoamterial can be coupled. The coherence of electron motion leads to strong electric fields both inside and around the surface of the nanostructure. Nanostructures supporting LSPR modes have been used for refractive index sensing,[22] angstrom rulers,[23] enhanced spectroscopy,[24] and nanoscale heat sources.[25] The high-energy electrons resulting from LSPR decay have also been used as sources for catalyzing chemical reactions.[26]

LSPR modes are strongly dependent on many parameters including the size, shape, material, and surrounding environement of the plasmonic nanostructure. Only a

few metals can support a LSPR in the visible spectrum. Au, Ag, and Cu are the most commonly used in real applications, but certain other metals such as Al, Pt, and Pd can support a LSPR in the UV. LSPR modes are also strongly dependent on the size, shape, dielectric environment of the nanostructure. An important consequence of the LSPR is an increased electric-field strength near the surface, decaying exponentially from the surface of the nanostructure. The increased electric-field strength is called the near-field enhancement, and the nanoscale volumes where the near-field is highest are often referred to as hotspots.[1] When the near-field associated with multiple LSPR modes overlap, they have the potential to become coupled. The overlapping near-fields can either red-shift or blue-shift the coupled LSPR depending on the interactions of their respective near-fields. In many cases, these interacting near-fields can interact constructively and result in near-field strengths greater than those of individual nanoparticles. In surface- and tip-enhanced Raman spectroscopy, this is referred to as gap-mode sensing. As the distance between these particles decreases, the interaction strength increases. These coupled nanostructures are instrumental in high-enhancements for many LSPR-based nanoparticle applications.

1.2.3. Tip-Enhanced Raman Spectroscopy (TERS)

Tip-enhanced Raman spectroscopy (TERS), is a powerful optical technique for chemical mapping that has the potential to achieve quantitative spectroscopic analysis of arbitrary surfaces with nanoscale resolution.[27, 28] TERS combines Raman spectroscopy with scanning probe methods by using a nanoscale metal tip (supporting an LSPR) to raster a surface. Upon irradiation, the metal tip behaves like an optical

antenna to facilitate near-field amplification of both the incident and Raman-scattered light. Figure 1.1. shows a schematic of the TERS process. By scanning this tip laterally across a surface, TERS enables the point-by-point acquisition of chemical information-rich Raman spectra with spatial resolutions of a few tens of nanometers down to < 1 nm.[11, 29, 30] Unlike other optical methods that yield super-resolution images[31] or electron[32] and x-ray mapping[33] techniques, TERS is inherently label-free, non-destructive, and can be performed in ambient conditions. As such, TERS is well-suited for probing highly sensitive samples, such as single molecules,[29] nanostructures,[11, 34] and biological surfaces.[35]

TERS is generally carried out using either AFM or scanning tunneling microscopy (STM), and the TERS probes used for each are unique. In STM TERS a constant height over a surface is maintained through monitoring a tunneling current between a sharp probe tip and a conductive surface. Because the tip supports an LSPR, optical excitation can provide enhanced Raman signals originating at the tip apex.

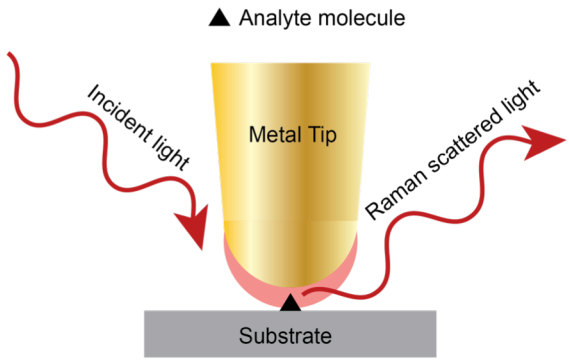

Figure 1.1. Schematic and example spectra of the TERS process. A LSPR supported by a plasmonic metal tip generates an enhanced electric near-field (red shading). The Raman analyte (black triangle) within the near-field generates enhanced Raman scattering that can then be detected. Moving the tip allows control over the origin of the TERS signal.

STM TERS offers the advantage of higher resolution, all single molecule TERS (SMTERS) studies are carried out using STM.[8] STM TERS probes tend to have a long operating lifetime as the feedback mechanism does not require physical contact with the substrate. STM TERS however requires a conductive substrate, which limits the range of samples that experiments can be carried out on.

In AFM TERS, a Au or Ag coated Si tip at the end of a cantilever is brought into contact with a surface. Mechanical deflection of the cantilever provides topographic information as the tip scans, in a similar manner to STM TERS, optical excitation provides enhanced Raman data originating from the probe apex. AFM TERS can be carried out in ambient conditions, but resolution limited to the radius of the tip. AFM TERS probes often have a radius of curvature > 10 nm in order to support a plasmonic nanostructure at the apex.[12] Because the feedback mechanism with AFM is mechanical, AFM TERS is also able to perform force spectroscopy (*i.e.* correlating forces applied to an analyte to their corresponding chemical spectra).[36] AFM TERS tips tend to have reduced lifetimes as plasmonic metals are often soft and wear down on extended contact. Mechanical wear can be addressed with hard oxide coatings over the plasmonic layer at the expense of a fraction of the Raman enhancement.[37]

In order to acquire chemical images of small numbers of molecules, TERS probes must greatly enhance the amount of Raman scattering from each molecule. The Raman enhancement factor (EF) is defined as the increase in Raman scattering from the plasmonic near-field as well as any chemical enhancements compared to the

Raman scattering from a neat sample. Both the exciting and Raman scattered light are enhanced in the plasmonic near-field resulting in an EF that is dependent on the enhanced near-field to the fourth power.[20] The EF is an important metric in TERS and defines the performance of the probe tip. The signal-to-noise ratio (SNR) is another important performance metric that represents the quality of the observable spectra. The SNR accounts for both the performance of the TERS tip as well as the optical system itself. TERS systems have many different configurations and can have top-, bottom-, or side-illumination.[38] Parabolic mirror illumination systems have also been explored.[39] Fiber coupled TERS probes have shown promise for increased optical coupling.[15] Each system has advantages and disadvantages. For example, bottom-illumination TERS systems can use objectives with a high numerical aperature but require transparent samples. Side-illumination TERS systems can work with arbitrary samples, but require longer focal distances and smaller optical efficiencies. In order to maximize TERS performance, a TERS probe with a high EF, and the correct optical system are required.

1.3. TERS Applications

1.3.1. Carbon Nanomaterials

Carbon nanomaterials such as carbon nanotubes (CNTs) and graphene display unique electrical, thermal, and mechanical properties. They have shown promise in field-effect transistors,[40, 41] optoelectronic devices,[42] composite materials,[43] transparent electrodes,[44] and water purification.[45] The properties of carbon nanomaterials are highly dependent on their atomic structure, which cannot be studied

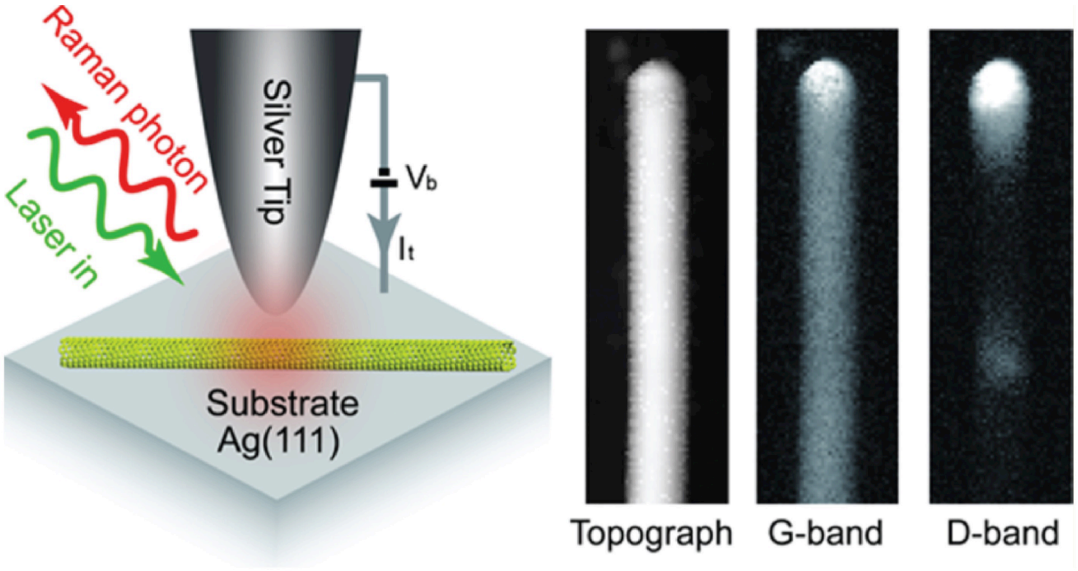

Figure 1.2. Schematic and example spectra of the topography and TERS maps of a carbon nanotube. An Ag STM probe is scanned over a single nanotube and provides simultaneous topographic and chemical information. The D-band provides specific insights about defects within the atomic structure. [Reprinted with permission from Reference 10]

by traditional optical spectroscopy methods, limited to the diffraction limit of light.

TERS has identified many properties of carbon nanotubes (CNTs) at the individual CNT level. A study in 2014 unambiguously showed the ability to not only identify but to spectroscopically map a single CNT with 1.7 nm spatial resolution.[11] In 2016 this resolution was increased to 0.7 nm.[10] This high resolution allowed TERS images of the defect induced D-band to identify individual defects within a CNT (Figure 1.2.). The relaxation length of electron-hole pairs around single defects was experimentally determined to be 2.2 nm.

By applying controlled amounts of pressure during TERS measurements, the electronic properties of individual CNTs can be probed. A study confirmed the difference between metallic and semiconducting CNTs by measuring the difference in peak shifts.[36] Metallic CNTs are achiral and thus vibrational modes are purely axial

and circumferential, while semiconducting CNTs have chiral properties. By examining the shape of the G-band, the chirality of the CNT can be determined. Mechanical deformation induces different changes to the vibrational structure to each type of CNT, which can easily be identified via TERS.

By correlating topography with TERS, properties and locations of individual CNTs within a bundle were identified.[46] The radial breathing mode (RBM) is a vibrational mode unique to a specific chirality and diameter of a CNT. TERS from the RBMs of different nanotubes along with topography was used to determine the chiral index, CNT diameter, and precise location within the bundle.

TERS has also been used to map graphene. By using a Ag coated AFM tip, graphene monolayers on glass were imaged with a resolution of 20 nm.[47] The presence and shape of the 2D vibrational mode identified the regions of monolayer and bilayer graphene. Additionally the relative strength of the D-band identifies high defect regions along the graphene edge as well as point and line defects. The 2D vibrational mode has also been used to identify regions of local strain in graphene. When monolayer graphene was placed over a 5 nm particle, changes in the TER spectra were used to quantify the local strain of the graphene.[48] Local contamination and hydrogen termination of graphene have also been reported *via* TERS.[49]

1.3.2. Single Molecule TERS

TERS can provide both the field-enhancement and field-localization to generate Raman spectra from single molecules. The ability to study single molecules via TERS has enabled basic studies into molecular kinetics,[50, 51] bonding properties,[52]

and orientations on surfaces.[8] Raman enhancements must be high to achieve SMTERS. Dye molecules are often used in SMTERS studies as they have molecular resonances that provide additional enhancement.[20] High field-enhancements and local temperature increases can induce molecular diffusion or photobleaching, preventing accurate measurements. SMTERS experiments account for this by using combinations of molecules fixed to a surface, low temperatures, and short collection times. SMTERS experiments are also often performed in ultra-high vacuum (UHV) conditions to control surface quality, prevent contamination, and reduce photodegredation.[53]

SMTERS was first achieved by using the resonant Raman dye molecule brilliant cresyl blue (BCB) excited at 633 nm in a gap-mode configuration.[54] The detection of a single BCB molecule was assumed by using low molecular surface coverage. The observation of spectral fluctuations, also known as blinking, supports this hypothesis. When only a single molecule accounts for the entire visible Raman spectra, blinking can result from molecules diffusing through, rotating within the hotspot, or small variations in excited-state lifetimes.[55-57] In 2012 more conclusive evidence was provided for SMTERS using the isotopologue method.[58] Two isotopes of Rhodamine 6G (R6G) were both placed in the presence of a TERS probe at low concentrations. When the Raman spectra for only a single isotope are observed, the likely origin is a single molecule. With time dependent TERS measurements, spectra of each isotope were observed individually as well as spectra showing both components. The study concludes that when both isotopes are observed there are

multiple molecules in the hotspot. Due to molecular diffusion there are also times when only a single molecule of either isotope is present.

In a 2013 groundbreaking study, TERS demonstrated the ability to map a single molecule.[8] A sub-monolayer of a porphyrin molecule, meso-tetrakis(3,5-di-tertiarybutylphenyl)-porphyrin (H_2TBPP), was carefully placed on an single-crystal Ag surface under low-temperature UHV conditions. A TERS probe with a plasmon resonance that overlapped with a molecular electronic resonance was chosen to maximize Raman enhancements. Chemical images of the porphyrin structure were obtained with 0.7 nm resolution (Figure 1.3.). The relative Raman intensities of different vibrational peaks were compared with calculated Raman spectra of the same molecule and used to determine the angular orientation of the molecule relative to the surface. A follow up study combined TERS with tip-enhanced fluorescence (TEF) to

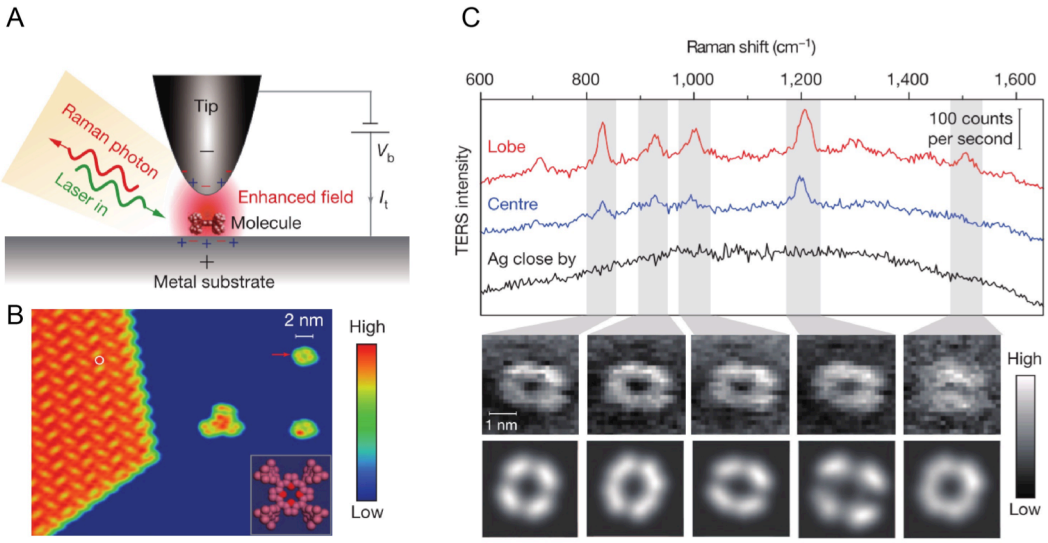

Figure 1.3. Schematic, STM topography, and TERS maps of single molecules. (A) Schematic of a Ag TERS tip positioned over a single molecule. (B) topography of a cluster of porphyrin molecules as well as several isolated molecules. (C) Example TERS spectra from different positions within a single molecule and TERS maps representing the spatial intensity of various vibrational modes showing a 0.7 nm TERS resolution. [Adapted with permission from Reference 8]

probe the molecule-surface interaction, and suggested that the H2TBPP was weakly coupled to the metallic substrate supporting it.[52] TERS has also been used to map and identify two distinct types of molecules positioned within van der Waals contact of each other, demonstrating 0.5 nm resolution.[9]

1.3.3. TERS in Catalysis

Understanding how catalysts operate is essential for many industrial processes. Spectroscopic methods such as infrared (IR), sum frequency generation (SFG), and surface-enhanced Raman spectroscopy (SERS) have all been used to study catalytic reactions.[59] These techniques offer valuable insight into the chemistry of the catalytic reactions. The main advantage of using SERS to study catalysis is the surface sensitivity. The Raman spectra originate from a sample near a plasmonic nanostructure, which can coincide with the catalytic surface, enabling reaction sensitivity down to a single nanostructure. Only TERS however has been able to provide the spatial resolution to identify catalytic hotspots within a nanostructure, or identify the reaction of a single molecule on a catalytic surface. For example, the photoisomerization of a single azobenzene molecule has been reported.[60]

In a demonstration of catalytic activity mapping *via* TERS, the photocatalytic reaction of p-nitrothiophenol (pNTP) to p,p'-dimercaptoazobisbenzene (DMAB) on a crystalline Au surface was reported.[61] To monitor the reaction *in situ*, a 633 nm excitation was used to continuously monitor the TERS spectra(does not result in photocatalysis). A seperate 532 nm excitation was pulsed to drive the photocatalytic reaction at specific time intervals. Due to the small hotspot generated by a TERS

probe, the observation in the few molecule regime of the photocatalytic reaction was achieved. In order to identify catalytic hotspots, a roughened Ag substrate was used as the photocatalyst.[62] The Ag TERS tip was protected with an alumina layer to prevent the tip from interfering with the reaction. TERS maps were generated by rastering the tip over the photocatalyst under 532 nm excitation. It was found that DMAB only formed in certain areas. When the catalytic hotspots were compared to topographic maps, it was hypothesized that photocatalytic activity is prominent in locations corresponding to plasmonic hotspots.

1.3.4. TERS in Biology

The high sensitivity of TERS makes it a promising tool for studying biological samples. The chemical information of Raman allows insights into samples unavailable with topography alone.[63] The low Raman cross-section of water allows TERS to be performed in liquids, a requirement for studying many biological molecules or cells.[64] The label free nature of TERS allows systems to be studied without further modification.

TERS has been employed in investigations of many types of biological surfaces. Understanding how amyloid fibrils fold has important consequences for understanding Alzheimer's and Parkinson's disease. TERS has been used to provide insight into the secondary structure of fibrils by chemically identifying hydrophobic and hydrophilic regions.[65, 66] The high spatial resolution of TERS has been able to identify streptavidin molecules embedded into a supported lipid bilayer, unachievable with topographic information alone.[67] Statistical methods have been employed to

identify proteins and lipid rich regions on the surface of human colon cancer cells.[68] In another study, the surface of a *Bacillus subtilis* spore was investigated and distinct regions were identified.[69] The spectral information in biological systems is rich and complex, research into understanding the full implications of TERS data is ongoing.[70]

In genomics, researchers are always searching for new ways to sequence and investigate DNA. TERS has been used on immobilized single stranded DNA to chemically identify individual nucleobases.[71] Vibrational modes unique to adenine, guanine, cytosine, and thymine have been identified. By acquiring TERS spectra along a DNA strand, the DNA can be sequenced one nucleobase at a time. Investigations of double stranded DNA have shown vibrational modes of the phosphate backbone only existent for hybridized DNA.[72] These studies suggest that investigation of hybridization reactions *in situ* is possible *via* TERS. TERS has also shown its ability to investigate double strand breaks, an important phenomenon which can lead to cell apoptosis.[73] Unlike electron microscopy and AFM characterization of double strand breaks, TERS can provide chemical information to understanding how and why DNA breaks.

1.4. TERS Probes

The design and fabrication of TERS probes with sufficient optical quality remains a major obstacle in the implementation of TERS. The sensitivity of TERS readouts is highly dependent on the near-field enhancement provided by the nanoscale metal feature at the tip apex.[74, 75] To achieve large near-field enhancements, TERS probes must possess a sharp radius of curvature, on the order of a few tens of

nanometers or less.[74] The metal tip must possess the appropriate size and shape such that it exhibits maximum field confinement of light near the incident wavelength.[76] In addition, tips must be resilient to both mechanical damage incurred by contact with the sample surface and thermal damage incurred by laser irradiation.[37, 77] While combining a TERS probe with a supporting metal surface can dramatically increase the Raman enhancement through the so-called gap-mode, the variability in performance of TERS remains heavily dependent on the probe geometry. There has been much recent work to develop TERS probes. The most common probes are etched Au and Ag wires and metal-clad AFM tips. These probes are simple to fabricate, however they suffer from reproducibility issues. The nanoscale morphology of the metal at the probe apex is hard to control and small changes can affect the plasmon resonance significantly. Engineered probes can have a tunable plasmon response and give better reproducibility.[15, 78, 79] These probes are often difficult to fabricate and require expensive cleanroom equipment. Other methods have been developed with a focus on batch fabrication.[80, 81] Despite extensive efforts, high variability between tips remains a problem.[14] The ultimate success of TERS as a routine analytical technique depends on a better understanding of the plasmon resonances in TERS probes and on developing inexpensive and dependable fabrication methods.

1.4.1. Etched Metal Wire TERS Probes

The most commonly used TERS probes are electrochemically etched Au or Ag wires.[82-84] A bulk wire is dipped into an etchant solution and surrounded by a ring

shaped counter electrode. An applied voltage dissolves the metal, leaving a sharpened metal point (Figure 1.4.). These tips can have a radius as sharp as 10 nm and lead to Raman enhancements high enough for SMTERS.[12] These tips are most often used for STM or shear-force AFM modes. Sharpened metal wire probes were used for all of the SMTERS studies discussed previously. The nature of the electrochemical etching process results in a large variation in geometry between probes, leading to low reproducibility.[13] The polycrystalline nature of bulk wires also contributes to morphological differences as well as additional scattering boundaries which can reduce the quality of the plasmon resonance.[85] By using carefully controlled AC voltages pulses, increased geometric regularity of the tips has been achieved in the fabrication of etched Au wire probes.[86, 87] Characterization of the regularity was performed only by SEM however, and no mention of reliable TERS performance was made. It is estimated that the most current etched wire TERS probes achieve good TERS contrast for 5-10% of the fabricated probes.[12]

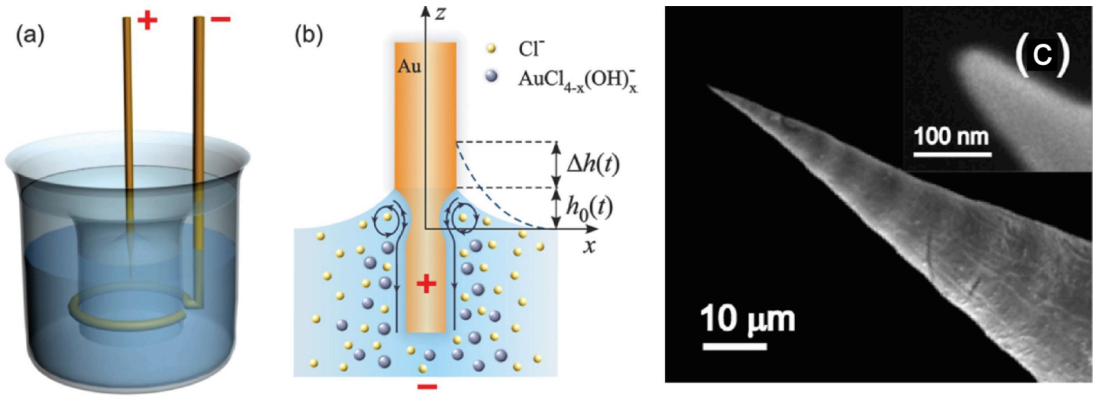

Figure 1.4. Schematic and SEM image of an etched Au wire TERS probe. (A-B) An Au wire is electrochemically etched using a ring counterelectrode in an acidic solution to a sharp point. (C) an SEM image shows the resulting TERS probe with a tip having a curvature of roughly 30 nm. [Adapted with permission from Reference 86]

1.4.2. TERS Probes *via* Physical Vapor Deposition

TERS probes operated in AFM contact or tapping modes are often fabricated by physical vapor deposition (PVD) methods such as evaporation or sputtering. These probes are fabricated by depositing a Ag or Au layer onto a commercially available AFM tip.[88, 89] The plasmon resonance of these TERS probes is determined by the structure of the metal film at the apex of the AFM tip which is determined by factors such as deposition rate, angle, and temperature.[90] As is the case with electrochemical etching, PVD methods lead to randomness in the geometry of the metal at the apex and irreproducibility in the TERS enhancement. A decisive advantage of these types of probe tips is that they can be fabricated on a wafer scale.[88] The metal deposition process can be followed by an immediate oxide coating which protects the probes against contamination and wear, at the expense of enhancement.[37] PVD AFM TERS probes have been used for many of the biological TERS studies discussed previously.

It was shown that Ag islands on a TERS probe, rather than a continuous metal film, improved reproducibility.[91] Closely spaced nanoparticle aggregates are able to broaden the plasmon resonance, allowing for larger amounts of geometric variation while maintaining consistent TERS performance. A direct experimental comparison of TERS probes fabricated with a smooth Ag film, connected Ag nanoparticles, and isolated Ag nanoparticles demonstrated an increased Raman enhancement for isolated Ag nanoparticle TERS probes. The increased performance was attributed to a larger absorption cross-section of separated nanoparticles, as well as waveguiding of the plasmon towards the apex, increasing the near-field enhancement.

A polarization scanning technique has been developed to help determine the near-field polarizations of PVD coated TERS probes.[92] This method allows insight to the performance of a given probe. By examining defocused scattering of a TERS probe in contact with a substrate, a near-field polarization image could be reconstructed. The knowledge of the near-field polarization allows tips to be specifically selected for TERS experiments where the near-field polarization is critical.[81]

1.4.3. Engineered TERS Probes

Many engineered TERS probes have been designed in order to improve the reliability of TERS enhancements. These probes are often fabricated using combinations of methods such as electron-beam lithography, focused-ion beam milling (FIB), and PVD. Engineered TERS probe fabrication is low-throughput as it can involve many steps. Despite the low-throughput fabrication, engineered probes offer unique advantages over the probes discussed in 1.4.2. and 1.4.3.

A grating coupled optical probe tip was developed to eliminate background Raman scattering during TERS measurements (Figure 1.5.A). Using FIB, a grating was cut into an electrochemically etched Au wire roughly 10 μm from the apex.[79, 93] The plasmon resonance with these TERS probes is determined by the angle of illumination and grating geometry, rather than the nanoscale morphology at the apex, increasing the reproducibility.[93, 94] TERS is performed by focusing the laser onto the grating, rather than at the apex. The grating acts as an optical coupler, creating a propagating plasmon. This plasmon travels to the probe tip and generates a highly

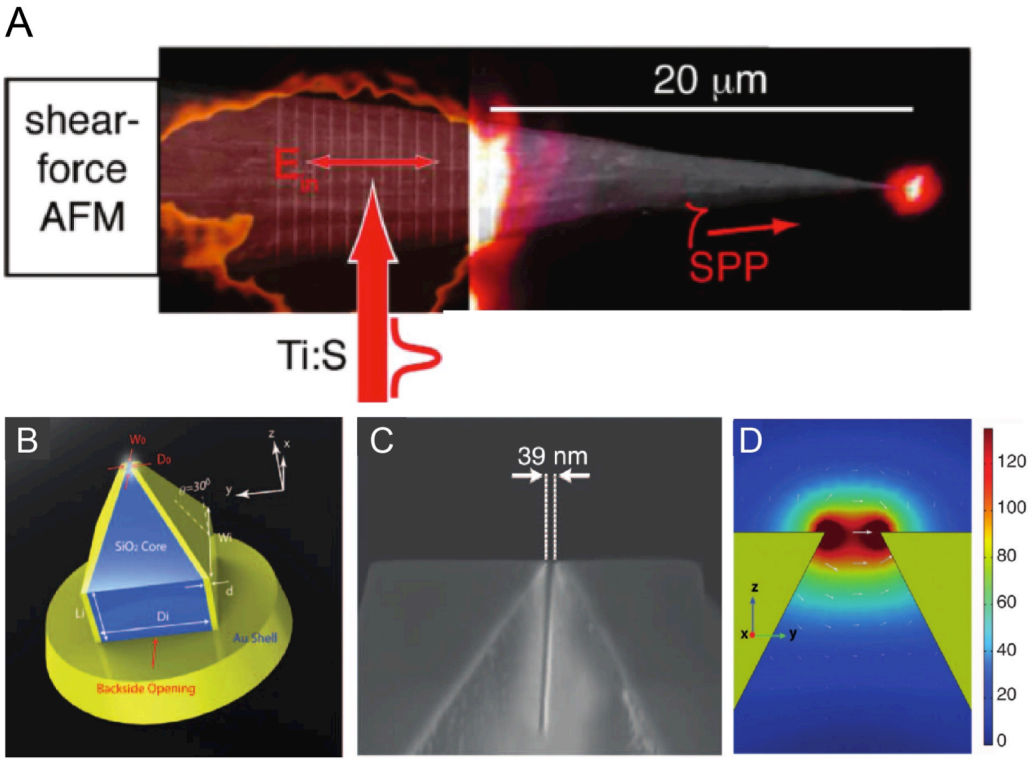

Figure 1.5. Grating coupled and Campanile optical probe tips. (A) An SEM showing an electrochemically etched Au wire with an optical grating etched into the base. Laser excitation is focused at the grating which creates an SPP travelling down the surface of the tip. At the apex a highly confined near-field is created. [Adapted with permission from Reference 79]. (B-D) A schematics (B) and SEM (C) of a campanile tip, showing (D) the near-field confinement at the nanogap created at the apex. [Adapted with permission from Reference 15]

confined near-field. With grating TERS probes, background Raman scattering is eliminated. Background Raman scattering normally originates from the laser spot focused on the analyte surrounding the TERS probe.

The campanile tip was developed to generate background free TERS with a broadband plasmon resonance (Figure 1.5.B-D).[15] The campanile tip is fabricated by cladding Au onto specific areas of a tapered optical fiber. A small nanogap is cut using FIB, resulting in a strong gap-plasmon within the tip itself. This geometry displays a plasmon resonance where light ranging from 600-1000 nm can be used for excitation, ensuring predictable performance of these probes. Because the gap-plasmon is

polarized in the plane of the substrate, 2D materials can be probed where in-plane near-field polarization is required.[95] A direct comparison of these probes to etched Au wires shows their outstanding optical performance.[78] Subsequent work has allowed external plasmonic structures to extend the working range of the campanile tip up to 100 nm.[96]

A template stripping method for TERS probe fabrication has also been explored.[80, 97] Microwells in Si are chemically etched into reproducible pyramidal templates. Au is evaporated into the microwells and stripped off with a droplet of epoxy that conforms to the Au. The side of the Au in contact with the Si is smooth and provides a highly reproducible TERS probe. This method allows simultaneous deposition of Au into millions of microwells. The disadvantage to this method is the microwell shapes are defined by the crystal structure of Si, which does not allow freedom to engineer the plasmonic nanostructure.

Other types of engineered TERS probes have been developed to achieve similar goals of background free, broadband, and high Raman enhancement. Photonic crystal structures have been etched into a Si probe which couple light into plasmonic waveguides.[16, 17, 98] AFM tips have been ground down to triangular geometries, which were then coated with evaporated Ag and Au films.[99] Bowtie nanoantenna have been grown on the flat face of a FIB milled AFM tip.[100] While each of these TERS probes offers unique advantages, they require extensive fabrication processes, and thus are not scalable.

1.4.4. Self-Assembly for TERS Probes

An increasing amount of attention is being given to TERS probes that are fabricated with self-assembly or bottom-up methods. These methods include chemically growing[101, 102] and self-assembling nanoparticles directly onto a scanning probe tip.[81, 103] In comparison to other TERS probe fabrication methods, bottom-up TERS probes allow the selection of plasmonic geometries and materials to be performed seperately from their positioning on a tip. All of these methods aim to position noble metal colloidal nanoparticles at the apex of a scanning probe tip. Colloidal nanoparticles are intriguing because they can be synthesized in a multitude of shapes, including spheres, cubes, polyhedra, discs, rods, tubes, and wires. Figure 1.6. shows SEM images of four shapes of chemically synthesized Ag colloidal nanoparticles. The unique and diverse set of shapes noble metal nanoparticles can form arises from their crystalline structure. Single-crystal noble-metal nanoparticles

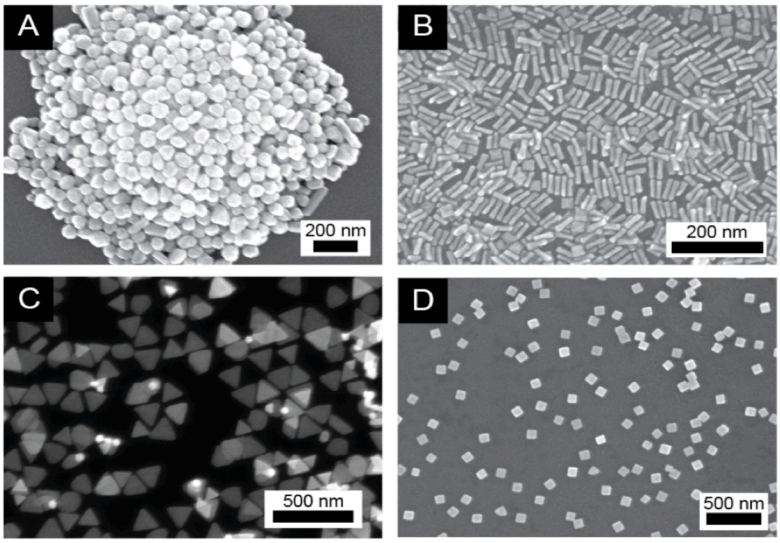

Figure 1.6. Examples of plasmonic colloidal nanoparticles. The scanning electron microscope (SEM) images show (A) Ag nanospheres, (B) Ag nanorods, (C) triangular Ag nanoprisms, (D) Ag nanocubes**.**

often appear as cubic, octahedral, tetrahedral, rod-like, or polyhedral discs, while multiply-twinned nanoparticles often display five-fold symmetry and appear commonly as decahedral, icosahedral, and wires with pentagonal cross-sections. The low energy families of crystal planes define the surfaces of noble metalnanoparticles.[104] Intersections of crystalline facets often lead to sharp corners and edges, often with curvatures of < 10 nm. In the case of some highly anisotropic nanoparticles, higher-order planes can be stabilized, resulting in extraordinarily sharp features. The penta-twinned Au nanobipyramid can have a point as sharp as 2 or 3 nm as a result of high-order planes, estimated as [105].[106, 107] Combinations of high crystallinity and sharp features lead to unique optical properties often unattainable by other TERS probe fabrication methods.

Colloidal nanoparticles can be grown or attached directly at the apex of an AFM tip. One method for attaching colloidal nanoparticles to a probe tip is functionalization of an AFM tip with a thiolated ligand, which strongly bind to Au and Ag nanoparticles. When the probe is brought into contact with a nanoparticle, the particle will bind to the tip apex.[108] Subsequent steps can then be taken to modify the particle size or grow a shell of a different material.[109] Nanoparticles can also be grown directly on the tip apex. When a bias is applied between a conductive AFM tip and a counter electrode, the electric field lines concentrate highly around the sharp apex (Figure 1.7.A-B). This allows isolated nanoparticles to be electrochemically grown at the tip apex through the electrochemical reduction of Au with an electrical pulse.[101] High electric field gradients at tips have also been leveraged to dielectrophoretically

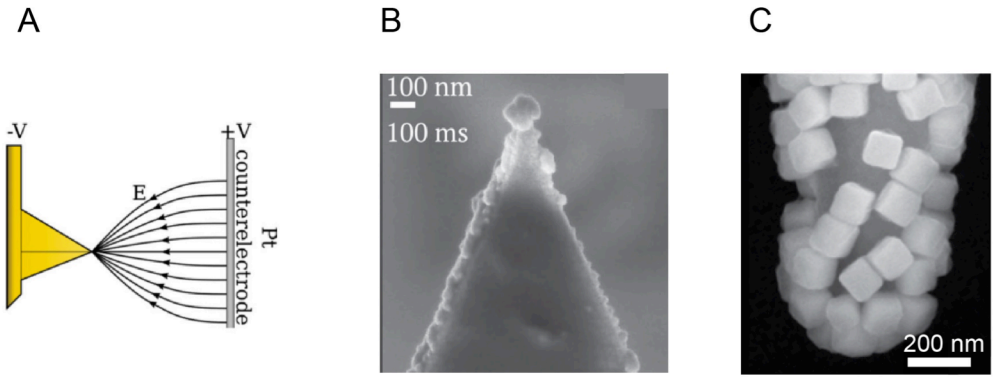

Figure 1.7. Self-assembled TERS probes (A-B) Leveraging field gradients at a sharp probe tip (A) can cause reduction of metal (B) to happen predominantly at the apex. [Adapted with permission from Reference 101]. (C) Close-packed colloidal Ag nanocubes deposited onto an AFM tip. [Adapted with permission from Reference 81]

attach colloidal nanoparticles.[103] High aspect ratio nanoparticles such as Ag nanowires will align along the electric field lines and are likely to attach with predictable orientations.

We developed a new type of TERS probe where a film of colloidal nanoparticles is used to coat an AFM tip. A close-packed film of Ag nanocubes is assembled at an air water interface and transferred to an AFM tip uniformly (Figure 1.7.C).[81] These TERS probes can be fabricated in large batches with > 80% reproducibility. They have also shown extraordinarily high Raman enhancements as a result of interparticle plasmon coupling. Self-assembled methods offer the advantage of selecting nanoparticle shapes and sizes independently of the fabrication process.

Nanoparticle based TERS probes offer many advantages over other fabrication methods such as electrochemical etching or top-down fabrication. The homogeneity of synthesized nanoparticles increases reproducibility of the plasmonic nanostructure placed at the probe apex, increasing the reliability of TERS performance. The shape control of these nanoparticles allows tunable plasmon resonances that are only

achievable with complex methods such as FIB. The high crystallinity and smooth faces of these particles results in higher Raman enhancements than can be achieved with bulk deposited or etched TERS probes. Isolated nanoparticles can also support higher field-enhancements than probes fabricated from larger continuous metal structures.

1.5. Organization of Chapters

The remainder of the dissertation is divided into chapters dedicated to scanning probe and substrate-supported plasmonic platforms fabricated from self-assembled colloidal nanoparticles. The application of these platforms is studied with respect to enhanced-Raman spectroscopy. Chapters 2 & 3 are focused on scanning-probe plasmonic tips and TERS, while chapters 4 – 6 are devoted to substrate-supported plasmonic systems and SERS.

Chapter 2 shows the development of a new type of TERS probe, which demonstrates high performance, reproducibility, and the ability to be fabricated in batches. We have named this probe the colloidal nanoantenna. Colloidal nanoantennas are fabricated by assembling close-packed Ag nanocube (AgNC) films onto AFM tips.

Chapter 3 shows that unlike other TERS probes, the performance of colloidal nanoantennas is largely invariant to many geometric variations in the plasmonic nanostructure. The robust optical response arises from complex hybrid plasmon modes that reflect the nature of close-packed AgNCs placed near metal surfaces. The discussion of these plasmon modes is relevant to the following chapters, which focus on the gap-plasmons of AgNCs oriented parallel to a metal surface.

Chapter 4 introduces a metasurface as a new platform for SERS (mSERS). mSERS substrates are highly versatile for studying both fundamental aspects of plasmon modes as well as many types of analytes. A unique aspect of mSERS substrates is their invariability over large areas, allowing large scale chemical mapping of surfaces.

Chapter 5 is an in depth study of the polydispersity of synthesized AgNCs and how it affects the Raman EF of real mSERS substrates. By examining features such as particle size and corner sharpness, we gain a better understanding of which factors are important for a strong optical response.

Chapter 6 observes quantum effects of mSERS substrates at unprecedented gap distances larger than 2 nanometers. We also show that this tunneling gap can be varied widely by modifying the chemistry within the plasmonic cavity. These quantum effects at large gap-distances have important consequences for both near- and far-field spectroscopy measurements, relating to both the colloidal nanoantenna and mSERS platforms.

1.6. References

1. Maier, S., *Plasmonics: Fundamentals and Applications*. 1 ed.; Springer US: 2007; p 224.

2. Tao, A. R.; Habas, S.; Yang, P., Shape Control of Colloidal Metal Nanocrystals. *Small* **2008,** *4* (3), 310-325.

3. Noda, S.; Chutinan, A.; Imada, M., Trapping and emission of photons by a single defect in a photonic bandgap structure. *Nature* **2000,** *407* (6804), 608-610.

4. Ogawa, S.; Imada, M.; Yoshimoto, S.; Okano, M.; Noda, S., Control of Light Emission by 3D Photonic Crystals. *Science* **2004,** *305* (5681), 227.

5. Yoon, I.; Baker, S. E.; Kim, K.; Fischer, N. O.; Heineck, D.; Wang, Y.; Esener, S. C.; Sirbuly, D. J., Nanofiber Near-Field Light–Matter Interactions for Enhanced Detection of Molecular Level Displacements and Dynamics. *Nano Letters* **2013,** *13* (4), 1440-1445.

6. Walia, S.; Shah, C. M.; Gutruf, P.; Nili, H.; Chowdhury, D. R.; Withayachumnankul, W.; Bhaskaran, M.; Sriram, S., Flexible metasurfaces and metamaterials: A review of materials and fabrication processes at micro- and nano-scales. *Applied Physics Reviews* **2015,** *2* (1), 011303.

7. Liu, Y.; Zhang, X., Metamaterials: a new frontier of science and technology. *Chemical Society Reviews* **2011,** *40* (5), 2494-2507.

8. Zhang, R.; Zhang, Y.; Dong, Z. C.; Jiang, S.; Zhang, C.; Chen, L. G.; Zhang, L.; Liao, Y.; Aizpurua, J.; Luo, Y.; Yang, J. L.; Hou, J. G., Chemical mapping of a single molecule by plasmon-enhanced Raman scattering. *Nature* **2013,** *498* (7452), 82-86.

9. Jiang, S.; Zhang, Y.; Zhang, R.; Hu, C.; Liao, M.; Luo, Y.; Yang, J.; Dong, Z.; Hou, J. G., Distinguishing adjacent molecules on a surface using plasmon-enhanced Raman scattering. *Nat Nano* **2015,** *10* (10), 865-869.

10. Liao, M.; Jiang, S.; Hu, C.; Zhang, R.; Kuang, Y.; Zhu, J.; Zhang, Y.; Dong, Z., Tip-Enhanced Raman Spectroscopic Imaging of Individual Carbon Nanotubes with Subnanometer Resolution. *Nano Letters* **2016,** *16* (7), 4040-4046.

11. Chen, C.; Hayazawa, N.; Kawata, S., A 1.7 nm resolution chemical analysis of carbon nanotubes by tip-enhanced Raman imaging in the ambient. *Nat Commun* **2014,** *5*.

12. Yasuhiko Fujita and Peter Walke and Steven De Feyter and Hiroshi, U.-i., Tip-enhanced Raman scattering microscopy: Recent advance in tip production. *Japanese Journal of Applied Physics* **2016,** *55* (8S1), 08NA02.

13. Neacsu, C. C.; Steudle, G. A.; Raschke, M. B., Plasmonic light scattering from nanoscopic metal tips. *Applied Physics B* **2005,** *80* (3), 295-300.

14. Blum, C.; Opilik, L.; Atkin, J. M.; Braun, K.; Kämmer, S. B.; Kravtsov, V.; Kumar, N.; Lemeshko, S.; Li, J.-F.; Luszcz, K.; Maleki, T.; Meixner, A. J.; Minne, S.; Raschke, M. B.; Ren, B.; Rogalski, J.; Roy, D.; Stephanidis, B.; Wang, X.; Zhang, D.; Zhong, J.-H.; Zenobi, R., Tip-enhanced Raman spectroscopy – an interlaboratory reproducibility and comparison study. *Journal of Raman Spectroscopy* **2014,** *45* (1), 22-31.

15. Bao, W.; Melli, M.; Caselli, N.; Riboli, F.; Wiersma, D. S.; Staffaroni, M.; Choo, H.; Ogletree, D. F.; Aloni, S.; Bokor, J.; Cabrini, S.; Intonti, F.; Salmeron, M. B.; Yablonovitch, E.; Schuck, P. J.; Weber-Bargioni, A., Mapping Local Charge Recombination Heterogeneity by Multidimensional Nanospectroscopic Imaging. *Science* **2012,** *338* (6112), 1317-1321.

16. De Angelis, F.; Das, G.; Candeloro, P.; Patrini, M.; Galli, M.; Bek, A.; Lazzarino, M.; Maksymov, I.; Liberale, C.; Andreani, L. C.; Di Fabrizio, E., Nanoscale chemical mapping using three-dimensional adiabatic compression of surface plasmon polaritons. *Nat Nano* **2010,** *5* (1), 67-72.

17. Taminiau, T. H.; Moerland, R. J.; Segerink, F. B.; Kuipers, L.; van Hulst, N. F., λ/4 Resonance of an Optical Monopole Antenna Probed by Single Molecule Fluorescence. *Nano Letters* **2007,** *7* (1), 28-33.

18. Harris, D. C.; Betolucci, M. D., *SYMMETRY AND SPECTROSCOPY An Introduction to Vibrational and Electronic Spectroscopy*. 2nd ed.; Dover Publications, Inc.: 1989.

19. *Raman Spectroscopy for Nanomaterials Characterization*. 1 ed.; Springer-Verlag Berlin Heidelberg: 2012; p 646.

20. Ru, E. L.; Etchegoin, P., *Principles of Surface-Enhanced Raman Spectroscopy: and related plasmonic effects*. Elsevier Science: 2008.

21. Kiefer, W., Recent Advances in linear and nonlinear Raman spectroscopy I. *Journal of Raman Spectroscopy* **2007,** *38* (12), 1538-1553.

22. Mayer, K. M.; Hafner, J. H., Localized Surface Plasmon Resonance Sensors. *Chemical Reviews* **2011,** *111* (6), 3828-3857.

23. Hill, R. T.; Mock, J. J.; Hucknall, A.; Wolter, S. D.; Jokerst, N. M.; Smith, D. R.; Chilkoti, A., Plasmon Ruler with Angstrom Length Resolution. *ACS Nano* **2012,** *6* (10), 9237-9246.

24. Zhang, Z.; Yang, P.; Xu, H.; Zheng, H., Surface enhanced fluorescence and Raman scattering by gold nanoparticle dimers and trimers. *Journal of Applied Physics* **2013,** *113* (3), 033102.

25. Baffou, G.; Quidant, R., Thermo-plasmonics: using metallic nanostructures as nano-sources of heat. *Laser & Photonics Reviews* **2013,** *7* (2), 171-187.

26. Tao, F.; Spivey, J., *Metal Nanoparticles for Catalysis: Advances and Applications*. The Royal Society of Chemistry: 2014; p 270.

27. Bailo, E.; Deckert, V., Tip-enhanced Raman scattering. *Chemical Society Reviews* **2008,** *37* (5), 921-930.

28. Pettinger, B.; Ren, B.; Picardi, G.; Schuster, R.; Ertl, G., Nanoscale Probing of Adsorbed Species by Tip-Enhanced Raman Spectroscopy. *Physical Review Letters* **2004,** *92* (9), 096101.

29. Steidtner, J.; Pettinger, B., Tip-Enhanced Raman Spectroscopy and Microscopy on Single Dye Molecules with 15~nm Resolution. *Physical Review Letters* **2008,** *100* (23), 236101.

30. Stadler, J.; Schmid, T.; Zenobi, R., Nanoscale Chemical Imaging Using Top-Illumination Tip-Enhanced Raman Spectroscopy. *Nano Letters* **2010,** *10* (11), 4514-4520.

31. Hell, S. W.; Wichmann, J., Breaking the diffraction resolution limit by stimulated emission: stimulated-emission-depletion fluorescence microscopy. *Optics Letters* **1994,** *19* (11), 780-782.

32. Bosman, M.; Keast, V. J.; García-Muñoz, J. L.; D'Alfonso, A. J.; Findlay, S. D.; Allen, L. J., Two-Dimensional Mapping of Chemical Information at Atomic Resolution. *Physical Review Letters* **2007,** *99* (8), 086102.

33. Kothleitner, G.; Neish, M. J.; Lugg, N. R.; Findlay, S. D.; Grogger, W.; Hofer, F.; Allen, L. J., Quantitative Elemental Mapping at Atomic Resolution Using X-Ray Spectroscopy. *Physical Review Letters* **2014,** *112* (8), 085501.

34. Hayazawa, N.; Yano, T.; Watanabe, H.; Inouye, Y.; Kawata, S., Detection of an individual single-wall carbon nanotube by tip-enhanced near-field Raman spectroscopy. *Chemical Physics Letters* **2003,** *376* (1–2), 174-180.

35. Rasmussen, A.; Deckert, V., Surface- and tip-enhanced Raman scattering of DNA components. *Journal of Raman Spectroscopy* **2006,** *37* (1-3), 311-317.

36. Yano, T.-a.; Verma, P.; Saito, Y.; Ichimura, T.; Kawata, S., Pressure-assisted tip-enhanced Raman imaging at a resolution of a few nanometres. *Nat Photon* **2009,** *3* (8), 473-477.

37. Agapov, R. L.; Sokolov, A. P.; Foster, M. D., Protecting TERS probes from degradation: extending mechanical and chemical stability. *Journal of Raman Spectroscopy* **2013,** *44* (5), 710-716.

38. Schmid, T.; Opilik, L.; Blum, C.; Zenobi, R., Nanoscale Chemical Imaging Using Tip-Enhanced Raman Spectroscopy: A Critical Review. *Angewandte Chemie International Edition* **2013,** *52* (23), 5940-5954.

39. Zhang, D.; Wang, X.; Braun, K.; Egelhaaf, H.-J.; Fleischer, M.; Hennemann, L.; Hintz, H.; Stanciu, C.; Brabec, C. J.; Kern, D. P.; Meixner, A. J., Parabolic mirror-assisted tip-enhanced spectroscopic imaging for non-transparent materials. *Journal of Raman Spectroscopy* **2009,** *40* (10), 1371-1376.

40. Brady, G. J.; Way, A. J.; Safron, N. S.; Evensen, H. T.; Gopalan, P.; Arnold, M. S., Quasi-ballistic carbon nanotube array transistors with current density exceeding Si and GaAs. *Science Advances* **2016,** *2* (9).

41. Schwierz, F., Graphene transistors. *Nat Nano* **2010,** *5* (7), 487-496.

42. Fang, Z.; Wang, Y.; Liu, Z.; Schlather, A.; Ajayan, P. M.; Koppens, F. H. L.; Nordlander, P.; Halas, N. J., Plasmon-Induced Doping of Graphene. *ACS Nano* **2012,** *6* (11), 10222-10228.

43. Stankovich, S.; Dikin, D. A.; Dommett, G. H. B.; Kohlhaas, K. M.; Zimney, E. J.; Stach, E. A.; Piner, R. D.; Nguyen, S. T.; Ruoff, R. S., Graphene-based composite materials. *Nature* **2006,** *442* (7100), 282-286.

44. Rana, K.; Singh, J.; Ahn, J.-H., A graphene-based transparent electrode for use in flexible optoelectronic devices. *Journal of Materials Chemistry C* **2014,** *2* (15), 2646-2656.

45. Das, R.; Ali, M. E.; Hamid, S. B. A.; Ramakrishna, S.; Chowdhury, Z. Z., Carbon nanotube membranes for water purification: A bright future in water desalination. *Desalination* **2014,** *336*, 97-109.

46. Peica, N.; Thomsen, C.; Maultzsch, J., Studying the local character of Raman features of single-walled carbon nanotubes along a bundle using TERS. *Nanoscale Research Letters* **2011,** *6* (1), 174.

47. Su, W.; Kumar, N.; Dai, N.; Roy, D., Nanoscale mapping of intrinsic defects in single-layer graphene using tip-enhanced Raman spectroscopy. *Chemical Communications* **2016,** *52* (53), 8227-8230.

48. Ryan Beams and Luiz Gustavo Cançado and Ado Jorio and, A. N. V. a. L. N., Tip-enhanced Raman mapping of local strain in graphene. *Nanotechnology* **2015,** *26* (17), 175702.

49. Stadler, J.; Schmid, T.; Zenobi, R., Nanoscale Chemical Imaging of Single-Layer Graphene. *ACS Nano* **2011,** *5* (10), 8442-8448.

50. Klingsporn, J. M.; Jiang, N.; Pozzi, E. A.; Sonntag, M. D.; Chulhai, D.; Seideman, T.; Jensen, L.; Hersam, M. C.; Duyne, R. P. V., Intramolecular Insight into Adsorbate–Substrate Interactions via Low-Temperature, Ultrahigh-Vacuum Tip-Enhanced Raman Spectroscopy. *Journal of the American Chemical Society* **2014,** *136* (10), 3881-3887.

51. Jiang, N.; Chiang, N.; Madison, L. R.; Pozzi, E. A.; Wasielewski, M. R.; Seideman, T.; Ratner, M. A.; Hersam, M. C.; Schatz, G. C.; Van Duyne, R. P., Nanoscale Chemical Imaging of a Dynamic Molecular Phase Boundary with Ultrahigh Vacuum Tip-Enhanced Raman Spectroscopy. *Nano Letters* **2016,** *16* (6), 3898-3904.

52. Chiang, N.; Jiang, N.; Chulhai, D. V.; Pozzi, E. A.; Hersam, M. C.; Jensen, L.; Seideman, T.; Van Duyne, R. P., Molecular-Resolution Interrogation of a Porphyrin Monolayer by Ultrahigh Vacuum Tip-Enhanced Raman and Fluorescence Spectroscopy. *Nano Letters* **2015,** *15* (6), 4114-4120.

53. Pettinger, B.; Schambach, P.; Villagómez, C. J.; Scott, N., Tip-Enhanced Raman Spectroscopy: Near-Fields Acting on a Few Molecules. *Annual Review of Physical Chemistry* **2012,** *63* (1), 379-399.

54. Zhang, W.; Yeo, B. S.; Schmid, T.; Zenobi, R., Single Molecule Tip-Enhanced Raman Spectroscopy with Silver Tips. *The Journal of Physical Chemistry C* **2007,** *111* (4), 1733-1738.

55. Wang, Z.; Rothberg, L. J., Origins of Blinking in Single-Molecule Raman Spectroscopy. *The Journal of Physical Chemistry B* **2005,** *109* (8), 3387-3391.

56. Futamata, M.; Maruyama, Y.; Ishikawa, M., Critical importance of the junction in touching Ag particles for single molecule sensitivity in SERS. *Journal of Molecular Structure* **2005,** *735–736*, 75-84.

57. Sonntag, M. D.; Chulhai, D.; Seideman, T.; Jensen, L.; Van Duyne, R. P., The Origin of Relative Intensity Fluctuations in Single-Molecule Tip-Enhanced Raman Spectroscopy. *Journal of the American Chemical Society* **2013,** *135* (45), 17187-17192.

58. Sonntag, M. D.; Klingsporn, J. M.; Garibay, L. K.; Roberts, J. M.; Dieringer, J. A.; Seideman, T.; Scheidt, K. A.; Jensen, L.; Schatz, G. C.; Van Duyne, R. P., Single-Molecule Tip-Enhanced Raman Spectroscopy. *The Journal of Physical Chemistry C* **2012,** *116* (1), 478-483.

59. Hartman, T.; Wondergem, C. S.; Kumar, N.; van den Berg, A.; Weckhuysen, B. M., Surface- and Tip-Enhanced Raman Spectroscopy in Catalysis. *The Journal of Physical Chemistry Letters* **2016,** *7* (8), 1570-1584.

60. Tallarida, N.; Rios, L.; Apkarian, V. A.; Lee, J., Isomerization of One Molecule Observed through Tip-Enhanced Raman Spectroscopy. *Nano Letters* **2015,** *15* (10), 6386-6394.

61. van Schrojenstein Lantman, E. M.; Deckert-Gaudig, T.; Mank, A. J. G.; Deckert, V.; Weckhuysen, B. M., Catalytic processes monitored at the nanoscale with tip-enhanced Raman spectroscopy. *Nat Nano* **2012,** *7* (9), 583-586.

62. Kumar, N.; Stephanidis, B.; Zenobi, R.; Wain, A. J.; Roy, D., Nanoscale mapping of catalytic activity using tip-enhanced Raman spectroscopy. *Nanoscale* **2015,** *7* (16), 7133-7137.

63. Pozzi, E. A.; Sonntag, M. D.; Jiang, N.; Klingsporn, J. M.; Hersam, M. C.; Van Duyne, R. P., Tip-Enhanced Raman Imaging: An Emergent Tool for Probing Biology at the Nanoscale. *ACS Nano* **2013,** *7* (2), 885-888.

64. Schmid, T.; Yeo, B.-S.; Leong, G.; Stadler, J.; Zenobi, R., Performing tip-enhanced Raman spectroscopy in liquids. *Journal of Raman Spectroscopy* **2009,** *40* (10), 1392-1399.

65. Paulite, M.; Blum, C.; Schmid, T.; Opilik, L.; Eyer, K.; Walker, G. C.; Zenobi, R., Full Spectroscopic Tip-Enhanced Raman Imaging of Single Nanotapes Formed from β-Amyloid(1–40) Peptide Fragments. *ACS Nano* **2013,** *7* (2), 911-920.

66. Deckert-Gaudig, T.; Kurouski, D.; Hedegaard, M. A. B.; Singh, P.; Lednev, I. K.; Deckert, V., Spatially resolved spectroscopic differentiation of hydrophilic and hydrophobic domains on individual insulin amyloid fibrils. *Scientific Reports* **2016,** *6*, 33575.

67. Böhme, R.; Cialla, D.; Richter, M.; Rösch, P.; Popp, J.; Deckert, V., Biochemical imaging below the diffraction limit – probing cellular membrane related structures by tip-enhanced Raman spectroscopy (TERS). *Journal of Biophotonics* **2010,** *3* (7), 455-461.

68. Richter, M.; Hedegaard, M.; Deckert-Gaudig, T.; Lampen, P.; Deckert, V., Laterally Resolved and Direct Spectroscopic Evidence of Nanometer-Sized Lipid and Protein Domains on a Single Cell. *Small* **2011,** *7* (2), 209-214.

69. Rusciano, G.; Zito, G.; Isticato, R.; Sirec, T.; Ricca, E.; Bailo, E.; Sasso, A., Nanoscale Chemical Imaging of Bacillus subtilis Spores by Combining Tip-Enhanced Raman Scattering and Advanced Statistical Tools. *ACS Nano* **2014,** *8* (12), 12300-12309.

70. Treffer, R.; Böhme, R.; Deckert-Gaudig, T.; Lau, K.; Tiede, S.; Lin, X.; Deckert, V., Advances in TERS (tip-enhanced Raman scattering) for biochemical applications. *Biochemical Society Transactions* **2012,** *40* (4), 609.

71. Treffer, R.; Lin, X.; Bailo, E.; Deckert-Gaudig, T.; Deckert, V., Distinction of nucleobases – a tip-enhanced Raman approach. *Beilstein Journal of Nanotechnology* **2011,** *2*, 628-637.

72. Najjar, S.; Talaga, D.; Schué, L.; Coffinier, Y.; Szunerits, S.; Boukherroub, R.; Servant, L.; Rodriguez, V.; Bonhommeau, S., Tip-Enhanced Raman Spectroscopy of Combed Double-Stranded DNA Bundles. *The Journal of Physical Chemistry C* **2014,** *118* (2), 1174-1181.

73. Lipiec, E.; Sekine, R.; Bielecki, J.; Kwiatek, W. M.; Wood, B. R., Molecular Characterization of DNA Double Strand Breaks with Tip-Enhanced Raman Scattering. *Angewandte Chemie International Edition* **2014,** *53* (1), 169-172.

74. Demming, A. L.; Festy, F.; Richards, D., Plasmon resonances on metal tips: Understanding tip-enhanced Raman scattering. *The Journal of Chemical Physics* **2005,** *122* (18), 184716.

75. Richards, D.; Milner, R. G.; Huang, F.; Festy, F., Tip-enhanced Raman microscopy: practicalities and limitations. *Journal of Raman Spectroscopy* **2003,** *34* (9), 663-667.

76. Zhang, W.; Cui, X.; Martin, O. J. F., Local field enhancement of an infinite conical metal tip illuminated by a focused beam. *Journal of Raman Spectroscopy* **2009,** *40* (10), 1338-1342.

77. Zhang, W.; Schmid, T.; Yeo, B.-S.; Zenobi, R., Near-Field Heating, Annealing, and Signal Loss in Tip-Enhanced Raman Spectroscopy. *The Journal of Physical Chemistry C* **2008,** *112* (6), 2104-2108.

78. Bao, W.; Staffaroni, M.; Bokor, J.; Salmeron, M. B.; Yablonovitch, E.; Cabrini, S.; Weber-Bargioni, A.; Schuck, P. J., Plasmonic near-field probes: a comparison of the campanile geometry with other sharp tips. *Optics Express* **2013,** *21* (7), 8166-8176.

79. Neacsu, C. C.; Berweger, S.; Olmon, R. L.; Saraf, L. V.; Ropers, C.; Raschke, M. B., Near-Field Localization in Plasmonic Superfocusing: A Nanoemitter on a Tip. *Nano Letters* **2010,** *10* (2), 592-596.

80. Johnson, T. W.; Lapin, Z. J.; Beams, R.; Lindquist, N. C.; Rodrigo, S. G.; Novotny, L.; Oh, S.-H., Highly Reproducible Near-Field Optical Imaging with Sub-20-nm Resolution Based on Template-Stripped Gold Pyramids. *ACS Nano* **2012,** *6* (10), 9168-9174.

81. Dill, T. J.; Rozin, M. J.; Palani, S.; Tao, A. R., Colloidal Nanoantennas for Hyperspectral Chemical Mapping. *ACS Nano* **2016,** *10* (8), 7523-7531.

82. Stadler, J.; Schmid, T.; Opilik, L.; Kuhn, P.; Dittrich, P. S.; Zenobi, R., Tip-enhanced Raman spectroscopic imaging of patterned thiol monolayers. *Beilstein Journal of Nanotechnology* **2011,** *2*, 509-515.

83. Stöckle, R. M.; Suh, Y. D.; Deckert, V.; Zenobi, R., Nanoscale chemical analysis by tip-enhanced Raman spectroscopy. *Chemical Physics Letters* **2000,** *318* (1–3), 131-136.

84. Ren, B.; Picardi, G.; Pettinger, B., Preparation of gold tips suitable for tip-enhanced Raman spectroscopy and light emission by electrochemical etching. *Review of Scientific Instruments* **2004,** *75* (4), 837-841.

85. Huang, W.; Qian, W.; El-Sayed, M. A.; Ding, Y.; Wang, Z. L., Effect of the Lattice Crystallinity on the Electron−Phonon Relaxation Rates in Gold Nanoparticles. *The Journal of Physical Chemistry C* **2007,** *111* (29), 10751-10757.

86. Kharintsev, S. S.; Hoffmann, G. G.; Fishman, A. I.; Salakhov, M. K., Plasmonic optical antenna design for performing tip-enhanced Raman spectroscopy and microscopy. *Journal of Physics D: Applied Physics* **2013,** *46* (14), 145501.

87. Kharintsev, S. S.; Noskov, A. I.; Hoffmann, G. G.; Loos, J., Near-field optical taper antennas fabricated with a highly replicable ac electrochemical etching method. *Nanotechnology* **2011,** *22* (2), 025202.

88. Hayazawa, N.; Yano, T.-a.; Kawata, S., Highly reproducible tip-enhanced Raman scattering using an oxidized and metallized silicon cantilever tip as a tool for everyone. *Journal of Raman Spectroscopy* **2012,** *43* (9), 1177-1182.

89. Taguchi, A.; Hayazawa, N.; Saito, Y.; Ishitobi, H.; Tarun, A.; Kawata, S., Controlling the plasmon resonance wavelength in metal-coated probe using refractive index modification. *Optics Express* **2009,** *17* (8), 6509-6518.

90. Huang, T.-X.; Huang, S.-C.; Li, M.-H.; Zeng, Z.-C.; Wang, X.; Ren, B., Tip-enhanced Raman spectroscopy: tip-related issues. *Analytical and Bioanalytical Chemistry* **2015,** *407* (27), 8177-8195.

91. Taguchi, A.; Yu, J.; Verma, P.; Kawata, S., Optical antennas with multiple plasmonic nanoparticles for tip-enhanced Raman microscopy. *Nanoscale* **2015,** *7* (41), 17424-17433.

92. Mino, T.; Saito, Y.; Verma, P., Quantitative Analysis of Polarization-Controlled Tip-Enhanced Raman Imaging through the Evaluation of the Tip Dipole. *ACS Nano* **2014,** *8* (10), 10187-10195.

93. Ropers, C.; Neacsu, C. C.; Elsaesser, T.; Albrecht, M.; Raschke, M. B.; Lienau, C., Grating-Coupling of Surface Plasmons onto Metallic Tips: A Nanoconfined Light Source. *Nano Letters* **2007,** *7* (9), 2784-2788.

94. Berweger, S.; Atkin, J. M.; Olmon, R. L.; Raschke, M. B., Adiabatic Tip-Plasmon Focusing for Nano-Raman Spectroscopy. *The Journal of Physical Chemistry Letters* **2010,** *1* (24), 3427-3432.

95. Bao, W.; Borys, N. J.; Ko, C.; Suh, J.; Fan, W.; Thron, A.; Zhang, Y.; Buyanin, A.; Zhang, J.; Cabrini, S.; Ashby, P. D.; Weber-Bargioni, A.; Tongay, S.; Aloni, S.; Ogletree, D. F.; Wu, J.; Salmeron, M. B.; Schuck, P. J., Visualizing nanoscale excitonic relaxation properties of disordered edges and grain boundaries in monolayer molybdenum disulfide. *Nat Commun* **2015,** *6*.

96. Polyakov, A.; Melli, M.; Cantarella, G.; Schwartzberg, A.; Weber-Bargioni, A.; James Schuck, P.; Cabrini, S., Coupling model for an extended-range plasmonic optical transformer scanning probe. *Light Sci Appl* **2014,** *3*, e195.

97. Jose, J.; Kress, S.; Barik, A.; Otto, L. M.; Shaver, J.; Johnson, T. W.; Lapin, Z. J.; Bharadwaj, P.; Novotny, L.; Oh, S.-H., Individual Template-Stripped Conductive Gold Pyramids for Tip-Enhanced Dielectrophoresis. *ACS Photonics* **2014,** *1* (5), 464-470.

98. Chen, D.; Miao, J.; Tian, Y.; Zhang, J.; Liu, Q., Field Enhancement of Tip with Spiral Nanostructure. *Plasmonics* **2014,** *9* (6), 1245-1249.

99. Kim, T.; Jeon, K.-S.; Heo, K.; Kim, H. M.; Park, J.; Suh, Y. D.; Hong, S., Multilayered nano-prism vertex tips for tip-enhanced Raman spectroscopy and imaging. *Analyst* **2013,** *138* (19), 5588-5593.

100. Weber-Bargioni, A.; Schwartzberg, A.; Schmidt, M.; Harteneck, B.; Ogletree, D. F.; Schuck, P. J.; Cabrini, S., Functional plasmonic antenna scanning probes fabricated by induced-deposition mask lithography. *Nanotechnology* **2010,** *21* (6), 065306.

101. Sanders, A.; Zhang, L.; Bowman, R. W.; Herrmann, L. O.; Baumberg, J. J., Facile Fabrication of Spherical Nanoparticle-Tipped AFM Probes for Plasmonic Applications. *Particle & Particle Systems Characterization* **2015,** *32* (2), 182-187.

102. Kim, W.; Kim, N.; Park, J. W.; Kim, Z. H., Nanostar probes for tip-enhanced spectroscopy. *Nanoscale* **2016,** *8* (2), 987-994.

103. You, Y.; Purnawirman, N. A.; Hu, H.; Kasim, J.; Yang, H.; Du, C.; Yu, T.; Shen, Z., Tip-enhanced Raman spectroscopy using single-crystalline Ag nanowire as tip. *Journal of Raman Spectroscopy* **2010,** *41* (10), 1156-1162.

104. Sun, Y.; Xia, Y., Shape-Controlled Synthesis of Gold and Silver Nanoparticles. *Science* **2002,** *298* (5601), 2176-2179.

105. Fraire, J. C.; Pérez, L. A.; Coronado, E. A., Cluster Size Effects in the Surface-Enhanced Raman Scattering Response of Ag and Au Nanoparticle Aggregates: Experimental and Theoretical Insight. *The Journal of Physical Chemistry C* **2013,** *117* (44), 23090-23107.

106. Liu; Guyot-Sionnest, P., Mechanism of Silver(I)-Assisted Growth of Gold Nanorods and Bipyramids. *The Journal of Physical Chemistry B* **2005,** *109* (47), 22192-22200.

107. Liu, M.; Guyot-Sionnest, P.; Lee, T.-W.; Gray, S. K., Optical properties of rodlike and bipyramidal gold nanoparticles from three-dimensional computations. *Physical Review B* **2007,** *76* (23), 235428.

108. Invited Review Article: A review of techniques for attaching micro- and nanoparticles to a probe's tip for surface force and near-field optical measurements. *Review of Scientific Instruments* **2007,** *78* (8), 081101.

109. Kim, W.; Kim, N.; Lee, E.; Kim, D.; Hwan Kim, Z.; Won Park, J., A tunable Au core-Ag shell nanoparticle tip for tip-enhanced spectroscopy. *Analyst* **2016,** *141* (17), 5066-5070.

Chapter 2

Fabrication and Characterization of Highly Reproducible Colloidal Nanoantennas

2.1. Introduction

Tip-enhanced Raman spectroscopy (TERS) is a powerful optical technique for chemical mapping that has the potential to achieve quantitative spectroscopic analysis of arbitrary surfaces with nanoscale resolution.[1, 2] TERS combines ultrasensitive vibrational spectroscopy with scanning probe methods by using a nanoscale metal tip to raster a surface. Upon irradiation, the metal tip behaves like an optical antenna to facilitate near-field amplification of both the incident and Raman-scattered light. By scanning this tip laterally across a surface, TERS enables the point-by-point acquisition of chemical information-rich Raman spectra with spatial resolutions from a few tens of nanometers down to < 1 nm.[3-6] Unlike other optical methods that yield super-resolution images or electron and X-ray mapping techniques, TERS is inherently label-free, nondestructive, and can be performed under ambient conditions. As such, TERS is well-suited for probing highly sensitive samples, such as single molecules,[3, 7, 8] nanostructures,[5, 9, 10] and biological surfaces.[7] However, the resolution and sensitivity of TERS readouts is highly dependent on the near-field enhancements provided by the nanoscale metal feature at the tip apex.[11-13] Understanding and engineering probe structures with sufficient optical quality and regularity remains a major obstacle in the implementation of TERS.

To achieve large near-field enhancements, TERS probes must possess a sharp radius of curvature, on the order of a few tens of nanometers or less.[11] The metal tip must possess the appropriate size and shape such that it exhibits maximum field confinement of light near the incident wavelength. In addition, tips must be resilient to

both mechanical damage incurred by contact with the sample surface and thermal damage incurred by laser irradiation.[14, 15] There are currently two approaches to TERS probe fabrication. The first approach uses methods such as electrochemical etching of an all-metal wire or physical vapor deposition (PVD) of metals such as silver or gold onto an atomic force microscopy (AFM) probe.[16, 17] These methods tend to produce tips with arbitrary nanoscopic features, leading to the difficulties in characterizing or reproducing optical measurements for which TERS is notorious. While recent studies have shown improvements in etching Au tips with consistent shapes at the micro- and nanoscale,[18, 19] they have not led to consistent optical field enhancements. The second approach uses top-down fabrication techniques such as focused ion beam milling[20, 21] and induced deposition mask-lithography[22] to generate engineered nanoantenna with specific plasmonic properties.[23] However, top-down methods encounter difficulties in producing reliable features < 10 nm due to the surface roughness generated by templated metal deposition.

Here we demonstrate TERS probes that are fabricated by assembling shaped, colloidal metal nanoparticles onto an AFM probe to generate a nanoantenna structure. When brought into contact with a metal substrate, the nanoparticles form a high quality plasmonic cavity that supports a coupled resonance mode. Using colloidal Ag nanocubes (AgNC), we are able to engineer these cavities to possess strong resonances in the visible to near-infrared range. We have found that these cavities produce Raman enhancements of 10^9, far surpassing the sensitivity of other TERS probes. AgNCs synthesized using solution-based methods[24] are ideal optical probes because they

exhibit localized surface plasmon resonances in the visible spectrum, and because these optical resonances are highly tunable with AgNC size. Additionally, unlike bulk metal wires or evaporated metal films, colloidal AgNCs are single-crystalline with nearly atomically smooth faces, which results in better near-field enhancements due to decreased boundary scattering and phonon-electron relaxation rates.[25, 26] Colloidal nanoparticles are also synthesized in milliliter to liter volumes, a process that can be readily scaled for manufacturing.

2.2. Results and Discussion

2.2.1. Nanoantenna Characterization and Validation

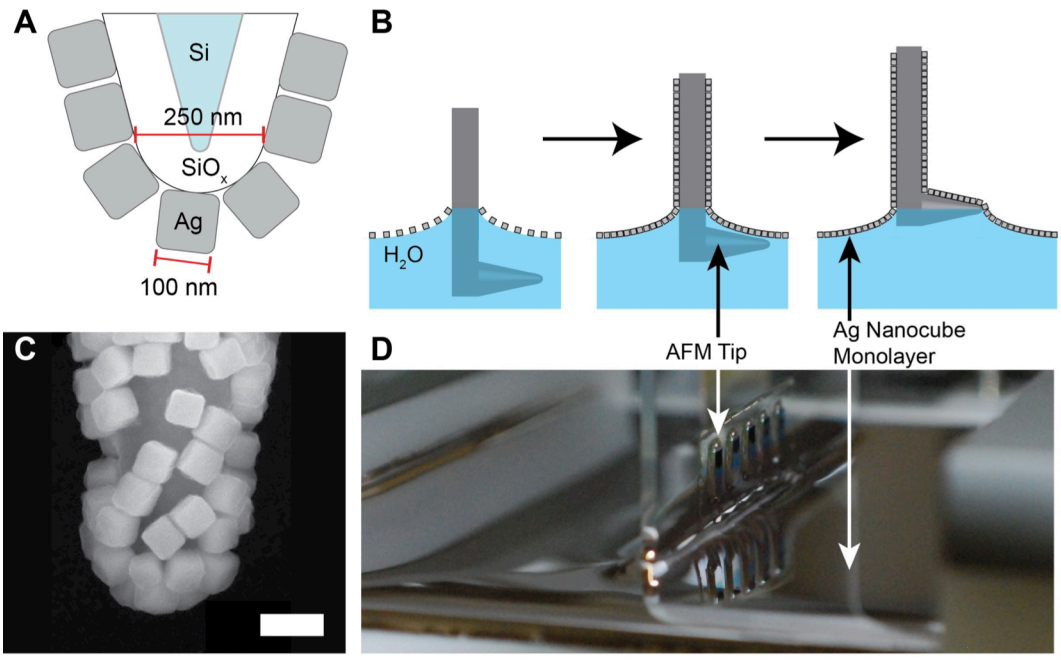

Figure 2.1. Fabrication process of colloidal nanoantenna. (A) Commercial AFM probe is coated with a layer of SiO_2 *via* PECVD to increase the radius. It is then coated with a continuous film of AgNCs. (B) Langmuir-Blodgett film of AgNCs is compressed to a monolayer and then transferred *via* mechanical dip coating to an AFM tip. (C) SEM image at high magnification (scale bar 200 nm) of a colloidal nanoantenna showing a uniform layer of AgNCs coating the surface. (D) Photograph showing multiple AFM tips simulateously coated with a monolayer of AgNCs.

We fabricate colloidal nanoantennas by depositing a close-packed monolayer of colloidal AgNCs onto commercially available Si AFM cantilevers. Figure 2.1.A,C shows a schematic and a scanning electron microscope (SEM) image of the colloidal nanoantenna. Using the Langmuir-Blodgett method (LB), AgNCs are deposited at an air-water interface and then isothermally compressed to form a highly ordered monolayer (Figure 2.1.B,D). A mechanical dipper then transfers the film to an AFM probe. SEM imaging confirms that AgNCs are deposited uniformly on the probe and that they remain in a close-packed configuration during film transfer.

Figure 2.2. shows that the radius of curvature (ROC) of the AFM tip plays an important role in the quality of the AgNC assembly on our colloidal nanoantenna. We found that the ROC must be on the order of AgNC size in order to ensure that multiple

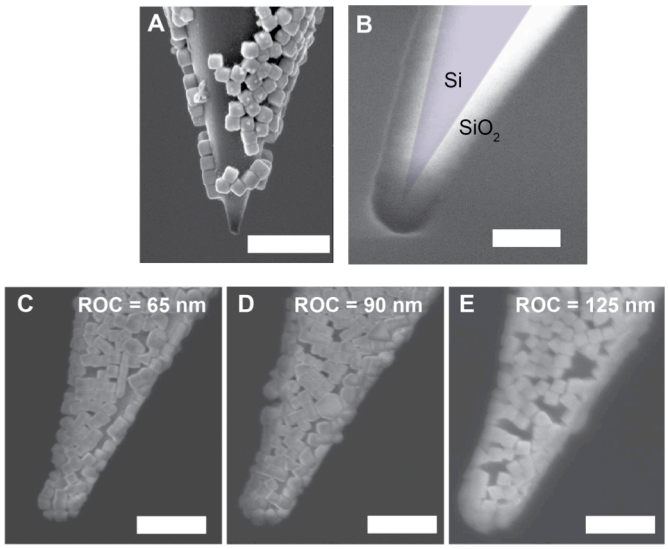

Figure 2.2. Modifying the radius of curvature of an AFM probe before AgNC deposition. (A) SEM image of an unmodified AFM probe after a monolayer of AgNCs was deposited. Excessively sharp probes cannot support an AgNC monolayer. (B) SEM image showing the comparison between an unmodified (false color overlay) AFM probe and an AFM probe with a PECVD SiO_2 layer resulting in a 125 nm curvature. (C-E) SEM images of AgNC monolayers deposited on PECVD SiO_2 modified AFM probes with (C) 65 nm ROC, (D) 90 nm ROC, and (E) 125 nm ROC. Scale bars in A,C-E are 500 nm, B is 200 nm.

AgNCs are seated at the AFM tip apex (for mechanical stability), but that only one protrudes further than the others (for maximum field confinement). For extremely sharp AFM tips with a radius of curvature <10 nm, AgNCs do not deposit at the apex because the sharp tips destructively pierce the AgNC monolayer during the dip-coating process (Figure 2.2.A). Therefore, we coat Si probes with a thin layer of SiO_2 by plasma-enhanced chemical vapor deposition (PECVD) to produce a tip with a controlled radius of curvature. Parts C-E of Figure 2.2. show examples of colloidal nanoantenna fabricated with 65, 90, and 125 nm ROC resulting from differing oxide thicknesses.

A molecular self-assembled monolayer (SAM) of 1-hexadecanethiol (HDT) is reacted with the AgNC surfaces to displace any polyvinylpyrrolidone (PVP) on the Ag surface that remains from the nanoparticle synthesis. The SAM also protects the AgNCs against oxidation and other contamination.[27]

To measure the field enhancement of these colloidal nanoantennas, we collected Raman scattering spectra for SAMs of thiophenol (PhSH) molecules on a supported Ag thin-film. Figure 2.3.A shows a schematic of the TERS experiment. Nanoantennas were mounted into an AFM and the apex was illuminated through an optically coupled Raman spectrometer. The distance between the nanoantenna and the Ag thin-film is controlled by a piezoelectric stage; when the nanoantenna is brought in contact with the Ag film, the supported SAM serves as a dielectric gap between the AgNC located at the nanoantenna apex and the underlying metal film. This nanoscale gap supports a highly confined optical resonance that leads to a large enhancement of

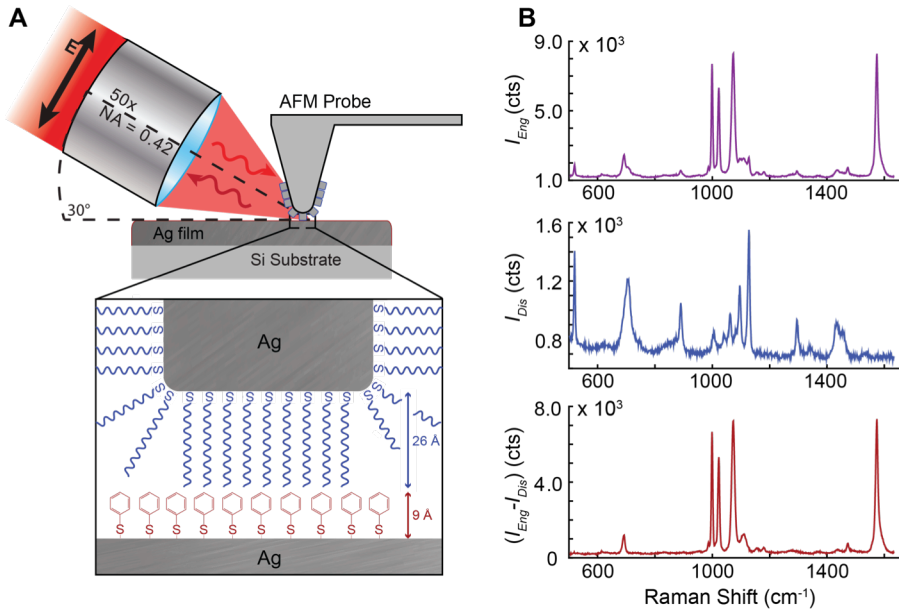

Figure 2.3. Experimental setup and TERS collection. (A) Colloidal nanoantenna are placed in an AFM and operated in contact mode. The substrate investigated is a SAM of PhSH on an Ag surface. A SAM of HDT protects the surface of the AgNCs deposited on the AFM probes from oxidation and contamination. (B) Raman spectra with the nanoantenna (top) engaged to a PhSH SAM on an Ag thin-film (I_{eng}). (middle) Raman spectra with the nanoantenna removed from the PhSH monolayer substrate by ≈ 100 nm (I_{dis}). (bottom) I_{eng} - I_{dis} . Spectra were taken at 785 nm, 1.5 mW, and 10 s integration time.

Raman scattering intensities. A typical Raman spectrum obtained by measuring scattering off of our colloidal nanoantenna is shown in Figure 2.3.B (top). When the nanoantenna is engaged to the Ag surface, we observe Raman scattering peak intensities (I_{eng}) that correspond to the vibrational modes for Si, HDT, and PhSH (See Table 2.1.). When the nanoantenna is disengaged from the surface by approximately 100 nm, we observe Raman scattering peak intensities (I_{dis}) corresponding only to Si and HDT (Figure 2.3.B, middle). Figure 2.3.B (bottom) shows the Raman spectrum obtained by subtracting I_{eng}- $I_{dis,}$ which shows Raman peaks for only PhSH. Most notable are the 999 cm^{-1} out-of-plane ring stretch, $\nu(C\text{-}C)_{Ring}$, and the 1574 cm^{-1}

symmetric C-C stretch, $\nu(C\text{-}C)_S$, which exhibit little overlap with the vibrational modes for Si and HDT.

Table 2.1. Vibrational Mode Assignments of PhSH, HDT, and silicon

Peak Location (cm^{-1})	**Parent Molecule**	**Peak Assignment**
520	Silicon	Lattice vibration
681, 690	HDT, PhSH	ν(C-S)
1000	PhSH	$(\text{Ring breathing})_{op}$, 12a
1024	PhSH	$(\text{Ring breathing})_{ip}$, 18a
1075	PhSH	Ring breathing & ν(C-S), 18b
1096, 1127	HDT	ν(C-C)
1154, 1184	HDT	ν(C-C)
1297, 1340	HDT	$\omega(CH_2)$
1575	PhSH	$\nu(\text{C-C})_{sym}$, 8a

To examine the near-field nature of this Raman enhancement, we plotted the intensities (I_{eng}) of these peaks as the analyte substrate was moved toward the nanoantenna stepwise in 2 nm increments. The AFM feedback voltage — which depends on the deflection of the cantilever — was used to verify the location of the nanoantenna relative to the Ag film (Figure 2.4.A). A slope of zero indicates that the nanoantenna is disengaged (*i.e.,* substrate movement yields no cantilever deflection). As the substrate approaches the nanoantenna, the snap-in force pulls the nanoantenna into contact with the substrate[28], and shows as a discontinuity in the AFM feedback voltage. Further movement of the substrate will deflect the cantilever and change the feedback voltage linearly with distance. We define effective distance (d_{eff}) as the distance the Ag film has traveled in either direction from the measured snap-in position. A positive d_{eff} is the distance separating the nanoantenna and the Ag film,

whereas a negative d_{eff} is generated by movement of the Ag film that applies an additional force to the cantilever.

From the plots in Figure 2.4.B-E, we define three regimes of I_{eng}: substrate approach, nanoantenna engagement, and deflection of the cantilever by the substrate. The intensities of the Si and HDT peaks remain constant at 538 ± 17 and 180 ± 20 counts/mW·s, resectively, since the laser remains focused on the nanoantenna apex. However, peak intensities associated with PhSH change drastically. For d_{eff} = 2–20 nm, the peak intensities for $\nu(C\text{-}C)_S$ and $\nu(C\text{-}C)_{ring}$ remain constant at 6 ± 7 and 7 ± 12 counts/ mW·s, respectively. These intensities increase just prior to the snap-in of the nanoantenna and engagement with the substrate at d_{eff} = 2 nm, which is consistent with other reported TERS simulations[29, 30] and experiments.[31, 32] From d_{eff} = -4–-26 nm, the peak intensities of $\nu(C\text{-}C)_S$ and $\nu(C\text{-}C)_{ring}$ have values of 423 ± 108 and 358 ± 50 counts/mW·s, respectively.

As the nanoantenna is deflected by the substrate beyond d_{eff} = -15 nm, the average Raman intensity increases for both vibrational modes of PhSH. Because this increase has been observed for multiple nanoantenna, we believe it is not an artifact of our probe fabrication (Figure 2.5.). This intensity increase may result from a number of effects related to an increased deflection of the cantilever. These effects may include: (i) conformational changes of the PhSH molecules within the SAM, (ii) changes in the optical near-field distribution due to bending of the cantilever, or (iii) changes in the optical near-field due to nanoscopic deformation or movement of the AgNC located at the apex with increased pressure from the substrate. We can rule out

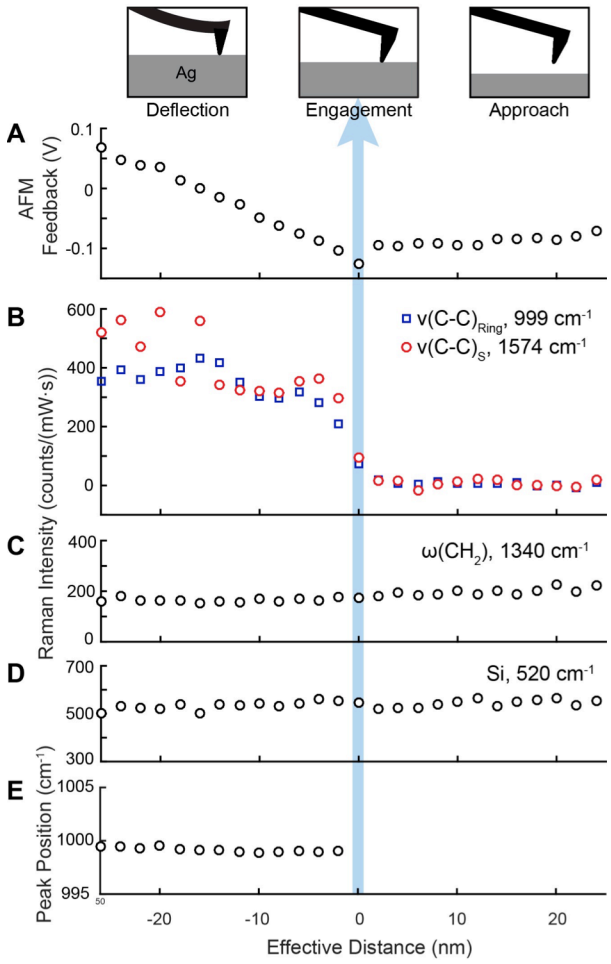

Figure 2.4. TERS near-field effect as a function of tip-sample distance. (A) AFM feedback voltage as a function of effective distance from the Ag surface. The nanoantenna engages the surface at an effective distance of 0 nm (blue arrow), verified by a drop in feedback voltage indicating "snap-in". (B) Intensity of PhSH peaks as a function of effective distance from the Ag surface. (C-D) Intensity of HDT and Si Raman peaks as a function of effective distance from the Ag surface. (E) Peak Position of the PhSH 999 cm-1 peak as a function of effective distance from the Ag surface. Measurements taken using a 633 nm laser line at 400 μW and with a 5 s integration time.

the first effect since the pressure applied at the AgNC-substrate interface is likely too low to induce any significant conformational change of the PhSH molecules. We use the equations for the deflection of a cantilever with one fixed end and one free end to calculate applied force:

$$\delta = \frac{FL^3}{3EI} \qquad (2.1.)$$

$$\theta = \frac{FL^2}{2EI} \qquad (2.2.)$$

where δ is the deflection of the cantilever at the free end, θ is the bending angle of the cantilever at the free end, E is Young's modulus, I is the moment of inertia, and F is the applied force. When δ is -60 nm (d_{eff}, a distance that is generously larger than the d_{eff} we employed for most of our experiments), we estimate that the maximum pressure applied at the nanoantenna apex would be 1.0 GPa (5 nm radius of applied pressure). Previous studies have reported that the wavenumber for the vibrational modes of PhSH will blue-shift linearly with pressure by a few tens of wavenumbers.[33]

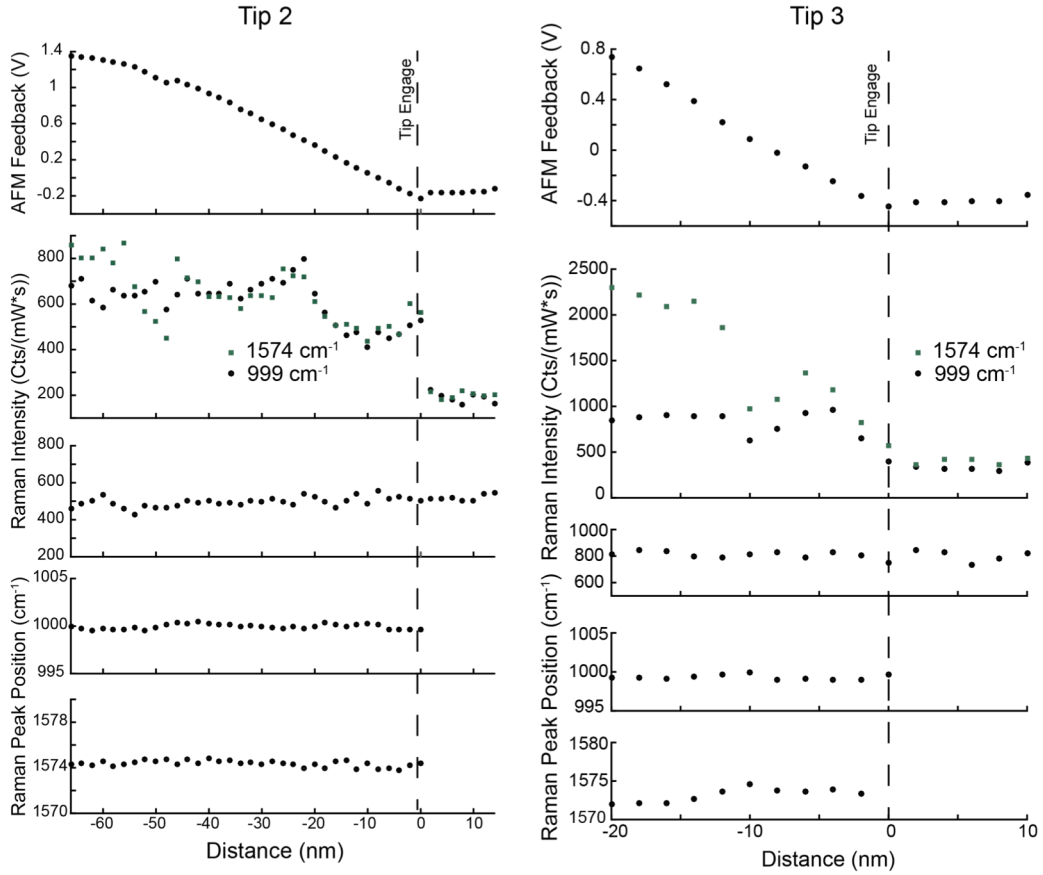

Figure 2.5. Additional tips showing the TERS near-field effect. Tip 2) engaged over 2 nm, tested over 60 nm engaged, 785 nm 150 uW 5s integration times. Tip 3) engaged over 8 nm, 785 nm 150 uW 5s integration times. Both show a PhSH intensity increase while HDT intensity is constant, bottom figures show peak positions of 999 cm^{-1} and 1574 cm^{-1}, and no change in their positions.

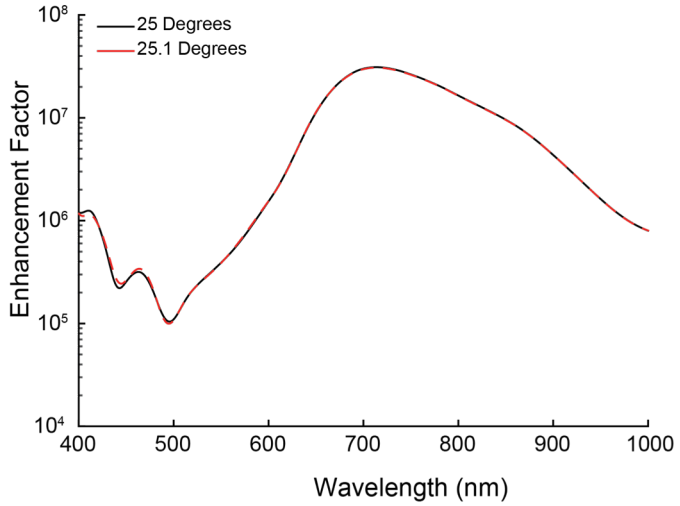

Figure 2.6. The effect of AgNC rotation on Raman EF. The black line shows a 25 degree tilt along the primary tilt axis (Figure 3C), the red line shows a 25.1 degree tilt, a larger change than we would expect from normal cantilever bending during engage.

Figure 2.4.E and 2.5. show no shift in wavenumber for the 999 cm^{-1} PhSH vibrational mode. Similarly, no shift was observed for any of the PhSH vibrational modes. To rule out contributions from cantilever bending, we estimate using equation 2.2. that the nanoantenna apex rotates by approximately 0.02° during deflection. Simulations indicate that this rotation is unlikely to result in any measurable effect on Raman enhancement (Figure 2.6.). The third effect is the most likely cause of the observed change in I_{eng}. Applying strain has been observed to alter the near-field distributions associated with plasmonic Ag nanostructures.[34] Applied pressure may also cause minor slipping of the metal nanoparticles on the oxide-coated nanoantenna.

2.2.2. Experimental Determination of Enhancement Factor

Using our colloidal nanoantenna, we achieved Raman enhancement factors (EFs) ranging from 10^5 – 10^9 depending on the excitation wavelength. Figure 2.7. shows tip-engaged and tip-disengaged spectra taken with a single nanoantenna probe

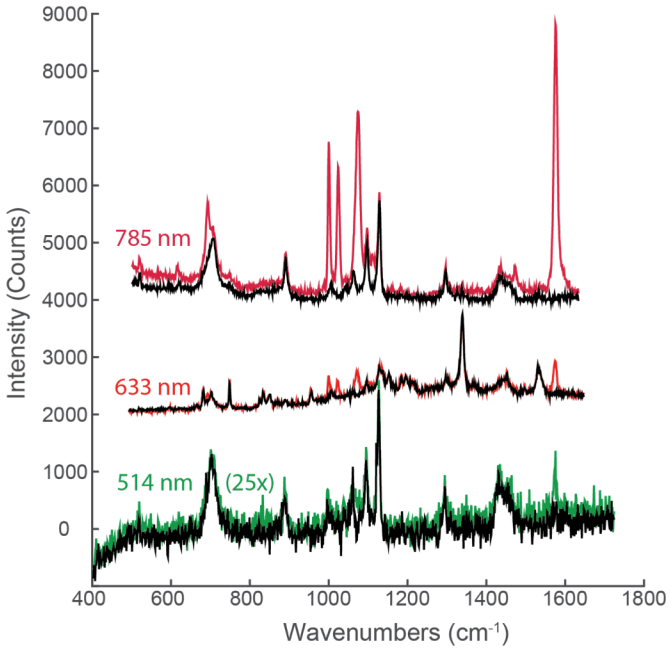

Figure 2.7. TERS engaged and disengaged spectra shown for each of the three experimental laser wavelengths used: 785, 633, and 514 nm. It shows the relative strength of the C16H33SH to the PhSH spectral peaks

(shown in the SEM images in Figure 2.8.B, C) using three different laser excitation wavelengths: 785 nm, 633 nm, and 514 nm. Figure 2.8.A shows the subtracted TERS spectra. We obtained the highest I_{eng} with an EF = 5.5 ± 2.0 x 10^8 using the 785 nm laser line. The other two laser lines gave EF = 1.3 ± 0.4 x 10^7 for 633 nm and EF = 9.7 x 10^5 for 514 nm (See section 2.4. for detailed EF calculations). Similar experiments were repeated for 16 different nanoantennas probes under 633 nm excitation and 20 different nanoantennas probes under 785 nm excitation. Raman scattering obtained from 514 nm excitation was very weak and was only detected for the single nanoantenna discussed in Figure 2.8A. Our results demonstrate that the average EF for our nanoantennas is in the range of 10^8–10^9 using the 785 nm laser line and in the range of 10^6–10^7 for the 633 nm laser line (raw data is listed in Appendix A). In a separate experiment, we fabricated 10 nanoantenna probes in parallel and evaluated

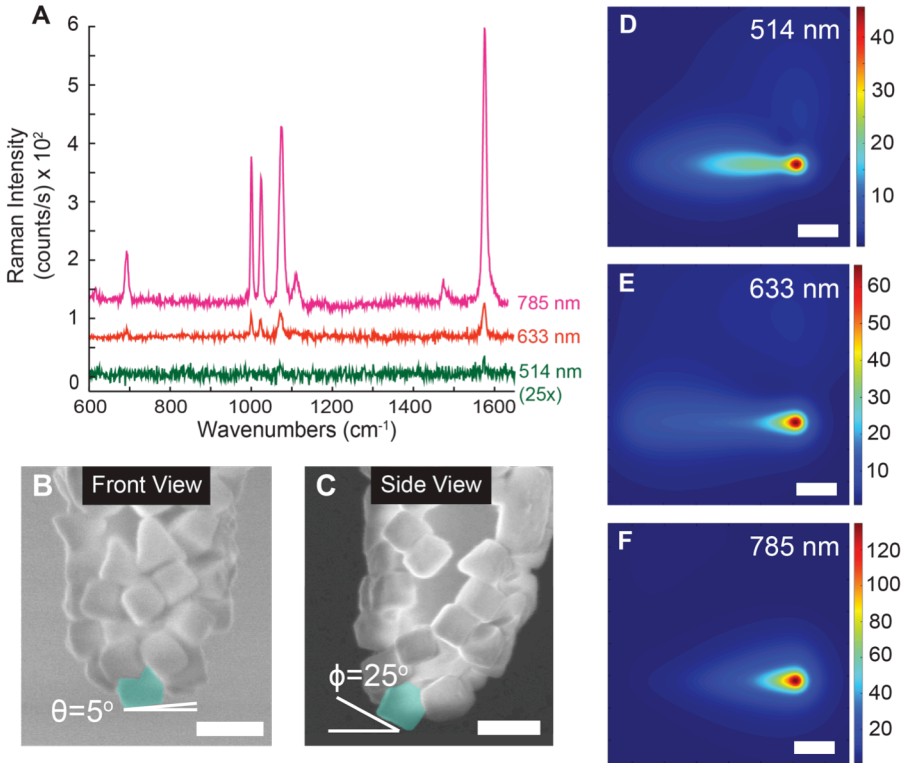

Figure 2.8. TERS wavelength-dependent field-enhancement. (A) TERS spectra collected at different laser excitation wavelengths for the colloidal nanoantenna shown in (B,C) (514 nm is multiplied 25x to identify the 1574 cm^{-1} $I_{stretch}$ peak). (B,C) SEM images of a colloidal nanoantenna with the apex AgNC false colored for visual clarity (scale bars 200 nm). (D-F) Field enhancement in the plane between the apex AgNC, and the substrate was determined from a simulation based on the orientation of the apex AgNC shown in B,C (scale bars 25 nm). Measurements taken for 785, 633, and 514 nm excitation were taking with respective power and time: 800 µW & 10s, 80 µW & 10s, 60 µW & 10s. Note: laser spot size for the 785 nm is significantly larger than the other excitation wavelengths, justifying the use of a higher power.

the EF of each nanoantenna under 785 nm excitation. Eight out of the 10 nanoantennas resulted in an EF between $1.0 \times 10^8 - 2.8 \times 10^9$, while two nanoantennas were only weakly Raman active or completely inactive (Appendix A, nanoantennas 20-27). In addition, we compared batch reproducibility using a single AgNC sample. We fabricated 36 nanoantennas in five separate batches. Of these nanoantenna, 28 (78%) were TERS active and 23 exhibited suitable EFs to acquire chemical maps.

2.2.3. Electrodynamic Modeling of Nanoantenna

We generated electrodynamic models of the colloidal nanoantenna showing that these large EFs result from a single, intense electromagnetic hotspot supported by a single AgNC located at the nanoantenna apex. SEM images (Figure 2.8.B,C) of the nanoantenna were used to determine the geometry and orientation of the AgNC that is most likely in contact with the substrate upon nanoantennaengagement (highlighted in false color). We generated a finite-difference time-domain (FDTD) model of this AgNC (See section 2.4, Figure 2.14.). Large TERS signals are attributed to the excitation of a resonant gap mode generated by plasmon coupling between the AgNC and the Ag substrate. When the Ag substrate is substituted with a dielectric such as SiO_2, this gap mode is no longer supported (Figure 2.9.A). Figure 2.8.D-F shows the calculated electric field distributions for a cross-section taken 1 nm above the Ag surface. Our model predicts the most intense electric field localization for 785 nm excitation, which shows a near-field strength of E/E_o = 135. This is also consistent with our experimental results. A recent study found that clusters of unconnected

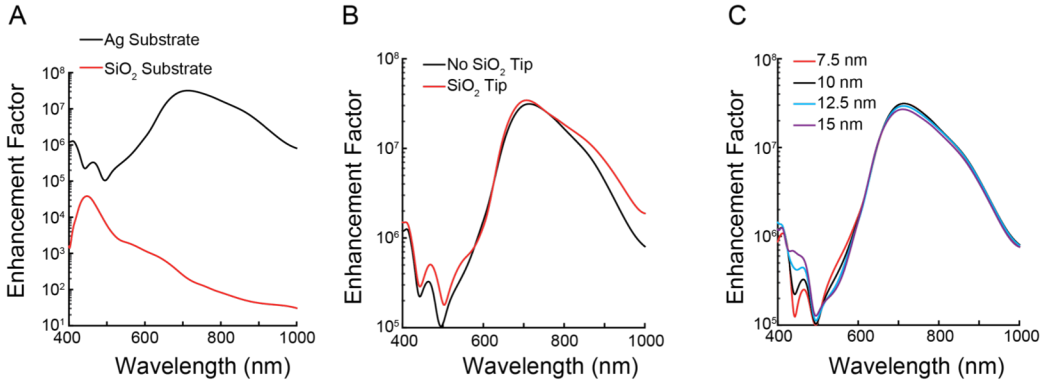

Figure 2.9. FDTD EF control simulations of a single 115 nm cube oriented as in Figure 2.8. (A) EF simulation showing the dependence of substrate material: Ag (black line) and SiO_2 (red line). (B) EF simulation showing the dependence on the presence of the SiO_2 tip. (C) EF simulation showing the dependence on AgNC corner radius.

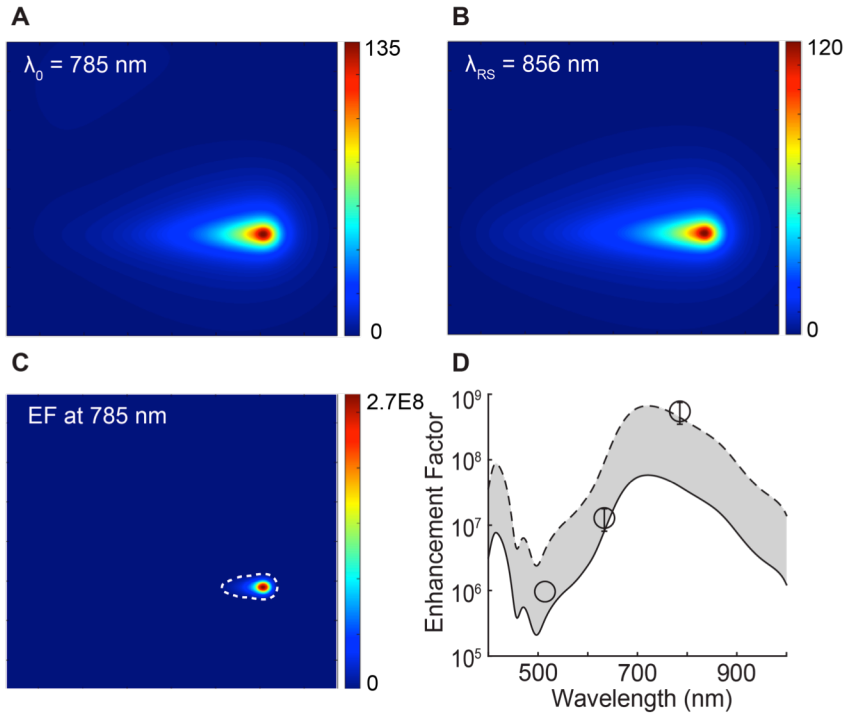

Figure 2.10. TERS EF determination. (A-B) Field enhancement resulting from the apex AgNC solved at (A) the excitation wavelength of 785 nm and (B) 856 nm, the 999 cm^{-1} Raman shifted wavelength. Simulations were carried out for the nanocube geometry shown in Figure 2.8. (simulation geometry is shown in Figure 2.14.). (C) Calculated EF, the dashed white line shows the hotspot area from which the average EF is calculated. (D) Average EF determined over the visible spectrum: gray area is the simulated Raman enhancement region, the lower bound is the simulated electromagnetic (EM) and the upper bound is the simulated EM + chemical EF, circles are the experimentally determined EF.

nanoparticles on an AFM tip support a unique waveguiding mode that increases the maximum TERS intensity and redshifts the optical resonance of the tip.[35] This is discussed in detail in Chapter 3. Additional models show that the inclusion of the Si/SiO_2 AFM tip or that varying the sharpness of AgNC corners has minimal effect on the predicted near-field intensities (Figure 2.9.B,C).

We calculated the expected Raman EF for our colloidal nanoantenna over a wavelength range of 400-1000 nm, which is expected to reach a maximum at 733 nm.

To determine the EF at a given wavelength, we first calculated the EF for each pixel in the near-field distribution map using the equation:

$$EF = \left(\frac{E_{Incident}}{E_0}\right)^2 \left(\frac{E_{Raman\ Shift}}{E_0}\right)^2 \quad (2.3)$$

The EF was calculated for the 999 cm^{-1} vibrational mode of PhSH. Figure 2.10.A,B shows the near-field distribution maps for the incident wavelength and the Raman-shifted wavelength for the 999 cm^{-1} mode; similar near-field maps were obtained over the entire wavelength range of interest. Figure 2.10.C shows the spatial dependence of the calculated EF for 785 nm excitation, as determined from the E/E_0 values in Figure 2.10.A,B. For visual clarity, the calculated EF is only shown within the hotspot area, which we defined as the region from which 90% of the Raman signal originates and is considered a conservative estimate of the EF. For example, we determined the hotspot area to be 598 nm^2 for 514 nm excitation, 249 nm^2 for 633 nm excitation, and 302 nm^2 for 785 nm excitation. We then determined the average EF — the metric most representative of the experimental data — by dividing the sum of all EF values within the hotspot by the total hotspot area. The average EF value was calculated at each wavelength over the visible spectrum. The results are plotted in Figure 2.10D (black line) against our experimentally calculated EFs (black circles). The discrepancy between our experimental and theoretical EF values is attributed to a deficiency in our FDTD models, which only accounts for electromagnetic enhancement of Raman scattering. It is well-known that Raman scattering intensities also experience a chemical enhancement, which can arise from molecular resonances or an increase in

polarizability due to surface adsorption. For PhSH monolayers that are chemisorbed to Ag surfaces, a chemical EF≈11 is expected.[36] Taking into account both the chemical and electromagnetic EFs increases the overall EF and reduces the discrepancy between our measured and predicted values (Figure 2.10.D, dotted line). Another possibility is that a waveguiding mode could contribute to an unexpectedly high EF. Alternatively, it is possible that other inaccuracies in our FDTD model —with the tip-to-substrate gap distance, measured AgNC size, or the bulk Ag dielectric function— may contribute to this discrepancy.

2.2.4. Performance and Comparison of Colloidal Nanoantenna to Other Probes

Figure 2.11. shows the comparison of the EFs obtained for our colloidal nanoantenna to the EFs obtained from commercially available electrochemically etched Au wires operated in tuning fork feedback mode. The logarithmic values of the EFs are displayed for our colloidal nanoantenna at both 633 nm and 785 nm excitation and for the purchased etched Au wire probes at 633 nm excitation. All measurements were made on identically fabricated PhSH monolayers on Ag substrates. We measured the TERS performance of ten etched Au wire probes and found that only five gave measurable TERS signals. We calculated the average EF of these five probes to be 6.3 x 10^5 ± 7.4 x 10^5. The large error in EF likely stems from nanoscale morphological differences at the wire apices, a common problem with etched wire probes. We then measured the TERS performance of 16 colloidal nanoantenna and calculated their EFs to be 1.4 ± 1.3 x 10^7. Not only do our colloidal nanoantenna achieve EFs that are over

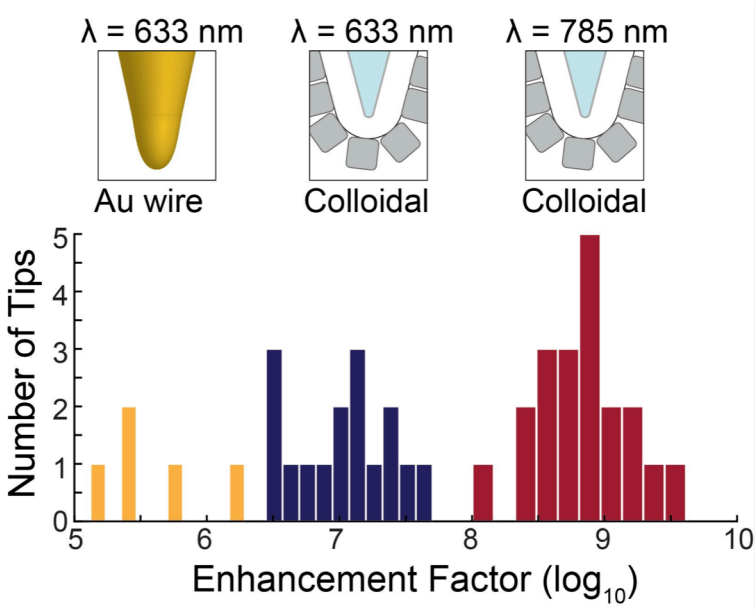

Figure 2.11. TERS reproducibility. Histogram showing the logarithmic values of EFs for colloidal nanoantenna excited at 785 nm (red bars), and 633 nm (blue bars). A direct comparison with an identical substrate and identical 633 nm illumination conditions was performed with etched Au wire TERS probes (yellow bars).

20 times higher than the commercial probes for 633 nm excitation and 1-2 orders of magnitude better for 785 nm excitation, but they also exhibit much lower deviations in EF with 78% of the colloidal nanoantenna resulting in measurable TERS enhancements. We attribute the consistency in EF amongst our colloidal nanoantenna probes to the broadband response of the gap plasmon mode, which is tolerant of variance in AgNC orientation and AgNC shape. We explore this in detail in Chapter 3.

TERS performance is also commonly gauged by measuring the signal-to-noise ratio (SNR). In 2014, A detailed reproducibility study was carried out across 13 different TERS instruments around the world.[37] They investigated the ability of different groups with different instrumentation and probes to identify a common analyte consisting of a PhSH SAM supported on an Au substrate. To compare TERS performance across all of the groups who were able to collect TERS data (only 7 out

of 13 groups), the authors devised a data normalization scheme that accounted for laser wavelength, power, integration time, number of acquisitions, numerical aperture, and illumination angle. This metric was applied to three probes per group and found that the average normalized SNR for the 999 cm^{-1} peak ranged from 0.5 – 160. One group had a single Ag probe give an outlier response with a normalized SNR of 1052. To compare our results with the results obtained by Blum et al., we tested 16 nanoantenna at 633 nm excitation and attained an average normalized SNR = 360 ± 256. We additionally tested 15 nanoantenna at 785 nm excitation and obtained a normalized SNR = 598 ± 381, with a single outlier nanoantenna possessing a SNR = 7043.

2.2.5. Colloidal Nanoantenna Demonstrate Sub-Diffraction Chemical Imaging

To further demonstrate the efficacy of assembled AgNC probes, we used our colloidal nanoantenna to map a chemical surface by TERS. We patterned an Ag substrate with two different molecular monolayers — 1,1':4',1"- Terphenyl-4-thiol (TPT), and Thiophenol (PhSH)— using soft contact lithography (Figure 2.12.A).[38] SEM images verify that the stripe pattern was successfully transferred to the Ag surface (Figure 2.13.A). Confocal Raman maps taken of the patterned substrate provide no evidence of the chemical patterns and exhibit Raman scattering intensities that are too low to distinguish either molecular component of the heterogeneous pattern (Figure 2.13.B). When we collect TERS spectra perpendicularly to the patterned substrate however, a clear variation in chemical spectra is present (Figure

2.12.B). The blue and red spectral peaks represent TPT and PhSH respectively. Orange and green peaks are attributed to the AgNC SAM and the Si probe respectively. Spectra were taken with a linear step of 39 nm and well below the Abbe diffraction limit of 280 nm (for a 785 nm light source). At some stripe edges, two mutually exclusive spectra are observed, indicating that the resolution of the TERS probe is at least as good as the step size. Other stripe edges display a mix of the

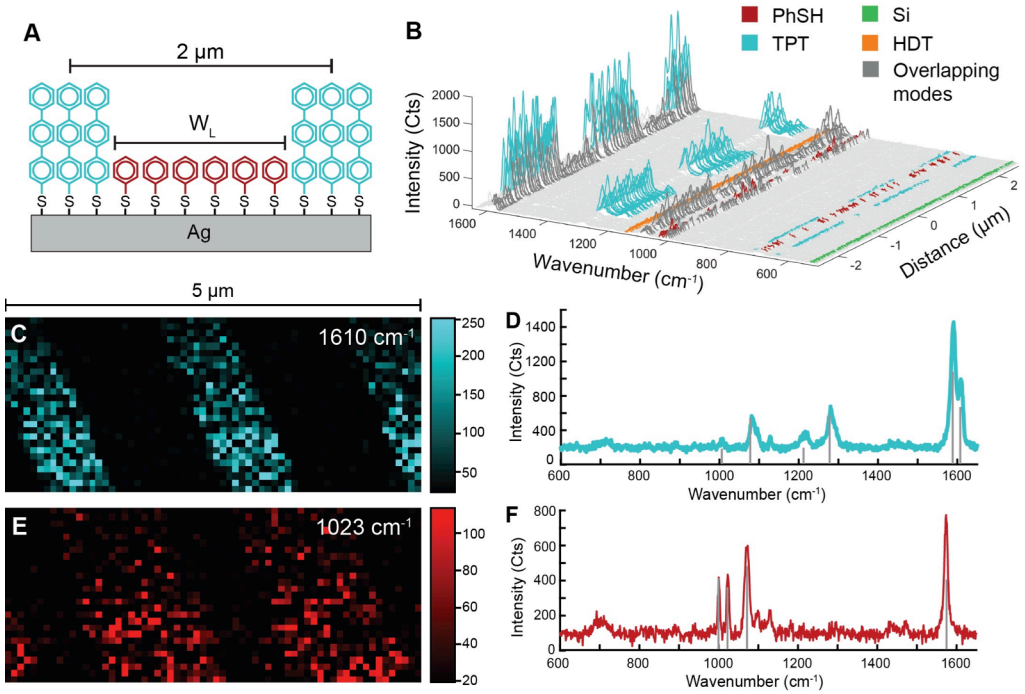

Figure 2.12. TERS map of patterned heterogeneous SAM. (A) Cartoon of a patterned Ag thin-film with TPT (stamped molecule, blue), and PhSH (backfilled molecule, red), the pitch is 2 µm, and the width of individual lines varies between substrates. (B) Hyperspectral linescan across the stripped pattern. Blue peaks represent TPT, while red peaks represent PhSH. Orange and green peaks represent HDT and Si, respectively. The stripe pattern can clearly be identified with a 39 nm step size. (C) TERS map and representative spectra (D) of the stamped molecule on the Ag substrate. The map is 5 x 2.5 µm, and has a pixel size of 78 nm x 78 nm. (E) TERS map and representative spectra (F) of the backfilled molecule (PhSH). Spectra for B were collected with an excitation wavelength of 785 nm, at a power of 1.5 mW, and a 0.3 s integration time, while C-F were collected with a 1 s integration time.

spectra suggesting a diffusion region where the two components have mixed. While we expect the nanoantenna to produce spatial resolution significantly less than shown here, patterned molecular monolayers are not likely able to identify spatial resolution below the 39 nm step size presented here as it would become convoluted with the diffusion region.

Figure 2.12.C,E show the TERS map collected using a colloidal nanoantenna scanned over the patterned Ag substrate. Each pixel is 78 x 78 nm. The color scale bars encompass > 98% of the intensity ranges that were collected in our TERS experiments. Figure 2.12B shows a TERS map generated by plotting the intensity of the ring vibrational mode at 1610 cm^1, which is unique to TPT. The maps show an average stripe width of 837 ± 24 nm, which is consistent within the range of stamped substrates. Figure 2.12.D shows a TERS map generated by plotting the intensity of the

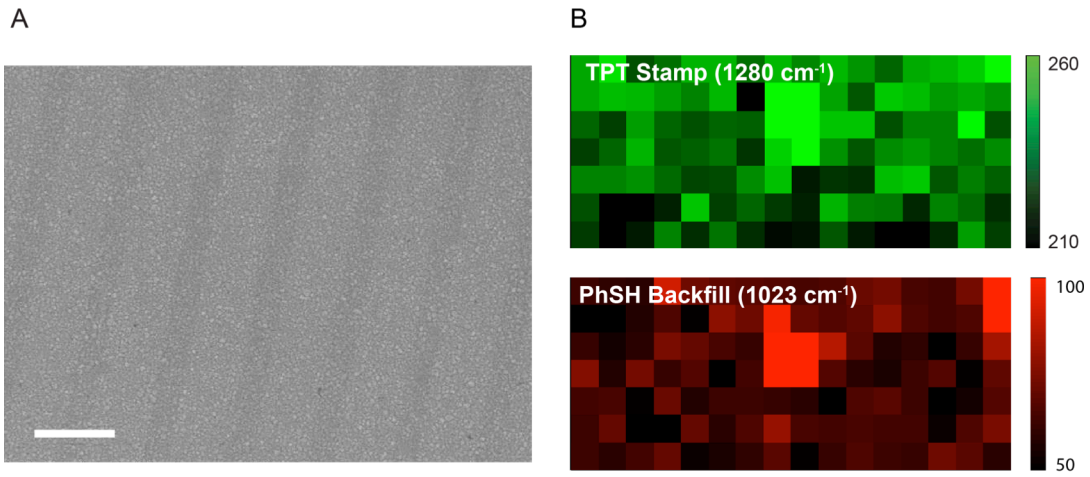

Figure 2.13. Characterization of the patterned substrate by (A) SEM (scale bar = 2 μm), and (B) confocal Raman measurements plotting peak intensities for (top) TPT, and (bottom) PhSH. Images are 8 x 21 μm. The nonzero intensities result from background fluorescence of the Ag substrate due to long exposure times.

$\nu(C\text{-}C)_S$ mode at 1023 cm^{-1}, which is unique to PhSH. While the stripe pattern in both maps are clearly visible, the TERS intensity varies significantly from pixel to pixel. In some cases, the TERS intensities are low enough that they appear as dark pixels in the map. We believe this fluctuation in TERS intensity is due to surface roughness of the Ag substrate that results from the deposition process. Using AFM, we measured the Ag surface roughness parameter to be R_{RMS} = 2.7 nm with $R_{Max\text{-}Min}$ = 17.7 nm. It has previously been reported that surface roughness can contribute significantly to TERS enhancement variation.[39] This intensity fluctuation can be alleviated by using ultra-flat metal surfaces to increase the signal uniformity, as is seen in Figure 2.12.B when a template-stipped Ag thin-film is substituted for the rougher, sputtered Ag.

2.3. Experimental and Computational Methods

AgNC Synthesis: AgNCs mean edge length (70-100 nm) are prepared via a polyol synthesis described previously.[24] Briefly, $AgNO_3$ is heated and reduced in 1-5 pentanediol. $CuCl_2$ and Polyvinylpyrrolidone (PVP, MW = 55,000) are added to control nucleation and growth process, and to surface passivate the AgNCs after growth. The AgNCs are then vacuum-filtered (Millipore Durapore membranes with 650 nm, 450 nm, then 220 nm pore sizes) to reduce the size dispersity of the particles by selectively removing larger, non-cubic particles. AgNCs are repeatedly centrifuged in ethanol to remove excess polymer and finally suspended in $CHCl_3$.

Colloidal Nanoantenna Fabrication: Colloidal nanoantenna are fabricated by coating Ag NCs on the surface of commercially available AFM tips: Olympus AC240TS-R3 or NT-MDT VIT_P_C-A. Ag NCs are deposited onto the AFM tip via

Langmuir-Blodgett trough (KSV Nima KN2001), as described previously.[40] The film is compressed at a rate of 5.8 cm^2/min to a surface pressure of Π = 12-18 mN/m. The AFM tips are drawn vertically through the monolayer film via mechanical dipper at a rate of 1.0 mm/ min and allowed to dry in air. PVP is displaced from the Ag NC surface by a self-assembled monolayer (SAM) of alkylthiols. The probes are submerged overnight in a 1 mM ethanolic solution of 1-hexadecanethiol (HDT, Sigma-Aldrich). The tips are then thoroughly rinsed in ethanol and dried under a stream of N_2. They are stored under vacuum until use, within 24 hours.

Au Etched Wire Probes were obtained commercially from Bruker Nano Inc.

Substrate Preparation: Thiophenol (PhSH) SAM on Ag thin-film: Si (100) was sonicated in ethanol and dried under a stream of N_2. It was then cleaned for 60 s in a 100 W RF Ar plasma (Denton Discovery). A 50 nm Ag film was sputtered (50 W, 2 mtorr Ar). Ag substrates were then immersed in 100 μM ethanolic solution of PhSH (Sigma Aldrich) overnight, then rinsed with ethanol and dried under a stream of N_2 to remove any excess thiol ligand. PhSH on Ag thin-film substrates are stored under vacuum until use, within 24 hours.

Patterned TPT with backfilled PhSH on Ag thin-film: An SU-8 master mold was fabricated using standard photolithography. The mask consists of an array of lines with a pitch of 2 μm, with individual line thicknesses varying depending on applied pressure and wear on the master. After silanization of the master, PDMS was poured over the master, and cured overnight at 60° C. The PDMS stamp was removed from the master and inked with a 10 mM ethanolic solution of TPT for 60 s and dried with

N_2. Full contact between the stamp and Ag was ensured (In the case of Figure 2.13.B, an ultra-flat Template-stripped (TS) Ag thin-film was used, 100 nm thickness), but no further pressure was applied. The stamp remained in contact for 10 – 15 s. The remaining exposed Ag was backfilled by covering the surface with a 50 μL droplet of 10 mM ethanolic solution of PhSH for 10 s. The patterned Ag substrate was then rinsed with copious amounts of ethanol and dried with N_2.

TERS Equipment and experiments: A commercial Raman/AFM (Renishaw inVia/Bruker Innova) system was used for all experiments in this study. The TERS objective is set at 60 degrees to normal (Figure 2.3.) with an ELWD 50x objective, NA = 0.42. The objective was controlled with three orthogonal, independently controlled stepper motors with 0.1 μm step size. Measurements were taken at powers between 80-1500 μW. 785 nm illumination was provided by a Renishaw 300 mW stripe diode laser. 633 nm illumination was provided by a Renishaw 17mW HeNe laser. 514 nm illumination was provided by a Modu-Laser 50 mW Ar+ Ion laser. A modified Bruker IRIS head with a 980 nm diode feedback laser was used for 785 nm measurements to prevent interference with the OEM 830 nm broadband feedback diode. All TERS measurements were taken in contact mode. To prevent contamination and/or degradation, colloidal TERS nanoantennas are imaged under a UHR SEM only after all TERS data is collected.

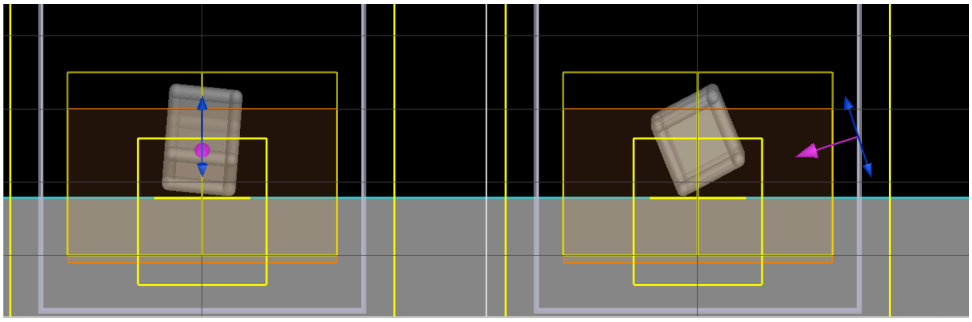

Figure 2.14. FDTD of a 115 nm AgNC showing (left) the XZ plane, and (right) the YZ section. The nanocube is rotated 25 degrees along the Y-axis and 5 degrees along the X-axis. The nanocube corners have a 10 nm radius. The orange rectangle is the 1 nm mesh volume, and the purple/ blue arrows are the light propagation and polarization respectively. The horizontal yellow line beneath the cube is the area from which electric field data is measured.

FDTD Simulations: Electromagnetic (EM) modeling was performed with Lumerical FDTD Solutions to determine computational EF. AgNCs (Palik[41] dielectric data) were modeled in 3 dimensions with a flat silver film as a substrate. A 3 nm spacer was added with index of refraction (n) = 1.4 to reflect the organic SAM spacers. Incident light was 72° to normal with s-polarized light. A 1 nm global mesh was used with a 0.5 nm local mesh at the junction added to improve accuracy. Control simulations were carried out with a 1 nm global mesh only. Figure 2.15. shows the difference between the simulations, we observe a uniform increase in EF without affecting the qualitative nature of the plasmonic response. The model was solved from 300-1500 nm. The electric field enhancements were calculated in the plane of the Ag film, offset 1 nm vertically.

Enhancement Factor Calculations: We determined experimental EFs by comparing the TERS spectral intensity of PhSH (I_{TERS}) to the bulk Raman spectral intensity of neat PhSH (I_{Raman}) and dividing by the number of molecules in the hot

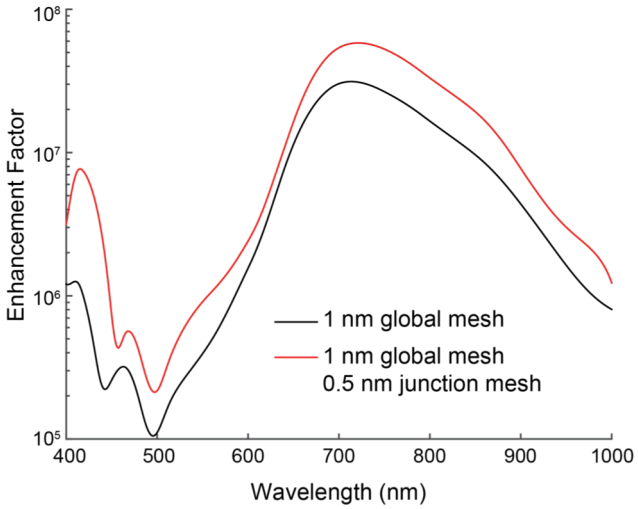

Figure 2.15. FDTD EF Simulations of a single 115 nm cube as shown in Figure 2.8. The red line uses an improved (0.5 nm) mesh at the cube substrate junction and provides an increased EF that is fairly uniform over the spectrum. The black line shows the model used as the standard for control experiments in Figures 2.9.

spot area(N_{TERS}) and laser focal volume respectively (N_{Raman}) according to the equation:

$$EF = \left(\frac{I_{TERS}}{I_{Raman}}\right)\left(\frac{N_{Raman}}{N_{TERS}}\right) \qquad (2.4)$$

The laser spot size was calculated using the scanning knife-edge method. A cleaved Si wafer edge was scanned over the laser spot in both X and Y directions and the 520 cm^{-1} peak intensity was recorded over the length of the scan. The plots were fitted to error functions and the Gaussian beam waists derived. Focal Depth was calculated by translating the Si along the z-axis, with the focal plane in the center. This was fitted to a Gaussian and the focal depth was taken as the integral (-inf, inf) of the fit. N_{Raman} was calculated using the density and molecular weight of bulk PhSH. N_{TERS} was calculated from the hotspot area defined by simulation, multiplied by the literature packing value for PhSH SAMs of 6.8 molecules/ nm^2.[42] I_{Raman} and I_{TERS} were taken with the same experimental configuration and power setting, and then normalized for

integration time. The enhancement factor was calculated using the 999 cm^{-1} peak because it displays low orientational dependence on intensity,[43] and is therefore less affected by molecular reordering on a metal surface. In addition it displays the highest bulk Raman signal (by a factor of > 5) and so gives us the most conservative EF calculation.

Experimental error analysis:

Fig 2.2. - Error is calculated as the standard deviation of peak value within each regime described, as determined by the feedback voltage.

Fig 2.3. - EFs were calculated from ≥ 3 spectra taken at random locations on a PhSH on Ag thin-film (powers and times for each tip are listed in Table S3). Error in the TERS performance, was calculated only from the deviation between the acquired spectra, and ignores error within the normal Raman spectra, which is < 5% and does not contribute to our understanding of tip intensity deviation.

Signal-To-Noise (SNR): Noise was taken as the average value of a blank spectral region, usually 50 cm^{-1} wide, with a spectral resolution of ~ 1 cm^{-1}, equaling about 50 data points. SNR was calculated by dividing the Peak height of the designated peak by the Noise level for that spectrum.

2.4. Conclusions

In conclusion, we have demonstrated that colloidal nanoantennas serve as high-quality TERS probes that produce significantly large, reproducible, and predictable Raman EFs. While nanoparticle-based probes have been explored in previous studies on either TERS or near-field scanning optical microscopy, the ability

to fabricate nanoantennas *via* the bottom-up assembly of metal nanocrystals is enabling. We expect that the combination of ease of fabrication and unprecedented reliability in batch-to-batch TERS readouts will make colloidal nanoantenna ideal for chemical mapping with nanoscale spatial resolution.

Chapter 2 is a reformatted reprint in full, of the material from: **Dill, T. J.**, Rozin, M. J.; Palani, S.; Tao, A. R., Colloidal Nanoantennas for Hyperspectral Chemical Mapping." *ACS Nano* 2016, 10 (8), 7523-7531. The dissertation author was the principal researcher and author of this paper.

2.5. References

1. Bailo, E.; Deckert, V., Tip-enhanced Raman scattering. *Chemical Society Reviews* **2008,** *37* (5), 921-930.

2. Pettinger, B.; Ren, B.; Picardi, G.; Schuster, R.; Ertl, G., Nanoscale Probing of Adsorbed Species by Tip-Enhanced Raman Spectroscopy. *Physical Review Letters* **2004,** *92* (9), 096101.

3. Steidtner, J.; Pettinger, B., Tip-Enhanced Raman Spectroscopy and Microscopy on Single Dye Molecules with 15~nm Resolution. *Physical Review Letters* **2008,** *100* (23), 236101.

4. Stadler, J.; Schmid, T.; Zenobi, R., Nanoscale Chemical Imaging Using Top-Illumination Tip-Enhanced Raman Spectroscopy. *Nano Letters* **2010,** *10* (11), 4514-4520.

5. Chen, C.; Hayazawa, N.; Kawata, S., A 1.7 nm resolution chemical analysis of carbon nanotubes by tip-enhanced Raman imaging in the ambient. *Nat Commun* **2014,** *5*.

6. Zhang, R.; Zhang, Y.; Dong, Z. C.; Jiang, S.; Zhang, C.; Chen, L. G.; Zhang, L.; Liao, Y.; Aizpurua, J.; Luo, Y.; Yang, J. L.; Hou, J. G., Chemical mapping of a single molecule by plasmon-enhanced Raman scattering. *Nature* **2013,** *498* (7452), 82-86.

7. Tallarida, N.; Rios, L.; Apkarian, V. A.; Lee, J., Isomerization of One Molecule Observed through Tip-Enhanced Raman Spectroscopy. *Nano Letters* **2015,** *15* (10), 6386-6394.

8. Sonntag, M. D.; Klingsporn, J. M.; Garibay, L. K.; Roberts, J. M.; Dieringer, J. A.; Seideman, T.; Scheidt, K. A.; Jensen, L.; Schatz, G. C.; Van Duyne, R. P., Single-Molecule Tip-Enhanced Raman Spectroscopy. *The Journal of Physical Chemistry C* **2012,** *116* (1), 478-483.

9. Hayazawa, N.; Yano, T.; Watanabe, H.; Inouye, Y.; Kawata, S., Detection of an individual single-wall carbon nanotube by tip-enhanced near-field Raman spectroscopy. *Chemical Physics Letters* **2003,** *376* (1–2), 174-180.

10. Bao, W.; Borys, N. J.; Ko, C.; Suh, J.; Fan, W.; Thron, A.; Zhang, Y.; Buyanin, A.; Zhang, J.; Cabrini, S.; Ashby, P. D.; Weber-Bargioni, A.; Tongay, S.; Aloni, S.; Ogletree, D. F.; Wu, J.; Salmeron, M. B.; Schuck, P. J., Visualizing nanoscale excitonic relaxation properties of disordered edges and grain boundaries in monolayer molybdenum disulfide. *Nat Commun* **2015,** *6*.

11. Demming, A. L.; Festy, F.; Richards, D., Plasmon resonances on metal tips: Understanding tip-enhanced Raman scattering. *The Journal of Chemical Physics* **2005,** *122* (18), 184716.

12. Richards, D.; Milner, R. G.; Huang, F.; Festy, F., Tip-enhanced Raman microscopy: practicalities and limitations. *Journal of Raman Spectroscopy* **2003,** *34* (9), 663-667.

13. Barbry, M.; Koval, P.; Marchesin, F.; Esteban, R.; Borisov, A. G.; Aizpurua, J.; Sánchez-Portal, D., Atomistic Near-Field Nanoplasmonics: Reaching Atomic-Scale Resolution in Nanooptics. *Nano Letters* **2015,** *15* (5), 3410-3419.

14. Zhang, W.; Schmid, T.; Yeo, B.-S.; Zenobi, R., Near-Field Heating, Annealing, and Signal Loss in Tip-Enhanced Raman Spectroscopy. *The Journal of Physical Chemistry C* **2008,** *112* (6), 2104-2108.

15. Agapov, R. L.; Sokolov, A. P.; Foster, M. D., Protecting TERS probes from degradation: extending mechanical and chemical stability. *Journal of Raman Spectroscopy* **2013,** *44* (5), 710-716.

16. Ren, B.; Picardi, G.; Pettinger, B., Preparation of gold tips suitable for tip-enhanced Raman spectroscopy and light emission by electrochemical etching. *Review of Scientific Instruments* **2004,** *75* (4), 837-841.

17. Hayazawa, N.; Inouye, Y.; Sekkat, Z.; Kawata, S., Metallized tip amplification of near-field Raman scattering. *Optics Communications* **2000,** *183* (1–4), 333-336.

18. Kharintsev, S. S.; Noskov, A. I.; Hoffmann, G. G.; Loos, J., Near-field optical taper antennas fabricated with a highly replicable ac electrochemical etching method. *Nanotechnology* **2011,** *22* (2), 025202.

19. Kharintsev, S. S.; Hoffmann, G. G.; Fishman, A. I.; Salakhov, M. K., Plasmonic optical antenna design for performing tip-enhanced Raman spectroscopy and microscopy. *Journal of Physics D: Applied Physics* **2013,** *46* (14), 145501.

20. De Angelis, F.; Das, G.; Candeloro, P.; Patrini, M.; Galli, M.; Bek, A.; Lazzarino, M.; Maksymov, I.; Liberale, C.; Andreani, L. C.; Di Fabrizio, E., Nanoscale chemical mapping using three-dimensional adiabatic compression of surface plasmon polaritons. *Nat Nano* **2010,** *5* (1), 67-72.

21. Ropers, C.; Neacsu, C. C.; Elsaesser, T.; Albrecht, M.; Raschke, M. B.; Lienau, C., Grating-Coupling of Surface Plasmons onto Metallic Tips: A Nanoconfined Light Source. *Nano Letters* **2007,** *7* (9), 2784-2788.

22. Cabrini, A. W.-B. a. A. S. a. M. S. a. B. H. a. D. F. O. a. P. J. S. a. S., Functional plasmonic antenna scanning probes fabricated by induced-deposition mask lithography. *Nanotechnology* **2010,** *21* (6), 065306.

23. Taminiau, T. H.; Moerland, R. J.; Segerink, F. B.; Kuipers, L.; van Hulst, N. F., λ/4 Resonance of an Optical Monopole Antenna Probed by Single Molecule Fluorescence. *Nano Letters* **2007,** *7* (1), 28-33.

24. Sun, Y.; Xia, Y., Shape-Controlled Synthesis of Gold and Silver Nanoparticles. *Science* **2002,** *298* (5601), 2176-2179.

25. Huang, W.; Qian, W.; El-Sayed, M. A.; Ding, Y.; Wang, Z. L., Effect of the Lattice Crystallinity on the Electron−Phonon Relaxation Rates in Gold Nanoparticles. *The Journal of Physical Chemistry C* **2007,** *111* (29), 10751-10757.

26. McPeak, K. M.; Jayanti, S. V.; Kress, S. J. P.; Meyer, S.; Iotti, S.; Rossinelli, A.; Norris, D. J., Plasmonic Films Can Easily Be Better: Rules and Recipes. *ACS Photonics* **2015,** *2* (3), 326-333.

27. Schmid, T.; Yeo, B.-S.; Leong, G.; Stadler, J.; Zenobi, R., Performing tip-enhanced Raman spectroscopy in liquids. *Journal of Raman Spectroscopy* **2009,** *40* (10), 1392-1399.

28. Carpick, R. W.; Salmeron, M., Scratching the Surface: Fundamental Investigations of Tribology with Atomic Force Microscopy. *Chemical Reviews* **1997,** *97* (4), 1163-1194.

29. Notingher, I.; Elfick, A., Effect of Sample and Substrate Electric Properties on the Electric Field Enhancement at the Apex of SPM Nanotips. *The Journal of Physical Chemistry B* **2005,** *109* (33), 15699-15706.

30. Yang, Z.; Aizpurua, J.; Xu, H., Electromagnetic field enhancement in TERS configurations. *Journal of Raman Spectroscopy* **2009,** *40* (10), 1343-1348.

31. Pettinger, B.; Domke, K. F.; Zhang, D.; Picardi, G.; Schuster, R., Tip-enhanced Raman scattering: Influence of the tip-surface geometry on optical resonance and enhancement. *Surface Science* **2009,** *603* (10–12), 1335-1341.

32. Neacsu, C. C.; Dreyer, J.; Behr, N.; Raschke, M. B., Scanning-probe Raman spectroscopy with single-molecule sensitivity. *Physical Review B* **2006,** *73* (19), 193406.

33. Brown, K. E.; Dlott, D. D., High-pressure raman spectroscopy of molecular monolayers adsorbed on a metal surface. *Journal of Physical Chemistry C* **2009,** *113*, 5751-5757.

34. Qian, X.; Park, H. S., Strain effects on the SERS enhancements for spherical silver nanoparticles. *Nanotechnology* **2010,** *21* (36), 365704.

35. Taguchi, A.; Yu, J.; Verma, P.; Kawata, S., Optical antennas with multiple plasmonic nanoparticles for tip-enhanced Raman microscopy. *Nanoscale* **2015,** *7* (41), 17424-17433.

36. Valley, N.; Greeneltch, N.; Van Duyne, R. P.; Schatz, G. C., A Look at the Origin and Magnitude of the Chemical Contribution to the Enhancement Mechanism of Surface-Enhanced Raman Spectroscopy (SERS): Theory and Experiment. *The Journal of Physical Chemistry Letters* **2013,** *4* (16), 2599-2604.

37. Blum, C.; Opilik, L.; Atkin, J. M.; Braun, K.; Kämmer, S. B.; Kravtsov, V.; Kumar, N.; Lemeshko, S.; Li, J.-F.; Luszcz, K.; Maleki, T.; Meixner, A. J.; Minne, S.; Raschke, M. B.; Ren, B.; Rogalski, J.; Roy, D.; Stephanidis, B.; Wang, X.; Zhang, D.; Zhong, J.-H.; Zenobi, R., Tip-enhanced Raman spectroscopy – an interlaboratory reproducibility and comparison study. *Journal of Raman Spectroscopy* **2014,** *45* (1), 22-31.

38. Libioulle, L.; Bietsch, A.; Schmid, H.; Michel, B.; Delamarche, E., Contact-Inking Stamps for Microcontact Printing of Alkanethiols on Gold. *Langmuir* **1999,** *15* (2), 300-304.

39. Zhang, W.; Cui; Yeo, B.-S.; Schmid, T.; Hafner, C.; Zenobi, R., Nanoscale Roughness on Metal Surfaces Can Increase Tip-Enhanced Raman Scattering by an Order of Magnitude. *Nano Letters* **2007,** *7* (5), 1401-1405.

40. Tao, A.; Sinsermsuksakul, P.; Yang, P., Tunable plasmonic lattices of silver nanocrystals. *Nature nanotechnology* **2007,** *2* (7), 435-440.

41. Palik, E. D., *Handbook of Optical Constants of Solids*. Academic Press: 1998.

42. McFarland, A. D.; Young, M. A.; Dieringer, J. A.; Van Duyne, R. P., Wavelength-scanned surface-enhanced Raman excitation spectroscopy. *Journal of Physical Chemistry B* **2005,** *109* (22), 11279-11285.

43. Ru, E. L.; Etchegoin, P., *Principles of Surface-Enhanced Raman Spectroscopy: and related plasmonic effects*. Elsevier Science: 2008.

Chapter 3

The Broadband Optical Response of Colloidal Nanoantenna Results from Interparticle Coupling

3.1. Introduction

Scanning probes that facilitate local optical measurements have enabled a variety of nanospectroscopy techniques, such as near-field scanning optical microscopy,[1-3] tip-enhanced Raman spectroscopy (TERS),[4-9] Tip-enhanced photoluminescence,[10, 11] and nano infra-red spectroscopy.[12-15] These techniques are capable of mapping surfaces and structures with nanometer resolution, making them particularly suitable for characterizing nanomaterials.[6, 16-19] TERS, in particular, is capable of providing rich chemical information through the collection of Raman scattering signals from highly confined nanoscale volumes. While TERS has the potential to become an invaluable analytical tool for probing both solid-state[10, 20-22] and biological surfaces,[23-26] TERS probe fabrication remains a large hurdle in using TERS for routine surface analysis and mapping. The optical responses of TERS scanning probes are highly dependent on probe tip geometry, material, and surrounding environment.[27-34] High performance probes can be attained by designing tips to support optical resonances (namely surface plasmon resonances) that are matched to the incident illumination wavelength and/or molecular resonances to enhance Raman signals.[17, 35, 36] A recent and thorough review by Fujita and co-authors describes various kinds of TERS probes that have been fabricated and demonstrated.[30] Probes fabricated by electrochemical etching of all-metal wires or fabricated by physical vapor deposition (PVD) of metals exhibit poor reproducibility of Raman enhancement. Engineered probes using e-beam lithography, focused-ion beam milling, template-stripping, and the attachment of colloidal metal nanostructures to sharp tips

have exhibited improvements both in TERS performance and enhancement reproducibility. Each of these probe types shows a different characteristic plasmonic response, (*e.g.* localized vs. propagating plasmons). It is clear that in order to engineer scanning probes that give rise to robust and consistent Raman scattering signals, a detailed understanding and thorough characterization of the plasmonic properties of the probe structure is critical.

Previous work has shown that TERS probes supporting a broadband optical resonance result in Raman signals that are less sensitive to minor defects in probe tip morphology.[11, 37, 38] One strategy to achieve such an optical response is by using closely-spaced metal nanoparticles to uniformly coat a scanning probe tip. Taguchi et al. recently demonstrated that physically separated Ag nanoparticles on an atomic force microscopy (AFM) tip support a broader plasmon resonance than does a single Ag nanoparticle on an AFM tip, with a TERS intensity maximized for a small number of nanoparticles located at the probe tip.[32] Lassiter et al. showed that cube-shaped nanoparticles deposited on a metal backplane result in a cavity plasmon whose fundamental resonance mode is in the visible wavelength range,[39]and Rozin et al. demonstrated that close-packed nanocubes display a similar behavior with the fundamental mode dramatically redshifted into the near-infrared due to interparticle coupling.[40] Inspired by these works, we recently employed a nanocube system for demonstrating TERS probes fabricated by self-assembly, where colloidal nanoantenna are generated by transferring a continuous film of colloidal Ag nanocubes (AgNC) onto a blunt AFM tip.[35] We observed that nearly 100% of colloidal nanoantenna with

AgNCs located at the probe tip apex were TERS active. While this suggests great potential for high-performance probes made by scalable fabrication, we were unable to identify the exact plasmon mode (e.g. localized vs. propagating plasmons) responsible for improved TERS performance. We hypothesized that the consistently large TERS signals observed in our experiments stemmed from a broadband localized surface plasmon resonance (LSPR), but were unable to measure this optical mode directly.

A combination of electrodynamic modeling and experimental efforts are needed to answer these questions regarding our colloidal TERS probes and their performance. For example, it is unclear whether our colloidal AgNC nanoantenna exhibit plasmonic behavior that is dominated by the effects of a continuous nanoparticle film, or of a single AgNC at the apex. Closely-spaced nanoparticle films have demonstrated long-range plasmon coupling in which energy can be transferred distances in excess of a micrometer, serving as an effective *plasmon waveguide*, and can be used to further increase near-field intensity in a local nanoscale region.[41-44] In a similar manner, close-packed AgNCs may be able to transfer energy from illuminated AgNCs located along the length of the AFM probe towards the tip apex. In addition, systematically varying probe tip geometries should be able to tease out which parameters are critical to TERS performance and elucidate plasmonic probe behavior. Examples include AgNC size, which is expected to have a greater effect on TERS probes in which single nanoparticle behavior is predominantly responsible for the enhanced field localization, and probe tip curvature (*i.e.* the radius of curvature (ROC)

of the underlying AFM tip), which is expected to significantly alter coupling between AgNCs.

In this work, we investigate the effects of AgNC edge length (*e*), tip ROC (*R*), and AgNC packing geometry on the near-field optical response of these colloidal nanoantenna (Figure 3.1.A,B). Our fabrication process enables us to readily control these fabrication variables, and we can validate electrodynamic finite-difference time-domain (FDTD) models with data from experimental prototypes of TERS probes. We employed self-assembled monolayers (SAM) of thiophenol (PhSH) adsorbed to an Ag thin-film as a standard Raman analyte to quantify the differences in Raman enhancement for various nanoantenna configurations. Figure 3.1.C shows a representative TERS spectra obtained from PhSH. We demonstrate that the robust performance of AgNC TERS probes results from the presence of multiple, close-packed AgNCs and that the broadband plasmon resonance responsible for the high Raman signals observed originate from long-range coupling between these close-

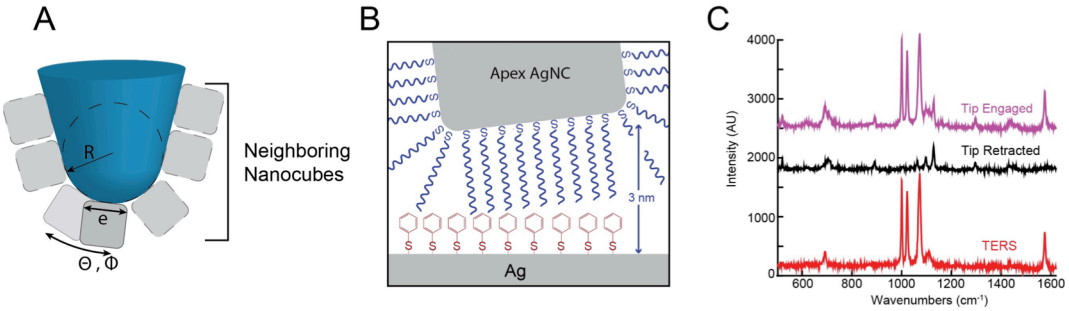

Figure 3.1. Colloidal nanoantenna geometric parameters and TER spectra (A) Schematic showing the variables affecting the optical response of colloidal nanoantenna: nanocube size (e), tip radius (R), orientation (θ, ϕ), relative placement to other nanocubes, and nanocube cluster size. (B) Schematic showing the gap region between the apex nanoparticle and the substrate. Monolayers of HDT and PhSH functionalize the AgNCs and Ag substrate respectively. (C) Representative Raman spectra showing (from top to bottom) the nanoantenna engaged to the Ag substrate, the nanoantenna withdrawn by roughly 150 nm from the surface, the retracted spectra subtracted from the engaged spectra.

packed AgNCs.

3.2. Results and Discussion

3.2.1. Plasmon Response of a Single AgNC Based Nanoantenna

Figure 3.2. shows the plasmon resonance expected for a colloidal nanoantenna where a single AgNC is brought in contact with an Ag surface (analyte substrate). To model this, we record the electric field enhancement in the plane parallel to the metal thin-film offset vertically by 1 nm. Figure 3.2.A shows a schematic of a simulated AgNC and the angles θ and ϕ that define its orientation relative to the surface by rotation around the X- and Y- axis respectively. In the shown configuration, the AgNC appears distorted because it is rotated at an angle θ and ϕ = 45°. From experimental characterization of AgNC probes by electron microscopy, it is unlikely that the apex AgNC on a colloidal TERS probe would be oriented perfectly tangential to the AFM tip at θ, ϕ = 0°. Figure 3.2.B shows the simulated electric field enhancement profile at 783 nm (chosen for its proximity to the experimental illumination wavelength of λ=785 nm that provided the highest TERS signals) for an AgNC with *e*=89 nm and oriented at θ=ϕ= 5°. At the probe apex, which we consider to be the AgNC corner closest to the substrate, a highly confined electric field is generated. This simulation shows that even small angular orientations are enough to localize the cavity resonance to a nanoscale region that is only a fraction the footprint of the actual AgNC. This is important because it has previously been shown that an AgNC placed flat on a metal surface with a nanometer sized gap generates a large cavity resonance originating from multiple reflections within the gap[45]. Such a cavity resonance occupies the entire

footprint of the AgNC and would result in poor spatial resolution for TERS measurements (e.g. limited by the size of the AgNC, ~70-100 nm).

Using field enhancement profiles for various AgNC sizes and orientations, we are able to calculate an average Raman enhancement factor (EF) at each wavelength (see Methods for detailed calculations). Figure 3.2.C shows average Raman EF over the wavelength range 400-1000 nm oriented at θ=ϕ= 5° for three different AgNC edge lengths, matching sizes made by colloidal synthesis: *e*= 74, 89, and 100 nm. From field distribution maps, these AgNCs result in respective hotspot radii of 12.4, 11.7, and 11.0 nm. Larger AgNC sizes significantly redshift the resonance peak. We also

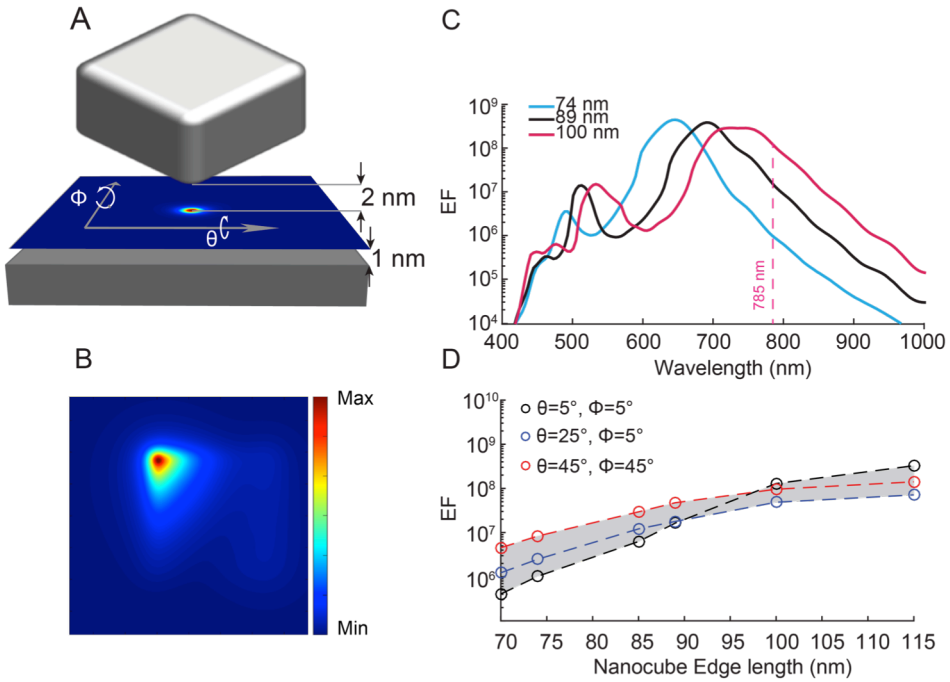

Figure 3.2. Single AgNC FDTD simulations. (A) Schematic showing a single AgNC oriented a θ and ϕ along the X and Y axis respectively relative to the substrate. The field enhancement is calculated 1 nm above the Ag substrate and 2 nm below the AgNC. (B) Field enhancement map showing the plasmonic hotspot beneath the nearest corner of the apex AgNC. The plane is solved at 785 nm for an 89 nm edge length AgNC with θ, ϕ = 45° (C) EF solved from 400 – 1000 nm for a 74, 89, and 100 nm AgNC with a θ, ϕ = 5°. The dashed line is located at 785 nm. (D) EF at 785 nm for AgNCs of edge lengths: 70, 74, 85, 89, 100, and 115 nm each solved at θ, ϕ = 5°; 25°, 5°; and 45°.

simulated a single AgNC ranging in size from 70 – 115 nm at three different angular orientations: low angular orientation ($\theta=\phi = 5°$), medium angular orientation ($\theta= 25°$, $\phi = 5°$) to high angular orientation ($\theta=\phi = 45°$). Figure 3.2.D shows the EFs calculated at the wavelength of 785 nm. The gray region shows the EFs expected with angular orientations not simulated, representing the expected variation in TERS measurements for probes fabricated with a given AgNC size. The effect of changing AgNC size is independent of the AgNC orientation: while changing angular orientation varies the Raman EF by a factor of 5, decreasing the AgNC size from 115 nm to 70 nm decreases the average EF by 2-3 orders of magnitude. This decrease indicates a strong dependence of the plasmon response on nanoparticle size over angular orientation.

3.2.2. Experimental Dependence of Raman EF on AgNC Size

To validate these models, we fabricated batches of colloidal nanoantenna using three different sizes of AgNCs: *e*=74 nm (8 nanoantenna, Figure 3.3.A), *e*=89 nm (8 nanoantenna, Figure 3.3.B), and *e*=100 nm (4 nanoantenna, Figure 3.3.C). We calculated the experimental TERS EF by performing multiple tip-in/tip-out measurements for each nanoantenna (see Methods for detailed calculations). The TERS EFs are plotted against the average AgNC size in Figure 3.3.D. There is no significant observed change in TERS EF over the size range investigated from 74- 100 nm AgNCs, which *disagrees with our single AgNC model*. This result suggests that more than a single AgNC located at the probe tip apex is responsible for the TERS response observed in our experiments.

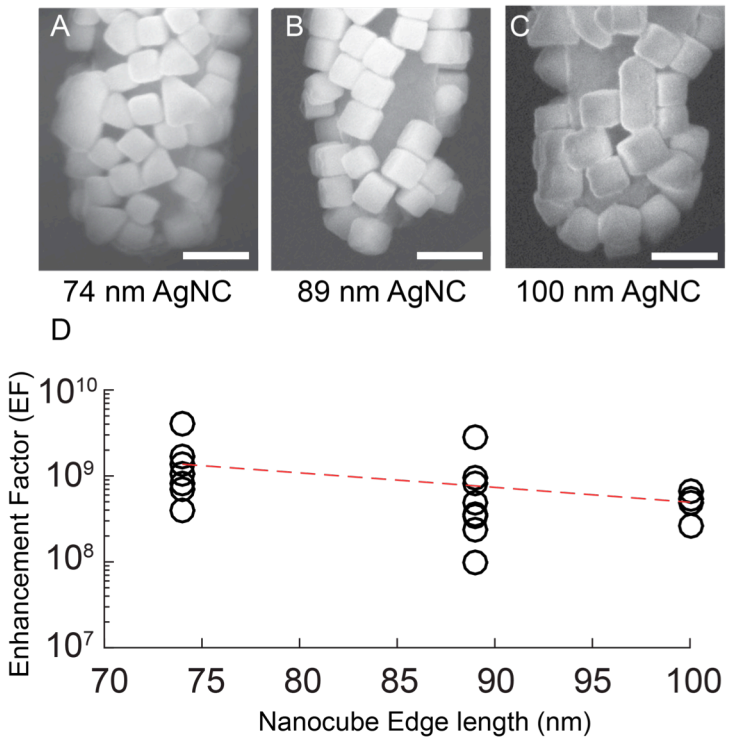

Figure 3.3. Experimental dependence of EF on AgNC size. (A-C) SEM Images showing colloidal nanoantenna fabricated with AgNCs of different mean edge lengths. (D) Experimental EFs for multiple colloidal nanoantenna at each of the different mean AgNC edge lengths (black circles), and the average EF over all tips measured for a given AgNC size (dashed line).

3.2.3. Contribution of Interparticle Coupling to the Plasmon Response of a Multi-AgNC Based Nanoantenna

Figure 3.4. shows the results of simulations using models that include multiple AgNCs in addition to the apex particle. We modeled clusters of 1, 5, 9, and 13 AgNCs (Figure 3.4.A) positioned on a Si AFM tip with R=125 nm. The apex AgNC was then placed 3 nm above an Ag thin-film (not shown). In our model, AgNCs were organized in a close-packed manner somewhat resembling a folded square lattice, with the condition a single AgNC be nearest the center of the probe apex, while remaining tangent to the tip surface. A 4 nm gap was introduced between the nearest points of

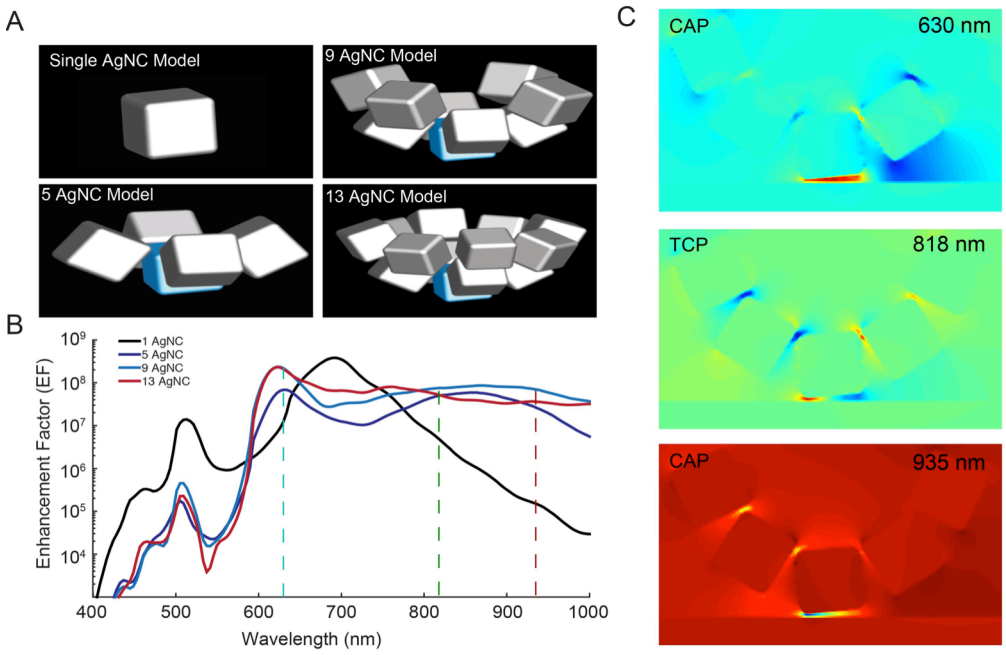

Figure 3.4. EF Dependence on number of nearest neighbor AgNCs the apex AgNC has. (A) Schematics of single, five, nine, and thirteen AgNC simulations (the apex AgNC is highlighted in blue for multiple AgNC simulations) All AgNCs have an edge length of 89 nm and the apex AgNC is at a θ and ϕ of 5° X 5° for all above simulations. (B) Wavelength dependent EFs for the simulations shown in (A). (C) Electric field profiles taken at a cross-section (along the plane of incidence) of the thirteen AgNC simulation at (from top to bottom) 630, 818, and 935 nm excitation.

adjacent AgNCs to accurately represent the spacing from the organic capping layer on the AgNC surface. The apex AgNC had an orientation of θ=ϕ=5° for each of the simulations. Figure 3.4.B shows the average EFs for each of the models in Figure 3.4.A. While the single AgNC model exhibits a single dominant resonance peak at 691 nm, the 5 AgNCs model shows two resonance peaks at 633 and 855 nm. When 9 AgNCs are modeled, the resonant peaks become broader, and the overall near-field optical response becomes flatter. When 13 AgNCs are modeled, individual resonant peaks are no longer distinguishable and a broadband response from 609 nm to >1000 nm remains.

This multi-nanoparticle response can be better understood by examining the plasmon modes associated with the gap between the AgNCs and the underlying metal substrate. A recent paper by Esteban et al. examines the plasmon modes associated with pairs of flat- and hemispherically-capped nanorods as they approach each other axially.[46] For flat-capped nanorods, two separate types of surface plasmon are identified. One is polarized perpendicular to the gap, between the nanoantennas, which is referred to as the longitudinal antenna plasmon (LAP). LAPs are excited by light components polarized perpendicular to the interparticle gap. These modes interact with the far-field and tend to be highly scattering. In the near-field, LAPs are characterized by having a single polarity on each side of the gap, like a plate capacitor or dipole-dipole coupled system. Transverse cavity plasmons (TCP) are polarized parallel to the gap. TCPs act like fabry-perot resonators and generate multiple reflections within the gap, leading to standing wave patterns. Importantly, TCPs can be excited by light components polarized in multiple orientations, including parallel to the interparticle gap. TCPs generated as a result of metal nanoparticles near metal films have been studied extensively.[39, 40, 45, 47] TCPs can lead to near-perfect absorption as well as high near-field enhancement over the entire footprint of the nanoparticle.

We assigned the LAC and TCP modes of the AgNC TERS antennas using the near-field distribution maps in Figure 3.4.B. The broadband plasmon response originates from interparticle coupling. The cross-section of a single AgNC oriented at $\theta=\phi=5°$ shows that the LAP serves as the dominant resonance peak at 691 nm. However, a weak TCP mode exists at higher wavelengths (Fig S1). Figure 3.4.C

shows a cross-section of the excitation plane from the 13 AgNC simulation for three different excitation wavelengths: 630, 818, and 935 nm. (Note that because these electric field profiles do not cross through the probe apex, they do not accurately represent either the intensity or the radius of the Raman hotspot.) Several LAP modes are observed when multiple AgNCs are present. Shown in Figure 3.4.C are LAP modes at 630 and 935 nm. Because resonances generated from interparticle coupling are red-shifted from their single AgNC equivalents, we attribute the shorter wavelength LAP at λ=630 nm to the apex AgNC, while the longer wavelength LAP at λ=935 nm likely results from interparticle coupling across multiple AgNCs. This is consistent with the larger full-width half-max of this LAP.[48] At intermediate wavelengths (λ=818 nm), we observe a TCP. The TCP mode is identifiable by the polarity flip across the gap (*i.e.* from red to blue). This near-field distribution map visibly displays the strong interactions between neighboring AgNCs for the TCP mode. Because the LSPR transitions from distinct peaks to a broadband response as AgNCs are added to the model, we suspect there is hybridization between the LAP

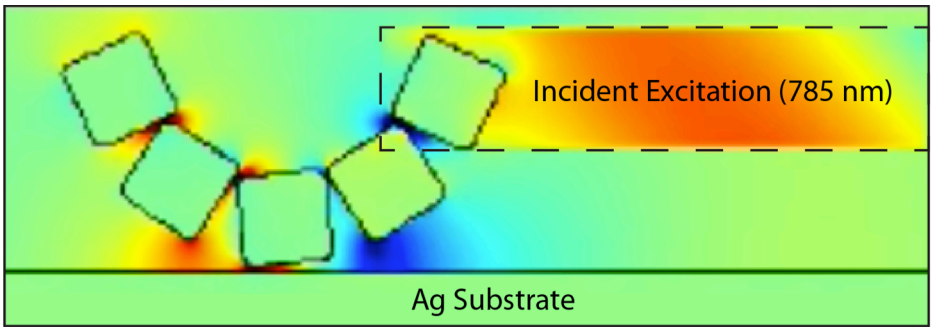

Figure 3.5. Cross-section of 13 AgNC simulation at 785 nm excitation when the apex AgNC is not illuminated. Only three of 13 AgNCs (top row) are illuminated by the incident light (dashed box). Energy transfer is observed between the remaining AgNCs showing a gap mode resonance still exists between the apex AgNC and the Ag substrate.

and TCP modes.

As previously discussed, interparticle coupling can also result in energy transfer *via* a waveguiding effect. By reducing the simulated excitation area to only illuminate three of the 13 AgNCs, we are able to directly observe energy transfer resulting from interparticle coupling. Without direct illumination of the apex AgNC, we observed a Raman hotspot similar (but weaker) to that of the fully illuminated simulation (Figure 3.5.). This demonstrates that in addition to hybridization of plasmon modes, additional energy transferred to the apex AgNC increases the TERS EF beyond the field generated by a single AgNC. Taken together, these simulation results suggest that interparticle coupling is responsible for new, hybridized plasmon modes that result in a broadband optical response and high local field enhancements at the probe apex.

Figure 3.6. shows how interparticle coupling accounts for our experimental observation that AgNC size has a negligible effect on TERS EF. We carried out simulations with 5 AgNCs; this model was chosen to conserve computational power while sufficiently demonstrating the nature of the new LAP and hybrid modes. Figure 3.6.A shows a schematic of the FDTD model. Figure 3.6.B shows an electric field enhancement profile using λ=783 nm excitation for five AgNCs with size=89 nm and with the apex AgNC oriented at $\theta=\phi=5°$. The Raman hotspot radii for these simulations ranged from 10.8 – 11.4 nm, very similar to the size of hotspots generated for single AgNCs. Figure 3.6.C shows the average TERS EFs over the range 450-1000 nm for AgNC probes with the same geometry, but with varying sizes of 74, 89, and

100 nm with the apex particle oriented at θ=ϕ=5°. The dashed line demarcates 785 nm and shows that for AgNCs in this size range, a 785 nm excitation laser lies within the broadband plasmon resonance, resulting in a relatively uniform EF. Figure 3.6.D plots the Raman EFs at 783 nm for five AgNC colloidal nanoantenna with AgNC sizes ranging from 70 – 115 nm and apex AgNC orientations of θ x ϕ =5°x5°; 25°x 5°; and 45°x45°. The average TERS EF factor varyies between 10^7-10^8 for varying AgNC orientation. However, the TERS EF neither increases nor decreases significantly with AgNC size. This is in contrast to single AgNC models but in agreement with our

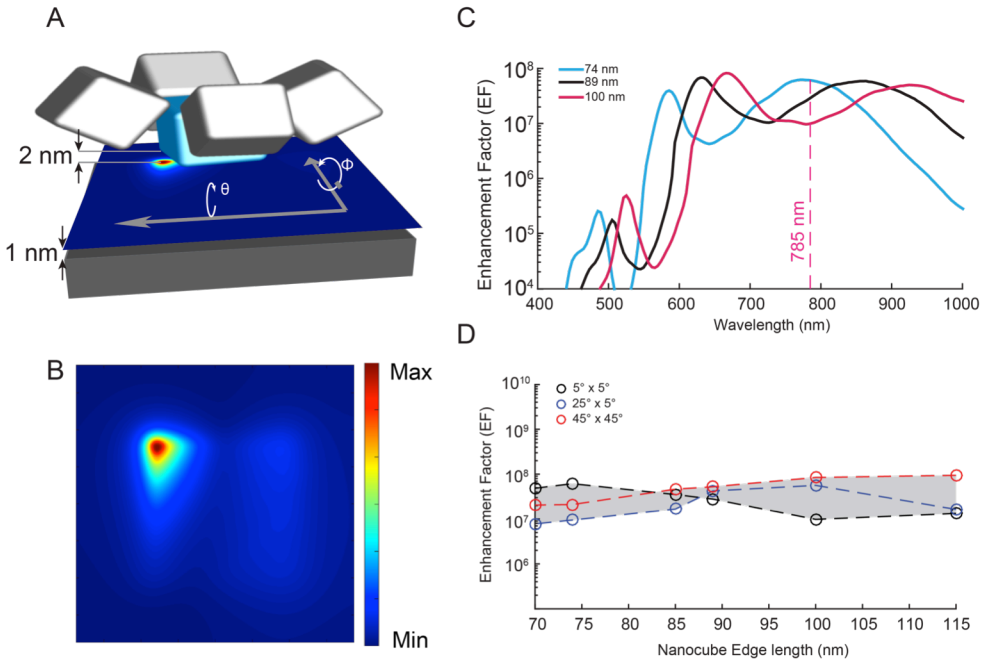

Figure 3.6. FDTD Simulations with four nearest neighbor AgNCs. The field enhancement is calculated 1 nm above the Ag substrate and 2 nm below the AgNC. (A) Schematic showing five AgNCs with the apex AgNC (highlighted in blue) oriented at θ and ϕ along the X and Y axis respectively relative to the substrate. Nearest neighbor AgNCs are placed tangent to a sphere (representing a AFM probe, radius 125 nm) with the nearest edge separated by 4 nm from the apex AgNC. (B) Field enhancement map showing the plasmonic hotspot beneath the nearest corner of the apex AgNC. The solution is at 785 nm for 89 nm edge length AgNCs with an apex AgNC orientation of θ, ϕ = 5° (C) EFs for five AgNC simulations, shown are AgNC edge lengths of 74, 89, and 100 nm AgNC with a θ and ϕ of 5° X 5°. The dashed line is located at 785 nm. (D) EF at 785 nm for AgNCs of edge lengths: 70, 74, 85, 89, 100, and 115 nm each solved with apex AgNC orientations of θ and ϕ of 5° X 5°, 25° X 5°, and 45° X 45°.

experimental observations.

Experimental control over probe tip ROC also allows us to investigate the effect of interparticle coupling and waveguiding effects on TERS EF. AFM tips are made blunt by PECVD oxide deposition, where increasing oxide film thickness effectively increases ROC. The curvature of the tip subsequently affects the location and orientation of neighboring AgNCs relative to the apex AgNC. We fabricated colloidal nanoantenna probes using 87 ± 5 nm AgNCs and measured their TERS EFs. Figure 3.7.A-D show example SEM images of colloidal nanoantenna fabricated on

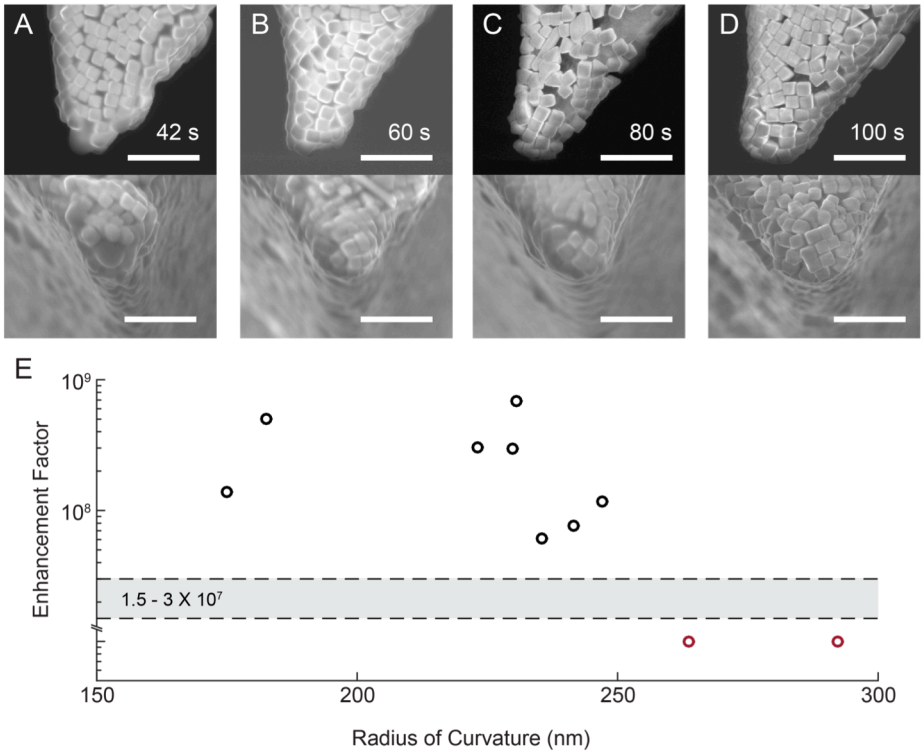

Figure 3.7. Experimental EF dependence on tip radius. (A-D) SEM images showing side views (top images), and top views (bottom images) of colloidal nanoantenna with different SiO_2 growth times: 42 s (A), 60 s (B), 80 s (C), and 100 s (D). (E) Experimental EF dependence on measured colloidal nanoantenna ROC (determined by fitting a circle to the apex of the colloidal nanoantenna). The gray area between two dashed lines represent the experimentally determined detection limit for our instrumentation given the integration time and power used for these experiments. Circles in red represent colloidal nanoantenna displaying AgNCs at the apex but with no measurable TERS signal.

AFM tips with different oxide thickness growth times: 42 s, 60 s, 80 s, and 100 s. Tips with a growth time of 42 s were sharp enough to puncture the AgNC film during fabrication and did not support an apex nanoparticle. We found none of these nanoantenna were TERS active (Figure 3.7.A). Blunter tips with growth times ranging from 60 – 100 s were able to support unbroken AgNC films and all except two (discussed below) provided measurable TERS EFs. We calculated the experimental Raman EF and imaged each nanoantenna by scanning electron microscopy. Using image analysis software, we measured the ROC of the tip (including the AgNC film coating the underlying tip). Nanoantenna that had large breaks or gaps in the film at or near the apex were not considered in this experiment because an ROC could not be accurately determined. Figure 3.7.E plots the relationship between nanoantenna curvature and measured Raman EF. Of interest are the two red circles with ROCs of 264 nm and 292 nm (100 s PECVD growth times). These nanoantenna gave no measurable TERS EF. These are the only examples out of over 40 TERS active nanoantenna fabricated where an AgNC was positioned at the apex but a measurable TERS signal was not obtained. We believe that these nanoantenna were TERS active but that the TERS activity was below the detection threshold of our instrument (which we calculated to be $1.5 – 3 \times 10^7$ at 785 nm for the measurement configuration used in this experiment).

We expect that this decrease below the threshold of detection is due to strong interparticle coupling. To verify this, we simulated 5 AgNC simulations with increasing tip ROC (Figure 3.8.A). Simulations were carried out with 85 nm AgNCs

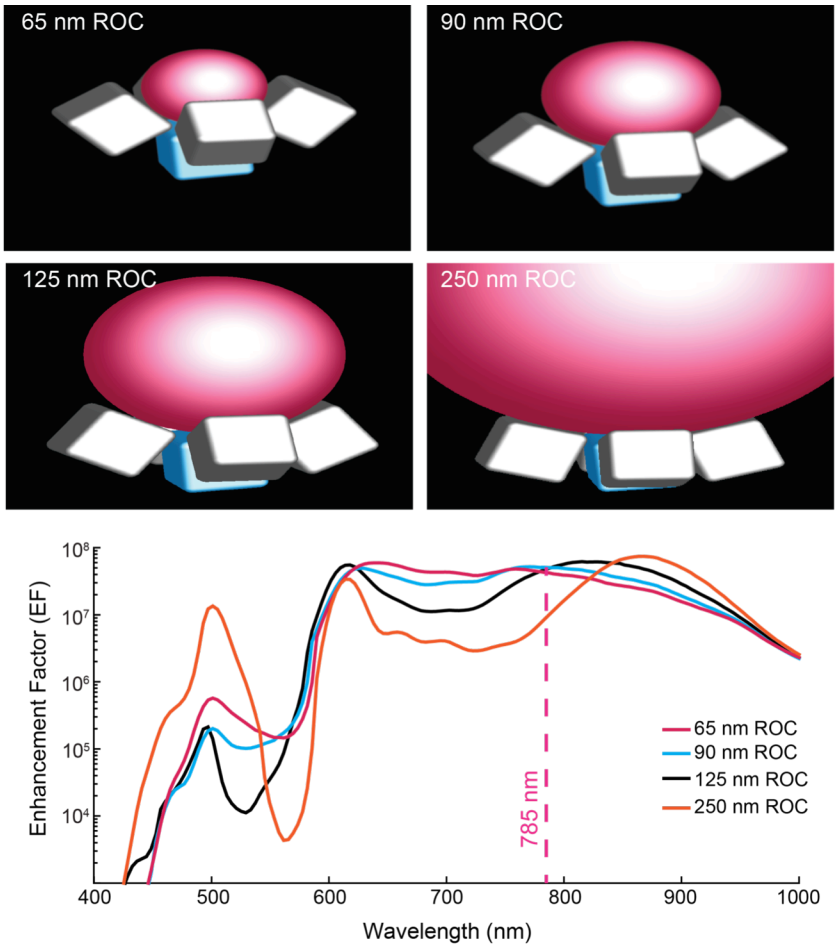

Figure 3.8. EF dependence on ROC FDTD simulations. (A-D) Schematic of AgNC simulations using 85 nm AgNCs. The apex AgNC was placed at θ, ϕ of 5°, 5°. Neighboring AgNCs are placed tangent to a sphere of (A) 65 nm, (B) 90 nm, (C) 125 nm, and (D) 250 nm radius. (D) EFs for the simulations shown in (A-D). The dashed line shows the 785 nm excitation wavelength.

with the apex AgNC oriented at θ=ϕ=5°. Figure 3.8.B shows that increasing the tip ROC from 65 nm to 250 nm redshifts the LAP resulting from interparticle coupling from 758 to 868 nm. This redshift is likely a result of increased interparticle coupling as the orientation angle between AgNCs is decreased. This redshift also decreases the simulated EF at 783 nm from 8.5 x 10^7 to 4.3 x 10^6. We conclude that the inability to measure an EF from the nanoantenna with a large ROC results not from the

disappearance of any plasmon resonance, but from a significant redshift away from our 785 nm excitation source.

3.2.4. AgNC Arrangement

As tip radius increases, so does the likelihood of a double-tip (multiple Raman hotspots resulting from two or more AgNCs generating comparable enhanced electric fields). To investigate the requirements for a double-tip, we simulated a nanoantenna where multiple nanocubes were nearly-equidistant from the substrate. While a simulation of multiple AgNCs perfectly equidistant from a surface would result in multiple hotspots, the purpose of this experiment is to investigate an apex AgNC that is dominant by only a small distance. Figure 3.9. compares the results of our previous 5 AgNC simulation, where the apex AgNC was 28 nm closer to the substrate than the neighboring AgNCs, with a simulation in which four AgNCs are nearly centered around the tip apex (Figure 3.9.A). This is representative of real nanoantenna imaged with SEM, in which an apex AgNC was not obviously visible, implying any apex AgNC would have been closer to the substrate by only several nm. In this nearly-equidistant simulation, AgNCs have small lateral offsets to allow for a 2 nm offset of a single AgNC.

Figure 3.9.B shows the Average Raman EFs for both the centered apex and nearly-equidistant simulations as well as a single AgNC nanoantenna for reference. The centered apex AgNC model has a Raman hotspot radius of 10.9 nm while the nearly-equidistant model has a Raman hotspot radius of 12.8 nm. Thus even the small offset of 2 nm for an apex AgNC is enough to generate a single-tip high-resolution

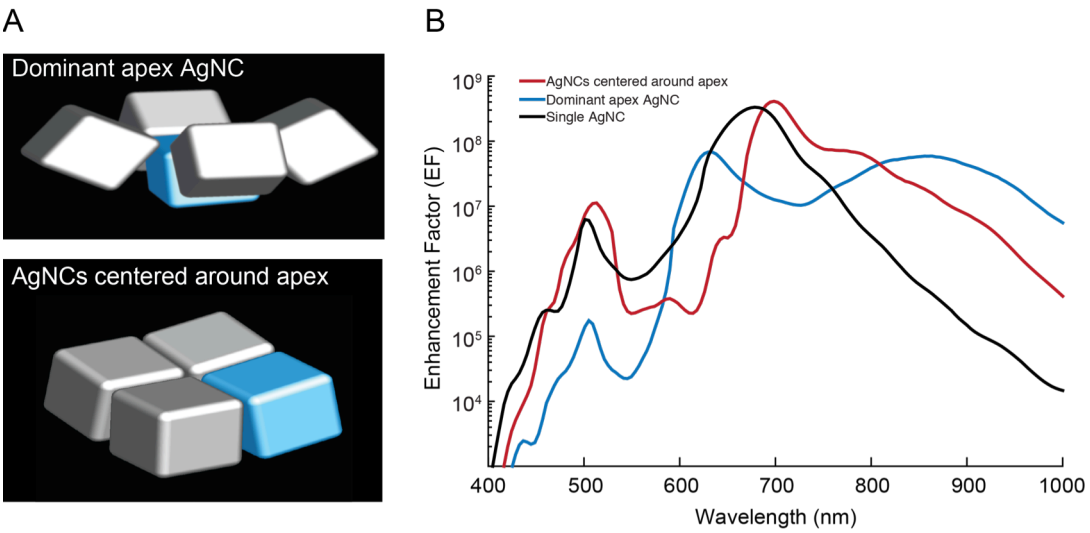

Figure 3.9. EF Dependence on AgNC arrangement at tip apex. (A) Schematics of AgNC simulations with five AgNCs where one nanoparticle has the dominant apex position and a θ, ϕ = 5° (highlithed in blue, top image), and a simulation with four AgNCs centered around the tip apex where a single AgNC is only 2 nm closer to the surface (highlighted in blue, bottom image). (B) EFs for the simulations shown in (A) as well as for a single AgNC with a θ, ϕ of 5°. All AgNC simulations are carried out for 85 nm sized AgNCs.

TERS signal. An important difference is that the resonance peak edge is red-shifted for the nearly-equidistant model, reaching an EF=1 x 10^7 at 666 nm while the centered apex nanoparticle model reaches an EF=1 x 10^7 at 602 nm. This shift is important for considering experimental design; HeNe lasers (633 nm) are a commonly used excitation source for TERS measurements. We observed previously that 785 nm excitation consistently provided higher EFs for colloidal nanoantenna than 633 nm excitation.[35] There were at least two nanoantenna observed that provided measurable TERS with 785 nm excitation and no measurable TERS at 633 nm excitation.

Even with control over the size and ROC of colloidal nanoantenna, the fabrication process still leaves random variation between nanoantenna. An experimental deviation in EF of around an order of magnitude was observed for our nanoantenna despite attempts to keep experimental parameters constant. This is

significantly less deviation than we have previously observed for Au etched wire tips.[35] Simulations predict a deviation of a factor of 5-8 in EF for orientation differences of the apex AgNC. Additional deviation between tips likely results from differences in the location and orientation of neighboring AgNCs, density of the AgNC film, and whether the film has holes or non-cubic nanoparticles. In addition, there is heterogeneity on a small scale between individual nanocubes as well as tip ROC. Each of these variables is expected to lead to small deviations in EF between nanoantenna.

3.3. Experimental and Computational Methods

The Experimental and Computational methods employed here can be found in detail in Chapter 2.

3.4. Conclusions

We have observed through experiment and simulation that a consistent Raman EF is observed across nanoantenna using a variety of AgNC sizes and tip ROCs. This effect results from a hybridized plasmon resonance of coupled AgNCs on the AFM tip that generates a broadband optical response. This broadband resonance is able to reduce the variation in performance across batches of simultaneously fabricated TERS probes, increasing their utility through high levels of reproducibility. The coupling between AgNCs additionally introduces a waveguiding mode that may contribute to the robust and high Raman EFs. The colloidal self-assembly process allows flexibility

to explore near-field optical probes fabricated with other shaped nanocrystals that display sharp features and high levels of interparticle coupling.

Chapter 3, in full, is currently being prepared for submission for publication of the material. **Dill, T. J.**, Tao, A. R. The dissertation author was the principal researcher and author of this material.

3.5. References

1. Higgins, D. A.; Hall, J. E.; Xie, A., Optical Microscopy Studies of Dynamics within Individual Polymer-Dispersed Liquid Crystal Droplets. *Accounts of Chemical Research* **2005,** *38* (2), 137-145.

2. Betzig, E.; Chichester, R. J., Single Molecules Observed by Near-Field Scanning Optical Microscopy. *Science* **1993,** *262* (5138), 1422.

3. Lewis, A.; Taha, H.; Strinkovski, A.; Manevitch, A.; Khatchatouriants, A.; Dekhter, R.; Ammann, E., Near-field optics: from subwavelength illumination to nanometric shadowing. *Nat Biotech* **2003,** *21* (11), 1378-1386.

4. Jiang, N.; Chiang, N.; Madison, L. R.; Pozzi, E. A.; Wasielewski, M. R.; Seideman, T.; Ratner, M. A.; Hersam, M. C.; Schatz, G. C.; Van Duyne, R. P., Nanoscale Chemical Imaging of a Dynamic Molecular Phase Boundary with Ultrahigh Vacuum Tip-Enhanced Raman Spectroscopy. *Nano Letters* **2016,** *16* (6), 3898-3904.

5. Stöckle, R. M.; Suh, Y. D.; Deckert, V.; Zenobi, R., Nanoscale chemical analysis by tip-enhanced Raman spectroscopy. *Chemical Physics Letters* **2000,** *318* (1–3), 131-136.

6. Chen, C.; Hayazawa, N.; Kawata, S., A 1.7 nm resolution chemical analysis of carbon nanotubes by tip-enhanced Raman imaging in the ambient. *Nat Commun* **2014,** *5*.

7. Kumar, N.; Stephanidis, B.; Zenobi, R.; Wain, A. J.; Roy, D., Nanoscale mapping of catalytic activity using tip-enhanced Raman spectroscopy. *Nanoscale* **2015,** *7* (16), 7133-7137.

8. Ryan Beams and Luiz Gustavo Cançado and Ado Jorio and, A. N. V. a. L. N., Tip-enhanced Raman mapping of local strain in graphene. *Nanotechnology* **2015,** *26* (17), 175702.

9. van Schrojenstein Lantman, E. M.; Deckert-Gaudig, T.; Mank, A. J. G.; Deckert, V.; Weckhuysen, B. M., Catalytic processes monitored at the nanoscale with tip-enhanced Raman spectroscopy. *Nat Nano* **2012,** *7* (9), 583-586.

10. Park, K.-D.; Khatib, O.; Kravtsov, V.; Clark, G.; Xu, X.; Raschke, M. B., Hybrid Tip-Enhanced Nanospectroscopy and Nanoimaging of Monolayer WSe2 with Local Strain Control. *Nano Letters* **2016,** *16* (4), 2621-2627.

11. Bao, W.; Melli, M.; Caselli, N.; Riboli, F.; Wiersma, D. S.; Staffaroni, M.; Choo, H.; Ogletree, D. F.; Aloni, S.; Bokor, J.; Cabrini, S.; Intonti, F.; Salmeron, M. B.; Yablonovitch, E.; Schuck, P. J.; Weber-Bargioni, A., Mapping Local Charge Recombination Heterogeneity by Multidimensional Nanospectroscopic Imaging. *Science* **2012,** *338* (6112), 1317-1321.

12. Pollard, B.; Muller, E. A.; Hinrichs, K.; Raschke, M. B., Vibrational nano-spectroscopic imaging correlating structure with intermolecular coupling and dynamics. *Nature Communications* **2014,** *5*, 3587.

13. Muller, E. A.; Pollard, B.; Bechtel, H. A.; van Blerkom, P.; Raschke, M. B., Infrared vibrational nanocrystallography and nanoimaging. *Science Advances* **2016,** *2* (10).

14. Pollard, B.; Raschke, M. B., Correlative infrared nanospectroscopic and nanomechanical imaging of block copolymer microdomains. *Beilstein Journal of Nanotechnology* **2016,** *7*, 605-612.

15. Khatib, O.; Wood, J. D.; McLeod, A. S.; Goldflam, M. D.; Wagner, M.; Damhorst, G. L.; Koepke, J. C.; Doidge, G. P.; Rangarajan, A.; Bashir, R.; Pop, E.; Lyding, J. W.; Thiemens, M. H.; Keilmann, F.; Basov, D. N., Graphene-Based Platform for Infrared Near-Field Nanospectroscopy of Water and Biological Materials in an Aqueous Environment. *ACS Nano* **2015,** *9* (8), 7968-7975.

16. Liao, M.; Jiang, S.; Hu, C.; Zhang, R.; Kuang, Y.; Zhu, J.; Zhang, Y.; Dong, Z., Tip-Enhanced Raman Spectroscopic Imaging of Individual Carbon Nanotubes with Subnanometer Resolution. *Nano Letters* **2016,** *16* (7), 4040-4046.

17. Zhang, R.; Zhang, Y.; Dong, Z. C.; Jiang, S.; Zhang, C.; Chen, L. G.; Zhang, L.; Liao, Y.; Aizpurua, J.; Luo, Y.; Yang, J. L.; Hou, J. G., Chemical mapping of a single molecule by plasmon-enhanced Raman scattering. *Nature* **2013,** *498* (7452), 82-86.

18. Jiang, S.; Zhang, Y.; Zhang, R.; Hu, C.; Liao, M.; Luo, Y.; Yang, J.; Dong, Z.; Hou, J. G., Distinguishing adjacent molecules on a surface using plasmon-enhanced Raman scattering. *Nat Nano* **2015,** *10* (10), 865-869.

19. Deckert-Gaudig, T.; Kurouski, D.; Hedegaard, M. A. B.; Singh, P.; Lednev, I. K.; Deckert, V., Spatially resolved spectroscopic differentiation of hydrophilic and hydrophobic domains on individual insulin amyloid fibrils. *Scientific Reports* **2016,** *6*, 33575.

20. Su, W.; Kumar, N.; Dai, N.; Roy, D., Nanoscale mapping of intrinsic defects in single-layer graphene using tip-enhanced Raman spectroscopy. *Chemical Communications* **2016,** *52* (53), 8227-8230.

21. Su, W.; Roy, D., Visualizing graphene edges using tip-enhanced Raman spectroscopy. *Journal of Vacuum Science & Technology B* **2013,** *31* (4), 041808.

22. Hermann, P.; Hecker, M.; Chumakov, D.; Weisheit, M.; Rinderknecht, J.; Shelaev, A.; Dorozhkin, P.; Eng, L. M., Imaging and strain analysis of nano-scale SiGe structures by tip-enhanced Raman spectroscopy. *Ultramicroscopy* **2011,** *111* (11), 1630-1635.

23. Rusciano, G.; Zito, G.; Isticato, R.; Sirec, T.; Ricca, E.; Bailo, E.; Sasso, A., Nanoscale Chemical Imaging of Bacillus subtilis Spores by Combining Tip-Enhanced Raman Scattering and Advanced Statistical Tools. *ACS Nano* **2014,** *8* (12), 12300-12309.

24. Schmid, T.; Yeo, B.-S.; Leong, G.; Stadler, J.; Zenobi, R., Performing tip-enhanced Raman spectroscopy in liquids. *Journal of Raman Spectroscopy* **2009,** *40* (10), 1392-1399.

25. Paulite, M.; Blum, C.; Schmid, T.; Opilik, L.; Eyer, K.; Walker, G. C.; Zenobi, R., Full Spectroscopic Tip-Enhanced Raman Imaging of Single Nanotapes

Formed from β-Amyloid(1–40) Peptide Fragments. *ACS Nano* **2013,** *7* (2), 911-920.

26. Pozzi, E. A.; Sonntag, M. D.; Jiang, N.; Klingsporn, J. M.; Hersam, M. C.; Van Duyne, R. P., Tip-Enhanced Raman Imaging: An Emergent Tool for Probing Biology at the Nanoscale. *ACS Nano* **2013,** *7* (2), 885-888.

27. Zhang, W.; Cui; Yeo, B.-S.; Schmid, T.; Hafner, C.; Zenobi, R., Nanoscale Roughness on Metal Surfaces Can Increase Tip-Enhanced Raman Scattering by an Order of Magnitude. *Nano Letters* **2007,** *7* (5), 1401-1405.

28. Stadler, J.; Oswald, B.; Schmid, T.; Zenobi, R., Characterizing unusual metal substrates for gap-mode tip-enhanced Raman spectroscopy. *Journal of Raman Spectroscopy* **2013,** *44* (2), 227-233.

29. Neacsu, C. C.; Steudle, G. A.; Raschke, M. B., Plasmonic light scattering from nanoscopic metal tips. *Applied Physics B* **2005,** *80* (3), 295-300.

30. Yasuhiko Fujita and Peter Walke and Steven De Feyter and Hiroshi, U.-i., Tip-enhanced Raman scattering microscopy: Recent advance in tip production. *Japanese Journal of Applied Physics* **2016,** *55* (8S1), 08NA02.

31. Mino, T.; Saito, Y.; Verma, P., Quantitative Analysis of Polarization-Controlled Tip-Enhanced Raman Imaging through the Evaluation of the Tip Dipole. *ACS Nano* **2014,** *8* (10), 10187-10195.

32. Taguchi, A.; Yu, J.; Verma, P.; Kawata, S., Optical antennas with multiple plasmonic nanoparticles for tip-enhanced Raman microscopy. *Nanoscale* **2015,** *7* (41), 17424-17433.

33. Mino, T.; Saito, Y.; Verma, P., Control of near-field polarizations for nanoscale molecular orientational imaging. *Applied Physics Letters* **2016,** *109* (4), 041105.

34. Yang, Y.; Li, Z.-Y.; Nogami, M.; Tanemura, M.; Huang, Z., The controlled fabrication of "Tip-On-Tip" TERS probes. *RSC Advances* **2014,** *4* (9), 4718-4722.

35. Dill, T. J.; Rozin, M. J.; Palani, S.; Tao, A. R., Colloidal Nanoantennas for Hyperspectral Chemical Mapping. *ACS Nano* **2016,** *10* (8), 7523-7531.

36. Neacsu, C. C.; Dreyer, J.; Behr, N.; Raschke, M. B., Scanning-probe Raman spectroscopy with single-molecule sensitivity. *Physical Review B* **2006,** *73* (19), 193406.

37. Bao, W.; Staffaroni, M.; Bokor, J.; Salmeron, M. B.; Yablonovitch, E.; Cabrini, S.; Weber-Bargioni, A.; Schuck, P. J., Plasmonic near-field probes: a comparison of the campanile geometry with other sharp tips. *Optics Express* **2013,** *21* (7), 8166-8176.

38. Neacsu, C. C.; Berweger, S.; Olmon, R. L.; Saraf, L. V.; Ropers, C.; Raschke, M. B., Near-Field Localization in Plasmonic Superfocusing: A Nanoemitter on a Tip. *Nano Letters* **2010,** *10* (2), 592-596.

39. Lassiter, J. B.; McGuire, F.; Mock, J. J.; Ciracì, C.; Hill, R. T.; Wiley, B. J.; Chilkoti, A.; Smith, D. R., Plasmonic Waveguide Modes of Film-Coupled Metallic Nanocubes. *Nano Letters* **2013,** *13* (12), 5866-5872.

40. Rozin, M. J.; Rosen, D. A.; Dill, T. J.; Tao, A. R., Colloidal metasurfaces displaying near-ideal and tunable light absorbance in the infrared. *Nat Commun* **2015,** *6*.

41. Maier, S. A.; Kik, P. G.; Atwater, H. A.; Meltzer, S.; Harel, E.; Koel, B. E.; Requicha, A. A. G., Local detection of electromagnetic energy transport below the diffraction limit in metal nanoparticle plasmon waveguides. *Nat Mater* **2003,** *2* (4), 229-232.

42. Kawata, S.; Ono, A.; Verma, P., Subwavelength colour imaging with a metallic nanolens. *Nat Photon* **2008,** *2* (7), 438-442.

43. Höppener, C.; Lapin, Z. J.; Bharadwaj, P.; Novotny, L., Self-Similar Gold-Nanoparticle Antennas for a Cascaded Enhancement of the Optical Field. *Physical Review Letters* **2012,** *109* (1), 017402.

44. Maier, S. A.; Kik, P. G.; Atwater, H. A., Optical pulse propagation in metal nanoparticle chain waveguides. *Physical Review B* **2003,** *67* (20), 205402.

45. Moreau, A.; Ciraci, C.; Mock, J. J.; Hill, R. T.; Wang, Q.; Wiley, B. J.; Chilkoti, A.; Smith, D. R., Controlled-reflectance surfaces with film-coupled colloidal nanoantennas. *Nature* **2012,** *492* (7427), 86-89.

46. Esteban, R.; Aguirregabiria, G.; Borisov, A. G.; Wang, Y. M.; Nordlander, P.; Bryant, G. W.; Aizpurua, J., The Morphology of Narrow Gaps Modifies the Plasmonic Response. *ACS Photonics* **2015,** *2* (2), 295-305.

47. Rose, A.; Hoang, T. B.; McGuire, F.; Mock, J. J.; Ciracì, C.; Smith, D. R.; Mikkelsen, M. H., Control of Radiative Processes Using Tunable Plasmonic Nanopatch Antennas. *Nano Letters* **2014,** *14* (8), 4797-4802.

48. Gao, B.; Arya, G.; Tao, A. R., Self-orienting nanocubes for the assembly of plasmonic nanojunctions. *Nat Nano* **2012,** *7* (7), 433-437.

Chapter 4

Self-Assembled Ag Nanocubes for Metasurface-Enhanced Raman Spectroscopy

4.1. Introduction

In chapter 4 we introduce metasurface-enhanced Raman spectroscopy (mSERS), a sensing platform based on Ag nanocubes (AgNC) deposited by the Langmuir-Blodgett (LB) method onto a metal substrate. The AgNC-on-metal structure has been previously demonstrated to efficiently focus visible and near-infrared light into the parallel gap formed between the nanocube face and the underlying thin-film.[1] The gap region layers allows a plasmon that propagates in the plane of the metal. At the AgNC edge the light undergoes reflection, resulting in a Fabry-Perot like resonance and strong electric field-confinement within the gap.[1-4] The resonance can be tuned by varying either the AgNC size or the gap height. When a Raman analyte is introduced into the gap, the mSERS substrate generates strongly enhanced Raman signals from a diffraction-limited spot. mSERS substrates can be fabricated at wafer-scale with high AgNC deposition uniformity. The uniformity of the self-assembly process allows the mSERS substrate to generate spatial Raman maps with uniform Raman EF over large areas. Here we demonstrate Raman maps of patterned molecular monolayers over regions > 100 μm^2.

In order to maximize the collected Raman signal, we are also interested in studying the properties of the LSPR of the mSERS substrate. Here we look at AgNC interparticle coupling as well as the polarization of the gap-plasmon near-field. When AgNCs become close enough to each other, the LSPR between AgNCs becomes coupled and has an effect on the resonance.[5] We find that below a AgNC surface density of 30% the Raman EF is maximized because AgNCs are non-interacting. In

this regime, any additional AgNCs contribute linearly to the signal. At higher surface density, the LSPR results in a weaker plasmon gap-mode and the Raman EF decreases significantly. We additionally find that molecules with polarizabilites oriented orthogonally to the surface will generate higher Raman EFs than materials that lie with their polarizability in-plane. This is a result of the gap-plasmon being oriented predominantly out-of-plane of the gap. The polarization of incident light (near-field) in Raman spectroscopy has been shown to be critically important for 2D materials such as graphene.[6-9]

In chapter 3, we demonstrated the detection limit for colloidal nanoantenna (for our experimental system at 785 nm excitation) to be an EF of $1.5 – 3 \times 10^7$. Because colloidal nanoantenna and mSERS substrates have similar LSPR resonances, they can be expected to return similar results for a given Raman analyte. mSERS substrates offer an advantage in that the number of active hotspots is several hundred AgNCs versus only one for a colloidal nanoantenna. More active hotspots results in a higher total collected Raman signal without modifing the EF or the optics of the experimental system. This higher Raman signal can be used to study systems that are below the detection threshold of the colloidal nanoantenna. The mSERS data is useful for determining a minimum EF for TERS detection, and subsequent experimental design.

We also introduce a modified fabrication process, in which AgNCs are first deposited onto a polydimethylsiloxane (PDMS) substrate, which can then be inverted and adhered to a functionalized metal surface. If the metal surface has regions of

varying surface energy, traditional LB deposition can result in uneven deposition due to drying effects. This modified fabrication gives uniform AgNC deposition as the PDMS is highly uniform. This fabrication method also allows high-levels of control over the ligand within the gap which can control chemical interactions as well as physical dimensions (discussed in detail in chapter 6).

4.2. Results and Discussion

4.2.1. mSERS Fabrication and Characterization

Figure 4.1. shows an overview of the functionality of mSERS substrates. Figure 4.1.A shows a schematic representation of an AgNC separated from an Au thin-film (50 nm) by one or more passive or functional organic spacer layers. Incident light is focused into the gap, increasing the electric field strength within the nanojunction (area within white dashed line) to 1.05 X 10^2 times that of the incident field. Raman enhancements are generated wherever the electric near-field is enhanced, in the case of mSERS substrates this is a large fraction of the cross-sectional area. The mSERS substrate is unlike other SERS substrates where small hotspots are responsible for the majority of SERS signals.[10-13] A Raman analyte is positioned directly in the nanoscale junction, the inset shows the ligand(s) within the gap. Figure 4.1. shows the case of a pattern of self-assembled monolayers (SAM) of thiophenol (PhSH, green) and 1-hexadecanethiol (HDT, red). The layer of polyvinylpyrillidone (PVP) on the AgNC surface remains from AgNC synthesis. The overall gap height is estimated to be 2-3 nm. We fabricated mSERS substrates using the Langmuir-Blodgett (LB) deposition (see methods). A uniform layer of well-spaced AgNCs is transferred onto a

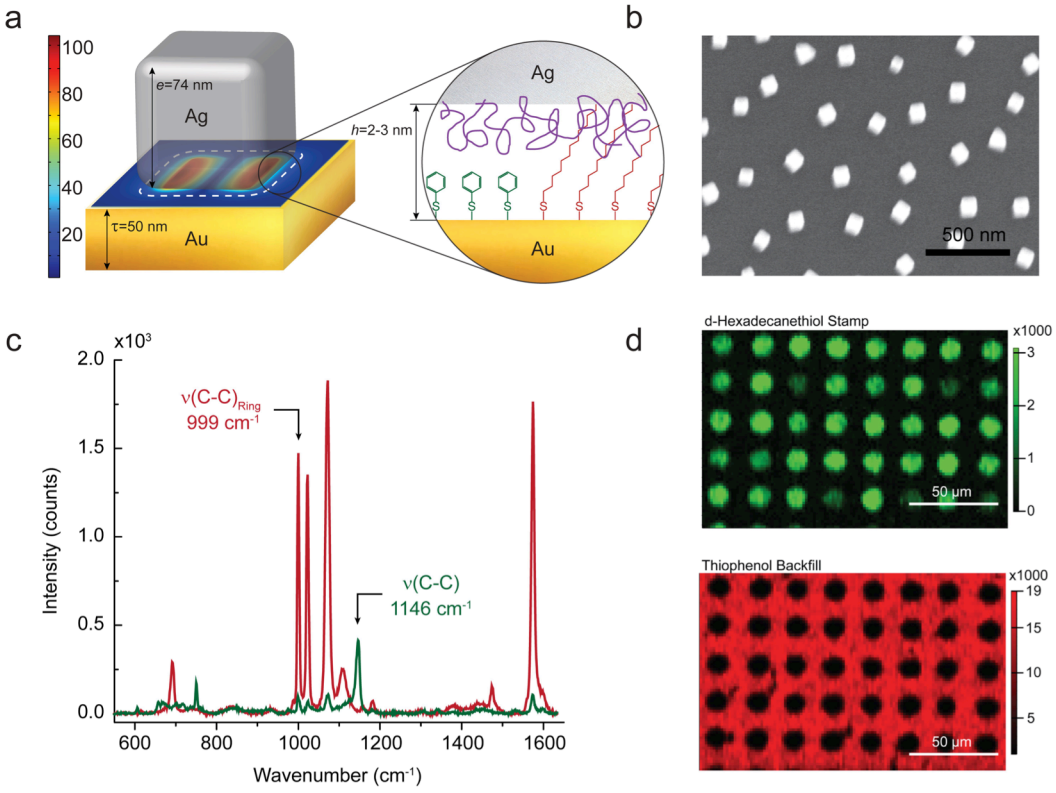

Figure 4.1. Overview of mSERS substrate structure and performance. (A) Schematic showing an individual metasurface unit, an AgNC on an Au thin-film separated by a thin dielectric spacer. In the case of an mSERS substrate the dielectric spacer is the Raman analyte of interest, located in the plasmon mode volume, the TCP mode is shown bounded by the white dashed line. Inset shows a hypothetical boundary between Raman analytes in a multi-component analyte system. (B) SEM image of an mSERS substrate. (C) mSERS spectra from different regions on an Au thin-film patterned with two different thiolated molecular monolayers (Red – PhSH, Green – dHDT). D) mSERS maps of a an Au thin-film which was patterned by two different molecules, shown in (C). Each map represents different spectral components of the same physical area. The upper map plots the spatial intensity of the dHDT vibrational mode located at 1146 cm^{-1}, while the lower map is a spatial intensity plot of the PhSH vibrational mode located at 999 cm^{-1}.

substrate already treated with one or more types of Raman analyte molecules. Figure 4.1.B shows a scanning electron microscope (SEM) image of a mSERS surface. The AgNCs used here have an average size of 74 ± 3 nm, and have an average interparticle spacing of 210 ± 80 nm. The AgNC size is chosen for its resonance located near that

of a 785 nm excitation laser,[13] the interparticle spacing insures no plasmon coupling between AgNCs (discussed further below).

To demonstrate both large-scale chemical mapping as well as uniform Raman enhancement over large areas, we patterned an Au thin-film with two chemically unique SAMs. A PDMS stamp was used to print a deuterated-HDT (dHDT) SAM into the circles. PhSH was then backfilled into the unstamped Au region. Finally, a layer of AgNCs was deposited to make the mSERS substrate. All subsequent spectra were collected with the resonant excitation wavelength of 785 nm unless noted otherwise. Figure 4.1C displays representative SERS spectra from each region of the patterned substrate, the red spectra shows mSERS spectra of PhSH, the green spectra shows mSERS spectra of dHDT. We collected spectra over a 100 x 150 μm region, Figure 4.1.D. Each diffraction-limited point on the map contains the chemical signature of the underlying molecular pattern. Here we plot the intensities of two vibrational modes distinctly representing PhSH and dHDT. These vibrational modes are highlighted in Figure 4.1.C with the 999cm^{-1} and 1146 cm^{-1} vibrational modes corresponding to the aromatic ring stretch and the aliphatic C-C backbone stretch respectively.[14, 15]

The mSERS fabrication process gives control over both AgNC size and average interparticle spacing, we expect both to have significant effects on Raman enhancement factor (EF). While simulations suggest that 74 nm AgNC with a 17 nm corner radius is resonant at 785 nm, it was experimentally shown mSERS substrates with AgNCs in the size range of 70-91 nm showed little variation in measured Raman enhancement factor (EF), the amount an analyte molecule has its Raman signal

enhanced by the electric near-field.[13] This study concluded that only AgNCs larger than 91 nm showed a decrease in EF, and by much less than predicted by simulation. It is hypothesized that AgNC polydispersity plays a large role in maintaining a uniform EF over a large AgNC size range. The polydispersity effect on Raman EF is discussed in detail in Chapter 5. AgNC surface density however, plays a large role in Raman EF due to interparticle plasmon coupling. The surface density of AgNCs is controlled by monitoring surface pressure of the LB film. It was previously shown *via* UV-Vis spectroscopy that AgNC surface densities below 17%, interparticle spacings of >190 nm, showed negligible interparticle coupling[1]. For AgNC films nearing a close-packed nature, interparticle spacing of < 50 nm, interparticle plasmon coupling became dominant and altered the resonance structure.[5] As the AgNCs progress from well-spaced to close-packed, a delocalized plasmon resonance forms, red-shifting the TCP into the IR. Here we probe the Raman EF and indirectly, the near-field strength, resulting from different surface densities of AgNC mSERS substrates.

4.2.2. The Effects of AgNC Surface Density on EF

We functionalized Au thin-films with PhSH and deposited 91 ± 4 nm AgNCs with surface densities estimated by image analysis software at: 6.2%, 16.2%, 17%, 27.1%, 32%, 43.1%, and 65%. Figure 4.2.A shows spatially averaged mSERS spectra for mSERS substrates with varying surface density. Figure 4.2.B shows the average intensity of the ν(Ring), 1024 cm^{-1}, vibrational mode plotted for each mSERS substrate. From 6.2 – 32% the Raman intensity increases from 1950 – 9492 counts linearly with surface density ($R^2 = 0.96$). This indicates negligible interparticle

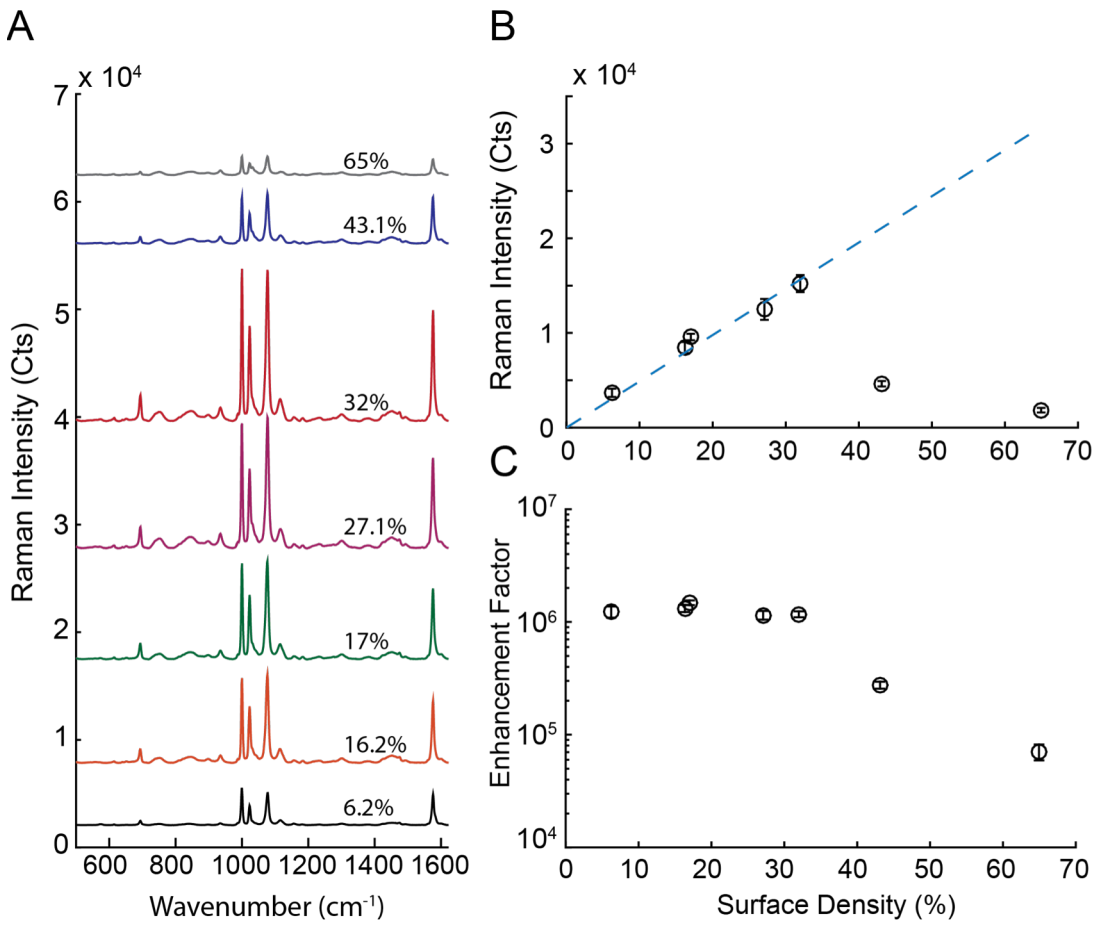

Figure 4.2. Effects of AgNC surface density on Raman EF. (A) Average Raman spectra for mSERS substrates of varying AgNC surface density. (B) Raman intensity of the 1024 cm^{-1} vibrational mode of PhSH as a function of AgNC surface density. The dashed line shows a linear fit of the five lowest surface density substrates. (C) EF shown as a function of AgNC surface density.

plasmon coupling. Each added AgNC provides an additional hotspot with the same intensity and linearly contributes to the total collected Raman signal. At 43.1% AgNC surface density there is a sharp decrease in Raman intensity (3015 counts), SEM imaging shows this substrate primarily consisting of small aggregates (average cluster size is 1.9 AgNCs). As neighboring AgNCs become electromagnetically coupled, the resonance red-shifts away from the 785 nm excitation, decreasing observed Raman scattering. At 65% surface density, the average cluster size increases to 56 AgNCs,

further increasing electromagnetic coupling and decreasing the Raman intensity (1150 counts). Figure 4.2.C shows the Raman EF for each substrate (see methods for detailed calculations). Raman EF accounts for surface density and thus returns a constant EF for non-coupled mSERS surfaces from 6.2 – 32%. As increased electromagnetic coupling decreases the near-field strength at 785 nm however, we observe a decrease in the Raman EF. An mSERS substrate that provides an optimal Raman EF (at 785 nm excitation) will be fabricated with a surface density at the top of the linear regime (~30%) with AgNCs in the 70-91 nm size range.

4.2.3. Effect of Near-Field Polarization on EF

The observed Raman EF depends highly on the polarizability of a molecule relative to the polarization of the electric field it experiences. The intensity of Raman scattering from a vibrational mode is highly dependent on its polarizability tensor.[16] Because enhanced-Raman scattering is dependent on the fourth power of field enhancement, we expect to find larger Raman intensities for molecules when the polarizability tensor is aligned to the polarization of the exciting light. Figure 4.3.A,B shows simulated field enhacnement profiles of the out-of-plane and in-plane components of the plasmon resonance (1000 nm, 96 nm AgNC). The component of the field enhancement perpendicular to the substrate (out-of-plane) has an average field enhancement of 64 while the orthogonal component (in-plane) has an average field enhancement of 6. Figure 4.3.C shows the calculated Raman EFs from 400 – 1000 nm. At 785 nm, the out-of-plane component is 5 orders of magnitude stronger

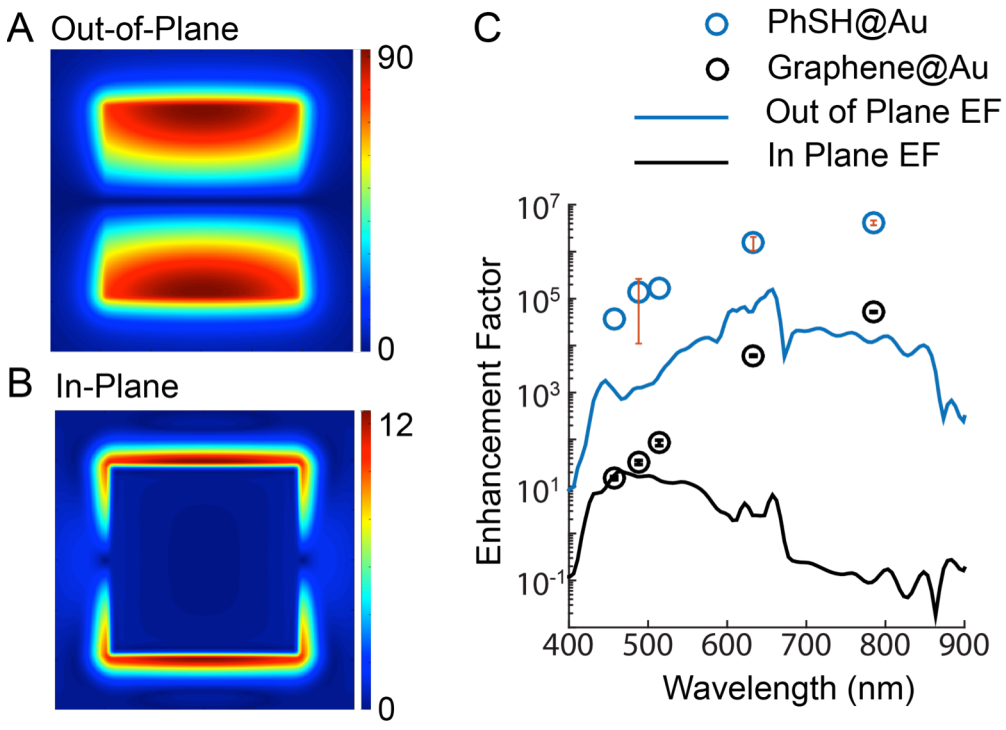

Figure 4.3. Near-field polarization effects on Raman EF. Computer simulation of an mSERS substrate showing the (A) out-of-plane, and (B) in-plane polarized near-field profiles in the dielectric gap. (C) Wavelength dependent EF for simulated in-plane and out-of plane near-fields (black and blue lines respectively), and for graphene and a PhSH SAM as Raman analytes within mSERS gaps (black and blue circles respectively). Error bars were omitted from 457 and 488 nm excitation for PhSH substrates as the errors were larger than the data values and this cannot be accurately displayed in a logarithmic plot.

than the in-plane component. This suggests that the Raman analyte must be oriented favorably to achieve high Raman EFs.

We are able to indirectly probe in-plane and out-of-plane field enhancements *via* mSERS measurements. Aromatic ring structures are known to be polarizable predominantly in the plane of the ring. PhSH SAMs and graphene have rings oriented orthogonally to each other on a flat surface. These molecules can be used to probe the polarization of the field enhancement.[6, 17]. Figure 4.3.C shows the wavelength dependent Raman EFs for both PhSH and graphene on a mSERS substrates. At the maximum EF, 785 nm, the EF of PhSH is 4.1 ± .48 x 10^6, while the EF of graphene is

$5.2 \pm .1 \times 10^4$, roughly 2 orders of magnitude smaller. Graphene shows similarly smaller EFs for other wavelengths: 633, 514, 488, and 457 nm. The EF difference predicted by simulation between in-plane and out-of-plane polarization is 3 orders of magnitude larger than the experimentally observed EF difference. A possible explanation is that the Au surface is not perfectly flat. This nanoscale roughness may result in a graphene layer that has components out-of-plane, which would interact with the out-of-plane field enhancement and increase the EF significantly. It is also known that Raman scattering from graphene is not localized, the Raman vibrational modes are based on phonon scattering.[18-20] It is possible that this could lead to inflated EFs where Raman scattering originates in regions other than the AgNC hotspot.

4.2.4. mSERS Substrates Fabricated on PDMS for Increased Uniformity

Direct deposition of AgNCs onto a substrate can lead to regions of varying AgNC density in some cases. This affects the uniformity of the EF. If the substrate has regions of analytes displaying different physical properties such as surface energy then drying effects can cause AgNCs to deposit to one region preferentially. To eliminate this effect, we introduce a modified fabrication process (Figure 4.4.), in which AgNCs are deposited onto a thin layer of PDMS (150 μm). The highly uniform PDMS insures a uniform dispersion of AgNCs (Figure 4.4.A). These substrates are termed mSERS stamps. mSERS stamps can be placed in contact with an arbitrary substrate containing a Raman analyte, and be scanned as previously. Figure 4.4.B shows a schematic of a mSERS stamp adhered to an Au thin-film. Figure 4.4.C shows a photograph as well as

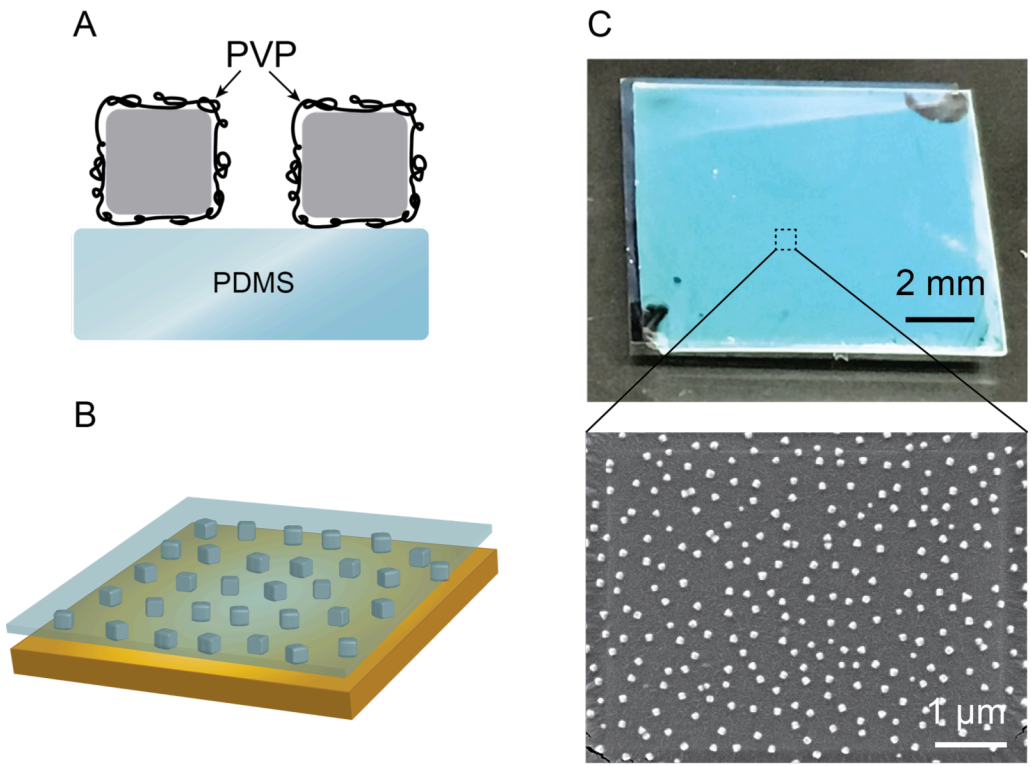

Figure 4.4. Fabrication of a PDMS supported mSERS substrate. (A) AgNCs deposited onto a PDMS surface *via* Langmuir-Blodgett deposition. (B) Schematic showing the AgNC film on PDMS being inverted and brought into contact with the Au substrate (C) A photograph (top) and SEM (bottom) of a film of AgNCs deposited onto 1 cm^2 of PDMS.

an SEM image of a mSERS stamp showing large scale uniformity. Importantly, the PDMS contributes negligibly to our SERS spectra. Additionally, mSERS stamps allow the PVP adsorbed to the AgNC to be exchanged with other ligands prior to bringing the AgNC surface into contact with the substrate. When AgNCs are deposited directly onto the Raman analyte, the PVP capping layer is trapped. Ligands with well characterized lengths, functional groups, and known Raman spectra can be used to further enhance the sensitivity and specificity. This is discussed in detail in chapter 6.

4.3. Experimental and Computational Methods

Ag nanocube preparation: Ag Nanocubes were synthesized via a polyol method published elsewhere.[21] In brief, $AgNO_3$ is reduced in a solution of pentanediol, $CuCl_2$, and polyvinylpyrrolidone (PVP) (M_w=55,000). PVP serves as a selective capping agent that controls nanocube nucleation and growth. The reaction was allowed to proceed until the resulting colloidal dispersion turned an opaque yellow-green color. To remove excess reactants, the nanocube dispersion product was centrifuged (2700 rpm for 10 min) using a Thermo Scientific CL2 Centrifuge, and the resulting precipitate was redispersed and diluted in an ethanol and water mixture, and then vacuum-filtered (Millipore Durapore membranes, with 0.65 μm, 0.45 μm, then 0.22 μm pore sizes) to remove any larger, unwanted particles.

Substrate preparation**:** Si was sonicated in EtOH and cleaned for 60s under a 100W RF Ar plasma in a high vacuum sputter chamber (Denton Discovery 18 Sputter System). 5-10 nm of Ti followed by 50 nm of Au was then sputtered.

SAM functionalized Au substrates were fabricated by incubating the metal thin-film substrates in a 100 μM (PhSH) or 1 mM (HDT, dHDT) ethanolic solution for 60 min, rinsed thouroughly with EtOH and dried under N_2. Functionalized Au substrates either immediately had AgNCs films deposited or were stored under vacuum until ready for use.

Patterned SAMs were fabricated using standard photolithography and μ-contact printing. We fabricated an SU-8 mold with a pattern of of circles (10 μm diameter) arranged in a square lattice (20 μm pitch), and a 5 μm relief height. After silanization the master, PDMS was cured into it overnight at 60° C. The PDMS stamp

was then inked with a 10 mM ethanolic solution of the analyte for 60 s and dried with N_2. Full contact between the stamp and the Ag thin-film was ensured, but no further pressure was applied. The stamp remained in contact for 10 – 15 s. The remaining unstamped Au area was then backfilled by immersing the surface with a 50 μL droplet of 10 mM ethanolic solution of a second analyte for 10 s. The patterned Au substrate was then rinsed with copious amounts of ethanol and dried with N_2.

Nanocube deposition and mSERS Stamps To prepare the AgNCs for Langmuir-Blodgett deposition, a AgNC dispersion is washed by centrifugation and the precipitate is dispersed in EtOH. This process was repeated three times before finally dispersing the precipitate in chloroform. AgNC films were fabricated using a KSV Nima KN2001 Langmuir-Blodgett trough, as previously described.[22] The AgNC solution was deposited drop-wise onto a deionized water (18 MΩ) subphase. The film formed at the air-water interface was allowed to equilibrate for 30. The Ag nanocube film was isothermally compressed to a desired surface density before being transferred to the substrate *via* mechanical dipping. For mSERS stamps, the AgNC film was transferred to a 150 μm thick PDMS film backed by Si.

SERS measurements: All Raman spectra were obtained using a Renishaw inVia confocal Raman microscope. Measurements were taken at powers < 1 mW to prevent laser induced damage. 785 nm illumination was provided by a Renishaw 300 mW diode laser. 633 nm illumination was provided by a Renishaw 17mW HeNe laser. 514, 488, and 457 nm illumination was provided by a Modu-Laser 50 mW Ar+ Ion laser. Spectra were collected through a 50x, 0.9 NA objective. For each EF calculation

an average of 100 data points was taken over a SERS substrate, the standard deviation in these points were used as the error for the EF calculations.

EF Calculations: For each EF calculation, 100 spectra were collected from random locations on an mSERS substrate and averaged. All Raman EFs were calculated using the PhSH vibrational mode of 1024 cm^{-1}, corresponding to the ring breathing mode, which is independent of molecular orientation.[16]. Raman EFs were then calculated using the following equation:[23]

$$EF = \left(\frac{I_{SERS}}{I_{Raman}}\right)\left(\frac{N_{Raman}}{N_{SERS}}\right) \qquad (4.1)$$

Where I_{SERS} and I_{Raman} are the Raman intensities for the mSERS substrates and bulk PhSH respectively. N_{SERS} and N_{Raman} are the number of Raman molecules from which the signal originates and are calculated using the density of neat PhSH and literature packing values for a SAM of PhSH on an Au surface.[24] Laser spot sizes were measured by scanning step-wise over a cleaved Si edge. N_{SERS} is normalized to the surface density of AgNCs on the substrate. Error in EF was determined from the standard deviation in the measured I_{SERS} values; error for I_{Raman} was considered negligible.

FDTD Simulations and Simulated EF: Electromagnetic modeling was performed with Lumerical FDTD Solutions. AgNCs (Palik dielectric data) were modeled in 3 dimensions with an underlying 50 nm Au thin-film. A 3 nm dielectric layer with n = 1.4 was added to reflect the analyte layer positioned within the plasmon volume. Incident light was injected normal to the substrate, and polarized parallel to the (100) faces of the AgNC. A 1 nm global mesh was used; to improve accuracy, the mesh size

was reduced in the gap region to 0.5 nm. The electric field profiles were calculated in the plane of the Au thin film, 1 nm offset from the surface. An average EF for the mSERS substrate is calculated by summing $|E/E_o|^4$ at each pixel (1x1 nm) and normalizing to the cross-sectional area of each nanocube. This calculation was carried out at discrete wavelengths over the the visible range.

4.4. Conclusions

mSERS substrates use Ag nanocubes coupled to an underlying metal film to support a strong gap-plasmon, providing large field-enhancedments and a uniform Raman EF. These mSERS substrates can be fabricated in a scalable fashion over large areas and on many types of surfaces. We show through experiment that mSERS substrates are able to generate Raman maps over large areas with the ability to easily identify unique chemical components. By exploring the limitations of mSERS substrates pertaining to Ag nanocube surface density and analyte orientation, we can better understand the fundamental interactions between these plasmonic junctions and molecular analytes. The large number of Ag nanocubes in an mSERS substrate produces many hotspots and larger Raman scattering signals, allowing us to investigate systems with signals too weak to be detected by TERS. This improved understanding of the optical resonance and its interaction with Raman analytes can help engineer mSERS substrates and TERS probes that will produce higher Raman signals and allow the study of new materials and analytes. Chapters 5 and 6 will

further investigate the mSERS substrate and the effects of Ag nanocube polydispersity and gap-height.

Chapter 4, in full, is currently being prepared for submission for publication of the material. **Dill, T. J.**, Rozin, M. J., Rodarte, A. L., Brown, E. R., Palani, S., Tao, A. R. The dissertation author was the principal researcher and author of this material.

4.5. References

1. Moreau, A.; Ciraci, C.; Mock, J. J.; Hill, R. T.; Wang, Q.; Wiley, B. J.; Chilkoti, A.; Smith, D. R., Controlled-reflectance surfaces with film-coupled colloidal nanoantennas. *Nature* **2012,** *492* (7427), 86-89.

2. Rose, A.; Hoang, T. B.; McGuire, F.; Mock, J. J.; Ciracì, C.; Smith, D. R.; Mikkelsen, M. H., Control of Radiative Processes Using Tunable Plasmonic Nanopatch Antennas. *Nano Letters* **2014,** *14* (8), 4797-4802.

3. Lassiter, J. B.; McGuire, F.; Mock, J. J.; Ciracì, C.; Hill, R. T.; Wiley, B. J.; Chilkoti, A.; Smith, D. R., Plasmonic Waveguide Modes of Film-Coupled Metallic Nanocubes. *Nano Letters* **2013,** *13* (12), 5866-5872.

4. Akselrod, G. M.; Argyropoulos, C.; Hoang, T. B.; Ciracì, C.; Fang, C.; Huang, J.; Smith, D. R.; Mikkelsen, M. H., Probing the mechanisms of large Purcell enhancement in plasmonic nanoantennas. *Nat Photon* **2014,** *8* (11), 835-840.

5. Rozin, M. J.; Rosen, D. A.; Dill, T. J.; Tao, A. R., Colloidal metasurfaces displaying near-ideal and tunable light absorbance in the infrared. *Nat Commun* **2015,** *6*.

6. Heo, G.; Kim, Y. S.; Chun, S.-H.; Seong, M.-J., Polarized Raman spectroscopy with differing angles of laser incidence on single-layer graphene. *Nanoscale Research Letters* **2015,** *10* (1), 45.

7. Su, W.; Roy, D., Visualizing graphene edges using tip-enhanced Raman spectroscopy. *Journal of Vacuum Science & Technology B* **2013,** *31* (4), 041808.

8. Bao, W.; Melli, M.; Caselli, N.; Riboli, F.; Wiersma, D. S.; Staffaroni, M.; Choo, H.; Ogletree, D. F.; Aloni, S.; Bokor, J.; Cabrini, S.; Intonti, F.; Salmeron, M. B.; Yablonovitch, E.; Schuck, P. J.; Weber-Bargioni, A., Mapping Local Charge Recombination Heterogeneity by Multidimensional Nanospectroscopic Imaging. *Science* **2012,** *338* (6112), 1317-1321.

9. Bao, W.; Borys, N. J.; Ko, C.; Suh, J.; Fan, W.; Thron, A.; Zhang, Y.; Buyanin, A.; Zhang, J.; Cabrini, S.; Ashby, P. D.; Weber-Bargioni, A.; Tongay, S.; Aloni, S.; Ogletree, D. F.; Wu, J.; Salmeron, M. B.; Schuck, P. J., Visualizing nanoscale excitonic relaxation properties of disordered edges and grain boundaries in monolayer molybdenum disulfide. *Nat Commun* **2015,** *6*.

10. Fang, Y.; Seong, N.-H.; Dlott, D. D., Measurement of the Distribution of Site Enhancements in Surface-Enhanced Raman Scattering. *Science* **2008,** *321* (5887), 388-392.

11. Kleinman, S. L.; Sharma, B.; Blaber, M. G.; Henry, A.-I.; Valley, N.; Freeman, R. G.; Natan, M. J.; Schatz, G. C.; Van Duyne, R. P., Structure Enhancement Factor Relationships in Single Gold Nanoantennas by Surface-Enhanced Raman Excitation Spectroscopy. *Journal of the American Chemical Society* **2013,** *135* (1), 301-308.

12. Cheng, S.-C.; Wen, T.-C., Robust SERS substrates with massive nanogaps derived from silver nanocubes self-assembled on massed silver mirror via 1,2-ethanedithiol monolayer as linkage and ultra-thin spacer. *Materials Chemistry and Physics* **2014,** *143* (3), 1331-1337.

13. Dill, T. J.; Rozin, M. J.; Brown, E. R.; Palani, S.; Tao, A. R., Investigating the effect of Ag nanocube polydispersity on gap-mode SERS enhancement factors. *Analyst* **2016,** *141* (12), 3916-3924.

14. Bryant, M. A.; Pemberton, J. E., Surface Raman scattering of self-assembled monolayers formed from 1-alkanethiols at silver [electrodes]. *Journal of the American Chemical Society* **1991,** *113* (10), 3629-3637.

15. Li, S.; Wu, D.; Xu, X.; Gu, R., Theoretical and experimental studies on the adsorption behavior of thiophenol on gold nanoparticles. *Journal of Raman Spectroscopy* **2007,** *38* (11), 1436-1443.

16. Le Ru, E.; Etchegoin, P., *Principles of Surface Enhanced Raman Spectroscopy and related plasmonic effects*. 1 ed.; Elsevier B.V.: 2009.

17. Tallarida, N.; Rios, L.; Apkarian, V. A.; Lee, J., Isomerization of One Molecule Observed through Tip-Enhanced Raman Spectroscopy. *Nano Letters* **2015,** *15* (10), 6386-6394.

18. Zhao, Y.; Liu, X.; Lei, D. Y.; Chai, Y., Effects of surface roughness of Ag thin films on surface-enhanced Raman spectroscopy of graphene: spatial nonlocality and physisorption strain. *Nanoscale* **2014,** *6* (3), 1311-1317.

19. Cançado, L. G.; Beams, R.; Jorio, A.; Novotny, L., Theory of Spatial Coherence in Near-Field Raman Scattering. *Physical Review X* **2014,** *4* (3), 031054.

20. Schedin, F.; Lidorikis, E.; Lombardo, A.; Kravets, V. G.; Geim, A. K.; Grigorenko, A. N.; Novoselov, K. S.; Ferrari, A. C., Surface-Enhanced Raman Spectroscopy of Graphene. *ACS Nano* **2010,** *4* (10), 5617-5626.

21. Sun, Y.; Xia, Y., Shape-Controlled Synthesis of Gold and Silver Nanoparticles. *Science* **2002,** *298* (5601), 2176-2179.

22. Tao, A.; Sinsermsuksakul, P.; Yang, P., Tunable plasmonic lattices of silver nanocrystals. *Nat Nano* **2007,** *2* (7), 435-440.

23. Doherty, M. D.; Murphy, A.; Pollard, R. J.; Dawson, P., Surface-Enhanced Raman Scattering from Metallic Nanostructures: Bridging the Gap between the Near-Field and Far-Field Responses. *Physical Review X* **2013,** *3* (1), 011001.

24. McFarland, A. D.; Young, M. A.; Dieringer, J. A.; Van Duyne, R. P., Wavelength-scanned surface-enhanced Raman excitation spectroscopy. *Journal of Physical Chemistry B* **2005,** *109* (22), 11279-11285.

Chapter 5

Contributions of Polydispersity and Defect Particles to the Raman EF

5.1. Introduction

Raman spectroscopy is a highly advantageous technique for chemical and biological identification because it provides chemical-specific vibrational signatures of analytes, performs over a large wavelength range, can be implemented using portable spectroscopic instrumentation, and is well suited to detection in aqueous environments.[1-3] These features enable high analyte specificity along with real-time measurement capabilities. However, typical values for Raman scattering cross-sections are low compared to other optical processes, ranging between 10^{-31} – 10^{-29} cm^2 per molecule. Surface-enhanced Raman spectroscopy (SERS) overcomes these low scattering cross-sections by placing the analyte within the evanescent field generated at a metal surface, resulting in the near-field amplification of scattered light.[4] Colloidal metal nanoparticles composed of Ag, Au, and other highly conducting metals are highly studied substrates for SERS[5-9] because they support localized surface plasmon resonances (LSPRs) that produce intense electromagnetic fields localized at the nanoparticle surface and within nanoparticle junctions.[10-14] In addition, colloidal nanoparticles are readily synthesized using wet chemistry, and are thus amenable to solution post-processing and chemical surface modification to generate SERS substrates for chemical detection. As examples, colloidal metal nanoparticles have been used as SERS substrates for trace detection of molecules such as narcotics[15] and pesticides,[16] and to characterize the chemical reactions of surfaces[17] and catalysts.[12]

A critical challenge in SERS sensing is the ability to predict the optical behavior — and thus, the chemical sensitivity — of these nanoparticle-based

substrates. There has been a considerable amount work trying to predict Raman EFs. Experimentally determined hotspot distributions on SERS substrates have been reported.[13] Experiment and simulation have been paired to explain the EF resulting from shaped nanoparticles, dimers, and clusters.[5, 18, 19] More recently, studies have used simulations and electron tomography to analyze near-atomic scale features, and their effects on optical properties.[20-22] While these studies are carefully conducted, they are limited to single particles or clusters and not representative of the polydispersity resulting from an ensemble colloidal solution. Most colloidal nanoparticles are synthesized in batch quantities and possess a large degree of heterogeneity in comparison to lithographically generated metal nanostructures. A typical size dispersion curve for colloidal nanoparticles is Gaussian,[23, 24] where larger nanoparticles exhibit red-shifted dipolar LSPR resonances and smaller nanoparticles exhibit blue-shifted LSPR resonances from the average peak position in the optical scattering spectrum. Complex shapes and assemblies can also introduce higher-order LSPR modes as well as dark plasmon modes, where near-field enhancement is high while far-field scattering is suppressed.[5, 25-27] As heterogeneity increases, the optical scattering response corresponding to LSPR excitation broadens, while the near-field enhancements of non-ideally sized nanoparticles are shifted off-resonance. Because SERS sensing typically relies on ensemble measurements where the optical readout is collected from many nanoparticles[28] experimental SERS sensitivities can vary dramatically from predictions that are based on the optical behavior of singular

nanoparticle size, shape, or assemblies where sample dispersity is not taken into account.[18, 29]

Here we construct an analytical model for the effects of nanoparticle size dispersity in the SERS response of colloidal Ag nanocubes arranged on flat Au films. We and others have recently demonstrated that these colloidal structures behave as large-scale plasmonic surfaces that exhibit high electromagnetic field enhancements.[30, 31] This is due to the highly confined optical gap generated between the colloidal nanocube and the metal film when they are separated by distances of < 20 nm. These colloidal surfaces have already been demonstrated as substrates for perfect optical absorption[32] and fast fluorescence emission.[33] In addition, Ag nanocubes present an ideal model system to understand the effects of colloidal dispersity on SERS response because they are single crystalline and nearly atomically planar, which means that they can be accuractely modeled using electrodynamic simulations to account for different nanoparticle sizes and shapes (i.e. using simple parameters such as nanocube edge length and radius of curvature of cube corners). Here, we investigate the effects of colloidal dispersity by measuring the SERS enhancement factor (EF) for Ag nanocube substrates and comparing these results with our electrodynamic simulations. We measure the size and shape dispersity of typical Ag nanocube samples to simulate the optical response of an ensemble of nanoparticles, rather than a single nanoparticle. Our analysis shows that by taking into account a range of nanocube sizes and shapes, we can predict the broad optical resonances and EFs observed in our experimental colloidal SERS substrates.

5.2. Experimental Raman EFs for Various Nanocube Size Distributions

In order to determine colloidal Ag nanocube size distributions, we analyzed multiple SEM images (Figure 5.1.) for SERS substrates fabricated with five different average nanocube sizes. We measured nanoparticle size and radius of curvature (ROC). Using standard image analysis software (ImageJ), we measured edge lengths of at least 100 nanocubes per substrate. Their distributions are displayed as histograms in Figure 5.2. for five different nanocube samples. The distributions were fit to a Gaussian curve to calculate average edge lengths and standard deviations. The same image analysis software was used to determine the ROC for the corners of the

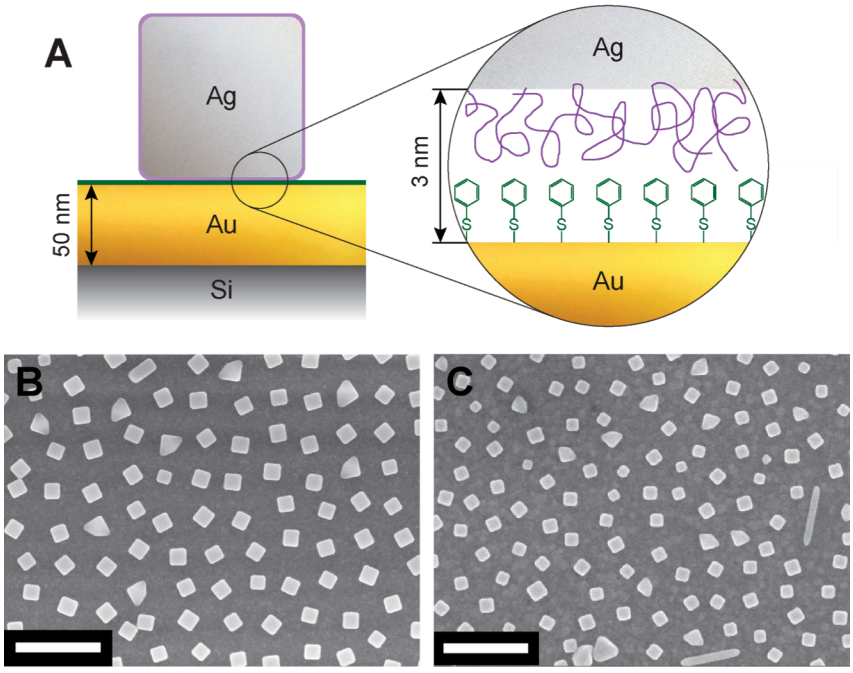

Figure 5.1. SERS Substrate schematic and representative SEM Images. A) A schematic of the nanocube on an Au-thin film as well as the PhSH and PVP layers producing a 3 nm dielectric spacer layer (inset). B,C) SEM Images of (B) 96 nm and (C) 74 nm nanocube dispersions deposited on an Au thin-film. Scale bars = 500 nm.

nanocubes. The ROC however is more difficult to accurately measure due to resolution limits of SEM imaging. The average sizes, standard deviations, and ROC for the SERS substrates are listed in Table 5.1.

Table 5.1. Nanocube sample size distributions.

Mean Nanocube Size (nm)	Standard Deviation (nm)	Radius of Curvature (nm)
70	4	17
74	4	16
91	6	12
96	6	11
105	5	11

We performed Raman spectroscopy on these nanocube substrates in order to determine the effect of average nanocube size on the Raman enhancement factor (EF). Figure 5.1.A shows a schematic of a nanocube SERS substrate that is functionalized with the Raman reporter, PhSH, a well-studied and characterized molecule often used

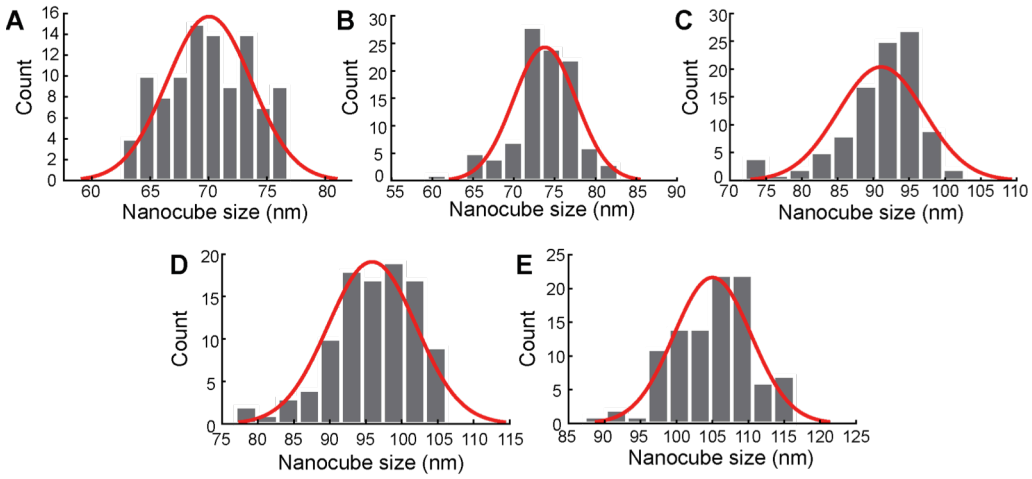

Figure 5.2. Histogram of size distributions for five different SERS substrates fabricated with varying nanocube sizes: A) 70 nm, B) 74 nm, C) 91 nm, D) 96 nm, E) 105 nm.

to estimate Raman EFs.[34, 35] PhSH is also known to form well-packed molecular monolayers on Au surfaces, which enables us to obtain an accurate estimate of the number of reporter molecules located in the optical gap.[36] The remaining gap between the nanocube and film results from a thin layer of PVP on the nanocube leftover from the colloidal synthesis. The lateral spacing between individual nanocubes on the substrate is sufficient to ensure no inter-nanoparticle coupling occurs.[32]

Figure 5.3. shows the average PhSH SERS spectra collected for each of the five SERS substrates. Table 2 shows the SERS intensities at the 1024 cm^{-1} vibrational mode for each substrate. All intensities fall in the range of 1.07 – 2.3 x 10^5 counts. Using these intensities, we calculated the Raman EF to approximate how much the Raman scattering intensity is increased per molecule for a given SERS substrate using the following equation:[26]

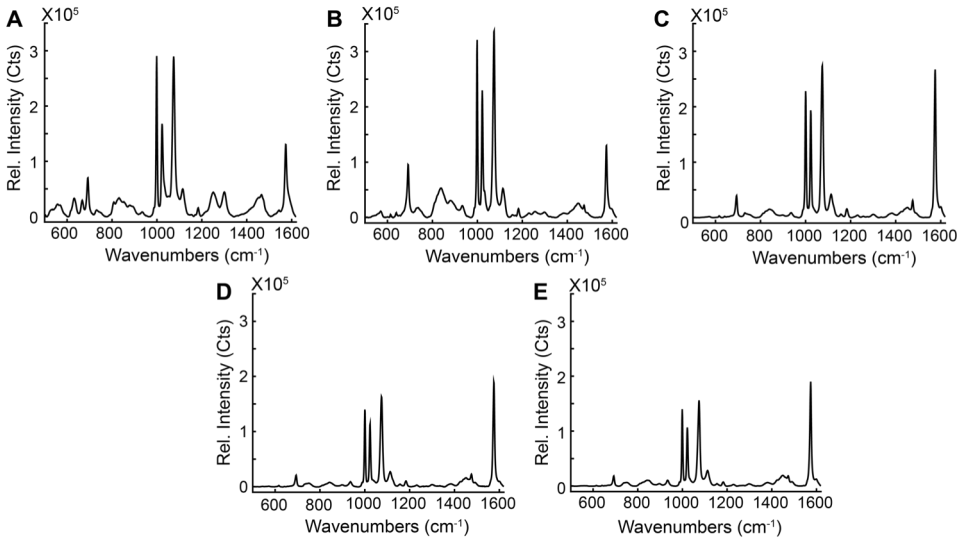

Figure 5.3. Average SERS spectra from five different SERS substrates fabricated from different sized nanoparticles (intensity displayed in counts): A) 70 nm, B) 74 nm, C) 91 nm, D) 96 nm, E) 105 nm. Each spectra is an average of 100 individual spectra collected from random points on the substrate.

$$EF = \left(\frac{I_{SERS}}{I_{Raman}}\right)\left(\frac{N_{Raman}}{N_{SERS}}\right) \qquad (5.1)$$

Where I_{SERS} and I_{Raman} are the Raman intensities for the SERS substrates and bulk PhSH samples respectively. N_{SERS} and N_{Raman} are the number of Raman molecules from which the intensities originate and are calculated using the PhSH bulk density and literature packing values for a molecular monolayer of PhSH on an Au surface.[37] Laser spot sizes were determined by scanning over a cleaved Si edge. N_{SERS} is then normalized to the density of nanocubes on each SERS substrate. All EFs were calculated at the 1024 cm^{-1} vibrational mode, which corresponds to the ring breathing mode and does not depend on molecular orientation.[4] Error in EF was determined from the standard deviation in the measured I_{SERS} values; error for I_{Raman} was considered negligible.

5.3. Simulated Raman EFs of Nanocubes

5.3.1. Simulated Single Nanocube EFs

As previously reported, our simulation results show the appearance of a resonant optical cavity that is confined to the gap between the Ag nanocube and Au film.[31] Figure 5.4.B-F show the electrical field distributions for Ag nanocubes with edge lengths of 70, 74, 91, 96, and 105 nm, respectively. The color maps are obtained by simulating the electrical field enhancement, $|E/E_o|$ at an excitation wavelength of 783 nm, the data point nearest the 785 nm Raman laser line. The field distributions in Figure 5.4. are characterized by a symmetric mode where reflections of the cavity resonance occur at the edges of the nanocube. The symmetry of these plasmon modes

arises from the waveguide-like nature of the cavity modes supported in metal-insulator-metal cavities.[30] The electric field profiles shown in Figure 5.4.B-F correspond to the lowest order dipolar mode, or the fundamental waveguide mode. This resonance is intimately linked to both nanocube size and gap height.[32]

Figure 5.4.G plots the Raman EF versus wavelength for each of the Ag

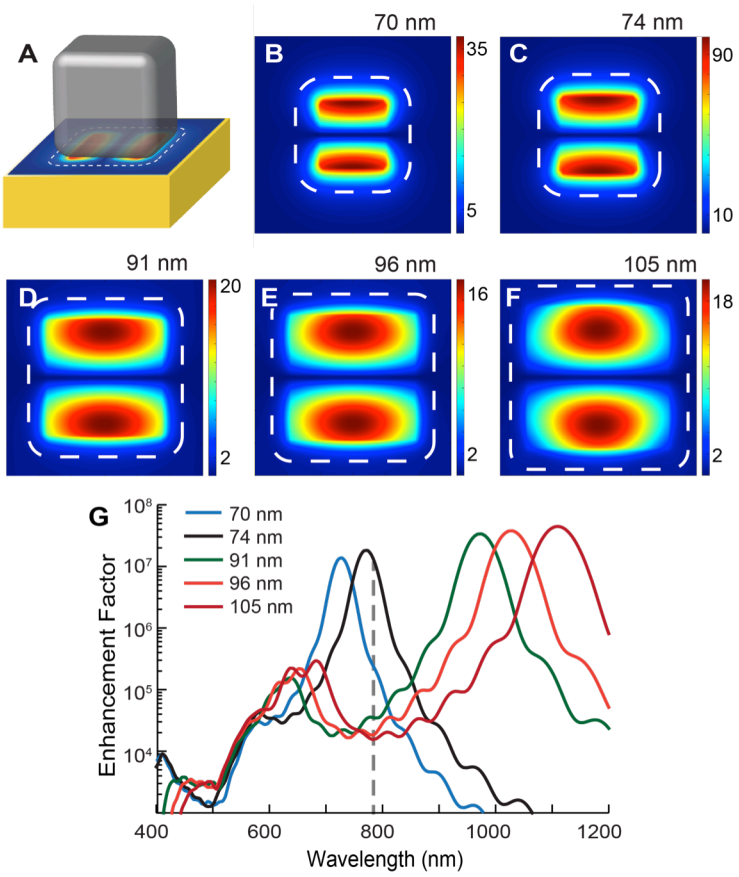

Figure 5.4. Computed field enhancement profiles and single nanocube Raman enhancement factors. A) A cartoon of a silver nanocube flat on an Au-thin film, and the field intensity profile solved at 783 nm for each of five different nanocube sizes B) 70 nm, C) 74 nm, D) 91 nm, E) 96 nm, and F) 105 nm. Dashed white lines represent the footprint of the cube. G) Raman enhancement factors for 70, 74, 91, 96, and 105 nm silver nanocube SERS substrates. The ringing artifacts in the EF profiles are likely caused by reflections in the PML. It is also possible they are caused by the finite time window used in an FDTD simulation which produces the ringing when Fourier transformed to the frequency domain.[43]

nanocube substrates. An average Raman EF for each nanocube size is calculated by summing $|E/E_o|^4$ at each pixel (1x1 nm) and normalizing to the cross-sectional area of each nanocube. This calculation was carried out at discrete wavelengths over the range of 300-1300 nm. The maximum EFs correspond to excitation at the fundamental resonance. The position of the maximum EF shifts by approximately 10 nm per nanometer increase in edge length. At 785 nm, we observe a maximum $|E/E_o| = 97.1$ for a 74 nm Ag nanocube, whereas a cube only 4 nm smaller in edge length has a maximum field enhancement of $|E/E_o| = 36.9$, confirming a strong dependence on size. Table 2 shows the calculated Raman EFs resulting from single nanocube models. For excitation at 785 nm, a 74 nm nanocube possesses a Raman EF = 1.24×10^7 which is 54 times larger than that of a 70 nm nanocube that possesses EF = 2.29×10^5. Ag nanocubes with edge lengths of 91, 96, and 105 nm all possess Raman EFs near 10^4, almost 3 orders of magnitude less than the smaller cubes. Other studies have shown similar results indicating strong size dependence for differently shaped colloidal metal nanoparticles.[30, 38, 39] In general, colloidal size-tuning where the nanoparticle LSPR is frequency-matched to the Raman excitation source is a widely accepted mechanism to engineer colloidal metal nanoparticles with maximum Raman EFs.

5.3.2. Simulated Ensemble Nanocube EFs

To accurately predict the effect of size dispersity on Raman EF, we used our single-nanoparticle FDTD simulation results to model the optical response of an ensemble of Ag nanocubes that possess a range of edge lengths. Each ensemble EF was calculated by using a weighted average of the EFs for five differently sized

nanocubes. The five sizes for each ensemble EF were determined from the experimentally determined size distributions shown in Figure 5.2. We chose to include the optical response for Ag nanocubes with edge lengths corresponding to the mean size, the mean size ± one standard deviation, and the mean size ± two standard deviations. The ensemble EF curve was generated by weighting each of these components to its population count on the Gaussian fits shown in Figure 5.2., roughly approximating the real size distribution of the colloidal sample.

The ensemble EFs calculated for 70, 74, 91, 96, and 105 nm nanocube samples are plotted in Figure 5.5. (gray shaded region) along with the simulation results for

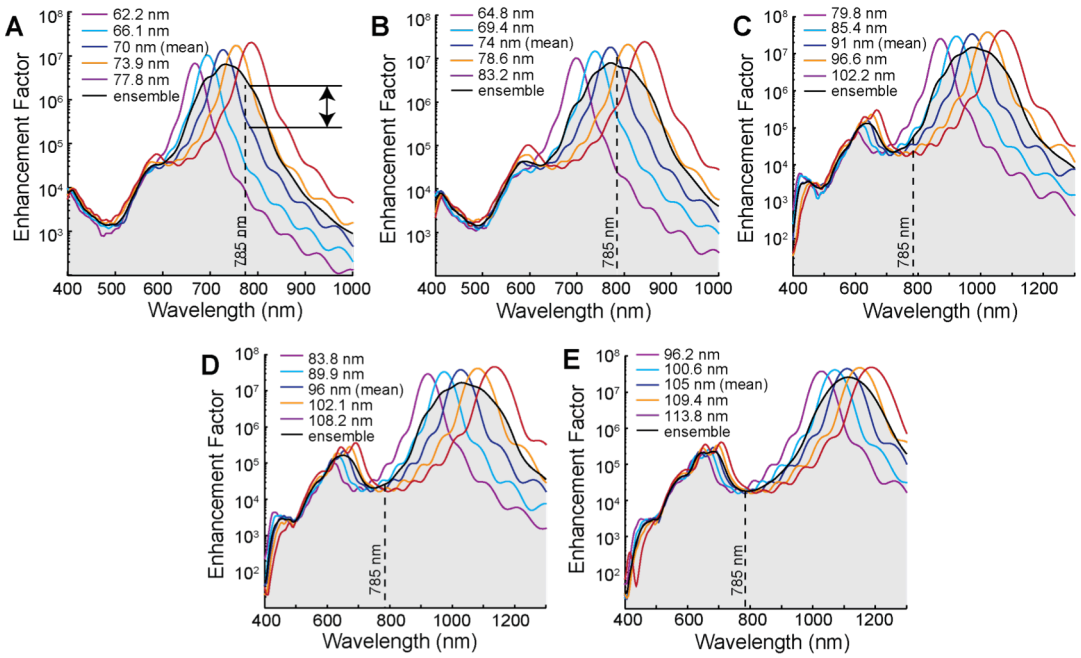

Figure 5.5. Calculation of ensemble EFs for different NP size distributions A) 70 nm, B) 74 nm, C) 91 nm, D) 96 nm, and E) 105 nm. Each ensemble EF is calculated by simulating five different nanocube sizes and generating a weighted average. Nanocube edge lengths were chosen to be representative of a Gaussian distribution of nanocube sizes, as determined by SEM image analysis. Nanocube models were constructed for edge lengths corresponding to the average nanocube size and ± one or two standard deviations.

each single-nanoparticle component that contributes to the weighted average (colored lines). The Raman EF curves for the 70 and 74 nm nanocube ensembles differ significantly from the EF curves for the single nanocubes, specifically with respect to peak broadening of the LSPR band. The 91, 96, and 105 nm nanocube ensembles exhibit resonances far enough from 785 nm that the EFs calculated for a size-disperse ensemble sample is not significantly different from the initial single nanocube models.

Table 5.2. Experimental and simulated Raman intensities and enhancement factors for each SERS substrate. All values are calculated at 785 nm.

	70 nm	**74 nm**	**91 nm**	**96 nm**	**105 nm**
I_{SERS} (1024 cm^{-1}) (X 10^5 Counts)	1.68 ± 0.41	2.30 ± 0.25	1.94 ± 0.16	1.14 ± 0.12	1.07 ± 0.09
Experimental EF (X 10^6)	2.47 ± 0.61	2.61 ± 0.28	2.21 ± 0.18	1.10 ± 0.11	1.16 ± 0.10
Single nanocube EF	2.29 x 10^5	1.24 x 10^7	3.51 x 10^4	1.86 x 10^4	1.56 x 10^4
Ensemble nanocube EF	1.97 x 10^6	6.89 x 10^6	5.69 x 10^4	2.63 x 10^4	1.82 x 10^4

5.4. Discussion

Figure 5.6. shows a plot of our simulated and experimental Raman EFs as a function of average nanocube size. Our single nanocube models predict the highest Raman EF of 1.24 x 10^7 for a nanocube with an edge length of 74 nm, whereas the Raman EF drops by almost three orders of magnitude for nanocubes over 90 nm. Our experiments, however, show that this decrease is only by a factor of two. Our ensemble nanocube models predict a large peak broadening in the overall LSPR resonance of each SERS substrate, which may account for this discrepancy. Accounting for the peak broadening that accompanies a disperse colloidal sample

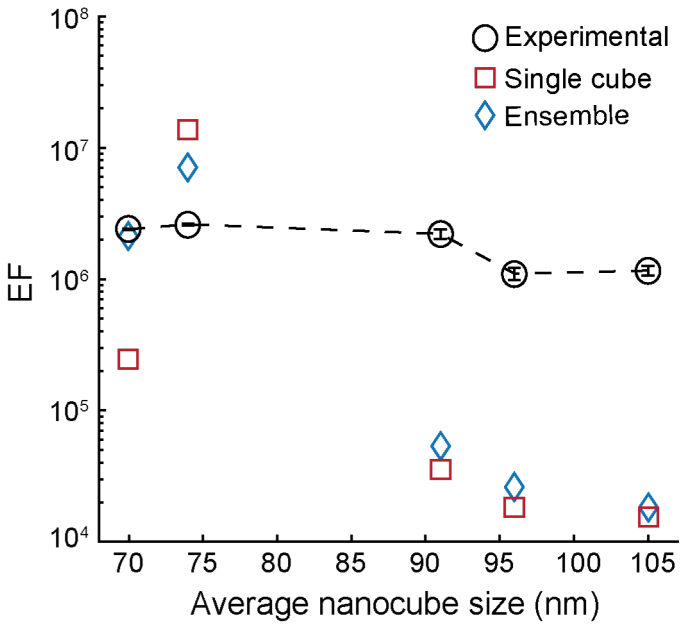

Figure 5.6. EF values versus nanoparticle size distribution. Black circles represent experimental EF determined at the 1024 cm^{-1} peak and their errors. Red squares indicate single nanoparticle EFs as determined by computer simulation. The blue diamonds indicate ensemble EFs determined by modeling nanoparticle size distribution.

allows us to more accurately predict the optical response for small nanocubes whose resonances lie near the excitation wavelength. However, our analytical model does not account for the large Raman EFs observed for substrates composed of large nanocubes (> 90 nm), which we observe to give large EFs even though their LSPRs are off-resonance.

This discrepancy for SERS substrates composed of larger Ag nanocubes is likely due to the contributions from shape heterogeneity, which can have large effects on the resonance and which are not accounted for in our analytical model. Figure 5.1. shows that our colloidal substrates are composed of many "defect" nanoparticles that posses other polyhedral shapes (e.g. rods and tetrahedra), rounded corners, or form small nanoparticle clusters. Figure 5.7.A shows the field distribution profiles for a 100

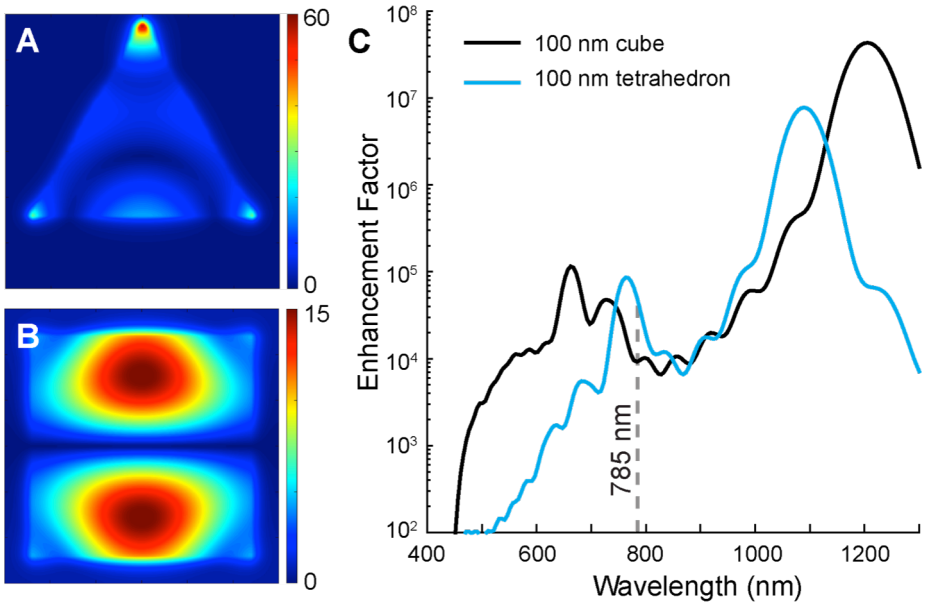

Figure 5.7. Effect of shape heterogeneity on enhancement factor. A) Calculated field enhancement profile of an Ag tetrahedron with edge length = 100 nm, and B) field enhancement profile of an Ag nanocube with edge length = 100 nm (783 nm excitation). C) Wavelength-dependent EF for the tetrahedral nanoparticle and nanocube modeled in parts A and B.

nm nanocube and a 100 nm tetrahedron, a common shape defect observed in our colloidal SERS substrates. At an excitation wavelength of 785 nm, the maximum field intensity is $|E/E_0| = 55.2$ for the tetrahedron and $|E/E_0| = 15.4$ for the nanocube. While the field intensity is higher for the tetrahedron, the optical mode of the cube extends over a larger surface area. As a result, the two polyhedral shapes possess near identical Raman EFs at this excitation wavelength (Figure 5.7.C).

We also considered the effect the orientation of silver nanocubes may have on the Raman EF. Nanoparticle orientation relative to incident light is known to significantly affect the plasmon resonance in many systems[27, 40]. We simulated a 70 nm nanocube with a 17 nm radius of curvature oriented with sides parallel to and at 18, 27, and 45° relative to the incident polarization. Figure 5.8.A-D) shows the field

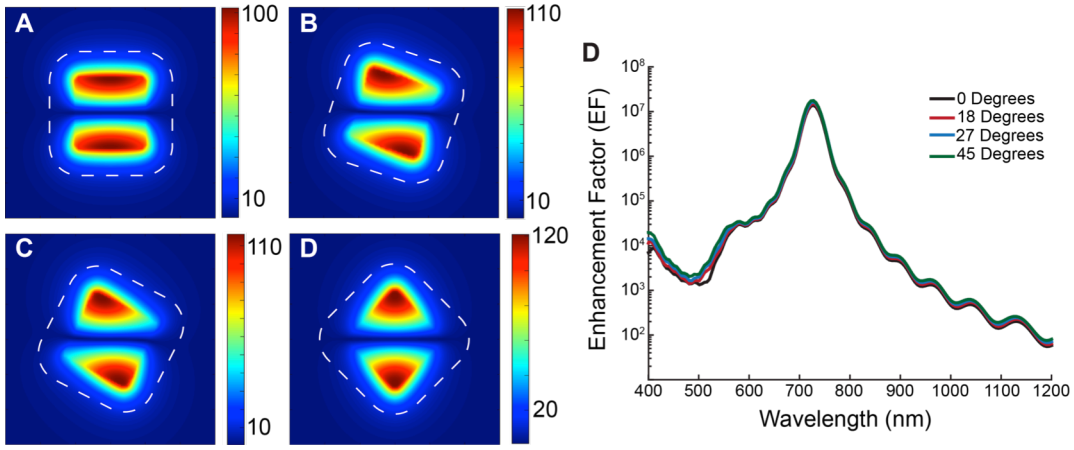

Figure 5.8. Orientational dependence of silver nanocubes. A-D) Field Intensity profiles solved at the resonance (728 nm) for a 70 nm nanocube with a 17 nm radius of curvature at different angular orientations relative to the incident polarization: A) 0 degrees B) 18 degrees C) 27 degrees and D) 45 degrees. E) Raman enhancement factors for different orientations of silver nanocube SERS substrates from 0 to 45 degrees

enhancement profiles. The mode shape changes to fill the volume of the cavity in the direction of the polarization, evolving from rectangles to triangles as the nanocube approaches a 45° orientation. The mode volume doesn't change however, and we found that the resonance location didn't change either. The enhancement factor at 728 nm (at resonance) increases from 1.38 x 10^7 at 0° to 1.76 x 10^7 at 45°. This small change is not considered significant for the experimental discrepancy we observe. To be sure these orientational results were generalizable, we also modeled an 80 nm nanocube with a 5 nm radius of curvature and found a similarly low enhancement factor dependence on polarization.

Figure 5.9. shows the effects of curvature at colloidal nanocube corners on Raman EF. We simulated the field distributions for 70 nm Ag nanocubes modeled with ROCs of 5, 9, 13, and 17 nm. At an excitation wavelength of 785 nm, decreasing the ROC from 17 to 13 nm increases the maximum field intensity from $|E/E_0|$ = 36.9 to

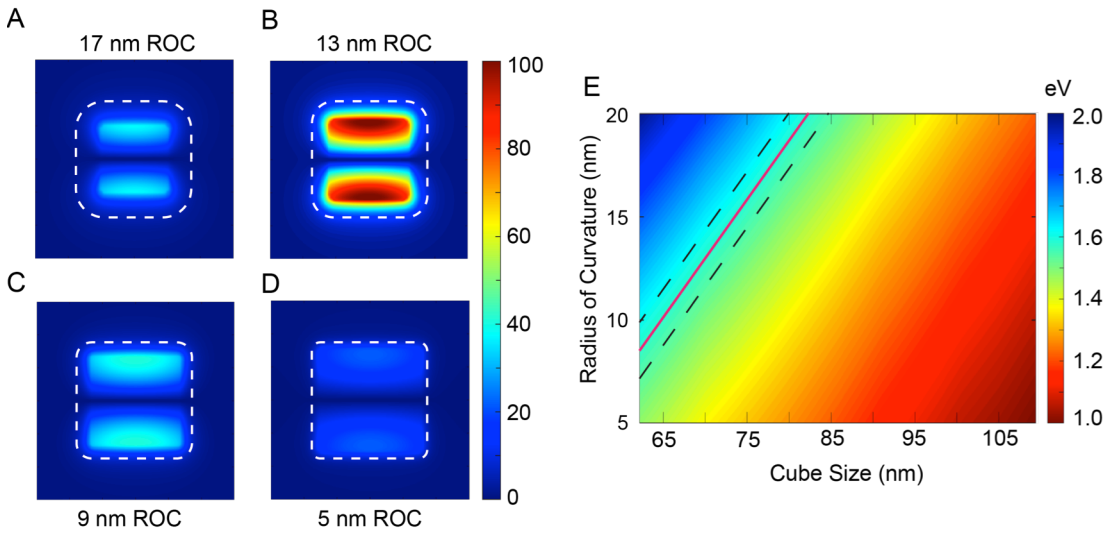

Figure 5.9. FDTD simulations and interpolated data for nanocube resonance when considering both nanocube size and ROC. A-D) Field enhancement profiles at 783 nm for a 70 nm nanocube modeled with A) 17 nm B) 13 nm C) 9 nm and D) 5 nm ROCs. E) Two dimensional heat map of resonance peak position, between the dashed lines is the range of nanocubes which are resonant with a 785 nm excitation source.

$|E/E_0|$ = 101.9 (Figure 5.8.A-D). This results in a significant increase in Raman EF, from EF = 2.29 x 10^5 to EF = 1.80 x 10^7. Further decreasing the ROC leads to a decrease in field intensity and Raman EF as the fundamental LSPR mode becomes red-shifted beyond 785 nm. (Figure 5.9.C,D) To expand this analysis, we plotted the energetic location of the resonance peak as a function of both Ag nanocube size and ROC (Figure 5.9.E). The resonance peak shifts by as much as 300 nm for a fixed nanocube size when the ROC is varied from 2-20 nm. As a visual aid, the regions bounded within the dashed lines denote the nanocube sizes and ROC combinations that are resonant at 785 nm (Figure 5.9.E, solid red line).

5.5. Experimental and Computational Methods

SERS Substrate Fabrication: Ag nanocubes were synthesized using a modified polyol reaction as previously described.[41] In brief, $AgNO_3$ is reduced in 1-5

pentanediol heated to ~200° C. $CuCl_2$ and polyvinylpyrrolidone (PVP, MW = 55,000) are added to control the nucleation and growth processes, and also to passivate the nanocube surfaces after growth. In order to decrease polydispersity and remove non-cubic particles, nanocubes were vacuum filtered. Millipore Durapore membranes were used in three different sizes to remove sequentially smaller nanoparticles: 650 nm, 450 nm, and 220 nm. The final nanocubes are then concentrated and washed via centrifugation several times to remove excess PVP, and resuspended in $CHCl_3$.

Nanocube films are made via a Langmuir Blodgett trough (KSV Nima KN2001).[42] The nanocube suspension is slowly drop-cast onto a deionized water subphase. After the nanocubes equilibrate, they are isothermally compressed at a rate of 3 cm^2/min to a desired surface pressure between 0 and 2 mN/m. The film was then transferred to a 50 nm Au thin-film sputtered on (100) Si. The Au is treated with 1 mM (ethanol) thiophenol (PhSH) overnight to form a self-assembled monolayer (SAM) on the Au surface. It is then copiously rinsed with EtOH and dried under N_2. The nanocube film is then transferred to the Au via dip coating and allowed to dry. Figure 5.1.A shows a schematic of a single nanocube deposited on the functionalized Au. Figure 5.1.B,C shows SEM images of two SERS substrates fabricated from different sized nanocubes, with averages of 74 and 96 nm.

Raman Data Collection: All data was collected on a Renishaw inVia Raman microscope. A 785 nm stripe diode laser was used with an illumination power of < 1 mW. A 50x, 0.9 NA objective was used for both illumination and collection of Raman data. For each SERS substrate, 100 data points were collected at random locations and

averaged. For bulk PhSH Raman, 10 data points were collected and averaged under the same illumination conditions.

Electrodynamic Simulations: Electromagnetic modeling was performed with Lumerical FDTD Solutions. Ag nanocubes (Palik dielectric data) were modeled in 3 dimensions with a 50 nm Au thin film as a substrate. A 3 nm spacer with index of refraction (n) = 1.4 was added to reflect the organic spacing layers (PhSH and PVP). Incident light was injected normal to the substrate, and polarized parallel to the (100) faces. A 1 nm global mesh was used; to improve accuracy, the mesh size was reduced in the gap region to 0.5 nm. The model was solved at 200 points at 5 nm intervals from 300 nm to 1300 nm. All $|E/E_0|$ and EF values were calculated for 785 nm using a cubic spline interpolation from the surrounding data points. All electric field profiles shown are at 783 nm, the data point nearest our 785 nm Raman laser line. The electric field measurements were calculated in the plane of the Au thin film, 1 nm offset from the surface.

5.6 Conclusions

Our results show that size and shape dispersity in colloidal metal nanoparticle samples can have a significant effect on the resulting Raman EF for nanoparticle-based SERS substrates. Single nanoparticle models do not provide an accurate prediction of Raman EFs, which can lead to inaccurate predictions of SERS detection levels. Using an analytical model that weight averages the optical response of multiple single nanoparticle models that possess different sizes can improve this accuracy. Extending these models to encompass shape dispersity requires image analysis to

gauge ROC distributions and counts for other shape defect populations. Finally, accounting for other variables such as Ag surface roughness and deviations in optical gap thickness may also improve the accuracy of our ensemble model.

Chapter 5 is a reformatted reprint in full, of the material from: **Dill, T. J.**, Rozin, M. J., Brown, E. R., Palani, S., Tao. A. R., Investigating the Effects of Polydispersity on Gap-Mode SERS Enhancement Factors. *The Analyst* **2016**, 141 (12), 3916-3924. The dissertation author was the principal researcher and author of this paper.

5.7 References

1. Harris, D. C.; Betolucci, M. D., *SYMMETRY AND SPECTROSCOPY An Introduction to Vibrational and Electronic Spectroscopy*. 2nd ed.; Dover Publications, Inc.: 1989.

2. *Raman Spectroscopy for Nanomaterials Characterization*. 1 ed.; Springer-Verlag Berlin Heidelberg: 2012; p 646.

3. Ru, E. L.; Etchegoin, P., *Principles of Surface-Enhanced Raman Spectroscopy: and related plasmonic effects*. Elsevier Science: 2008.

4. Le Ru, E.; Etchegoin, P., *Principles of Surface Enhanced Raman Spectroscopy and related plasmonic effects*. 1 ed.; Elsevier B.V.: 2009.

5. Kleinman, S. L.; Sharma, B.; Blaber, M. G.; Henry, A.-I.; Valley, N.; Freeman, R. G.; Natan, M. J.; Schatz, G. C.; Van Duyne, R. P., Structure Enhancement Factor Relationships in Single Gold Nanoantennas by Surface-Enhanced Raman Excitation Spectroscopy. *Journal of the American Chemical Society* **2013,** *135* (1), 301-308.

6. Blaber, M. G.; Schatz, G. C., Extending SERS into the infrared with gold nanosphere dimers. *Chemical Communications* **2011,** *47* (13), 3769-3771.

7. Tao, A. R.; Yang, P., Polarized Surface-Enhanced Raman Spectroscopy on Coupled Metallic Nanowires. *The Journal of Physical Chemistry B* **2005,** *109* (33), 15687-15690.

8. Rycenga, M.; Xia, X.; Moran, C. H.; Zhou, F.; Qin, D.; Li, Z.-Y.; Xia, Y., Generation of Hot Spots with Silver Nanocubes for Single-Molecule Detection by Surface-Enhanced Raman Scattering. *Angewandte Chemie (International Ed. in English)* **2011,** *50* (24), 5473-5477.

9. Creighton, J. A.; Blatchford, C. G.; Albrecht, M. G., Plasma resonance enhancement of Raman scattering by pyridine adsorbed on silver or gold sol particles of size comparable to the excitation wavelength. *Journal of the Chemical Society, Faraday Transactions 2: Molecular and Chemical Physics* **1979,** *75* (0), 790-798.

10. Sharma, B.; Fernanda Cardinal, M.; Kleinman, S. L.; Greeneltch, N. G.; Frontiera, R. R.; Blaber, M. G.; Schatz, G. C.; Van Duyne, R. P., High-performance SERS substrates: Advances and challenges. *MRS Bulletin* **2013,** *38* (08), 615-624.

11. Gao, B.; Arya, G.; Tao, A. R., Self-orienting nanocubes for the assembly of plasmonic nanojunctions. *Nat Nano* **2012,** *7* (7), 433-437.

12. Ling, X. Y.; Yan, R.; Lo, S.; Hoang, D. T.; Liu, C.; Fardy, M. A.; Khan, S. B.; Asiri, A. M.; Bawaked, S. M.; Yang, P., Alumina-coated Ag nanocrystal monolayers as surfaceenhanced Raman spectroscopy platforms for the direct spectroscopic detection of water splitting reaction intermediates. *Nano Research* **2013,** *7* (1), 132-143.

13. Fang, Y.; Seong, N.-H.; Dlott, D. D., Measurement of the Distribution of Site Enhancements in Surface-Enhanced Raman Scattering. *Science* **2008,** *321* (5887), 388-392.

14. Chen, G.; Wang, Y.; Yang, M.; Xu, J.; Goh, S. J.; Pan, M.; Chen, H., Measuring Ensemble-Averaged Surface-Enhanced Raman Scattering in the Hotspots of Colloidal Nanoparticle Dimers and Trimers. *Journal of the American Chemical Society* **2010,** *132* (11), 3644-3645.

15. Andreou, C.; Hoonejani, M. R.; Barmi, M. R.; Moskovits, M.; Meinhart, C. D., Rapid Detection of Drugs of Abuse in Saliva Using Surface Enhanced Raman Spectroscopy and Microfluidics. *ACS Nano* **2013,** *7* (8), 7157-7164.

16. Li, J. F.; Huang, Y. F.; Ding, Y.; Yang, Z. L.; Li, S. B.; Zhou, X. S.; Fan, F. R.; Zhang, W.; Zhou, Z. Y.; WuDe, Y.; Ren, B.; Wang, Z. L.; Tian, Z. Q., Shell-isolated nanoparticle-enhanced Raman spectroscopy. *Nature* **2010,** *464* (7287), 392-395.

17. Moran, C. H.; Rycenga, M.; Zhang, Q.; Xia, Y., Replacement of Poly(vinyl pyrrolidone) by Thiols: A Systematic Study of Ag Nanocube Functionalization by Surface-Enhanced Raman Scattering. *The Journal of Physical Chemistry C* **2011,** *115* (44), 21852-21857.

18. Lee, S. Y.; Hung, L.; Lang, G. S.; Cornett, J. E.; Mayergoyz, I. D.; Rabin, O., Dispersion in the SERS Enhancement with Silver Nanocube Dimers. *ACS Nano* **2010,** *4* (10), 5763-5772.

19. Fraire, J. C.; Pérez, L. A.; Coronado, E. A., Cluster Size Effects in the Surface-Enhanced Raman Scattering Response of Ag and Au Nanoparticle Aggregates: Experimental and Theoretical Insight. *The Journal of Physical Chemistry C* **2013,** *117* (44), 23090-23107.

20. Perassi, E. M.; Hrelescu, C.; Wisnet, A.; Döblinger, M.; Scheu, C.; Jäckel, F.; Coronado, E. A.; Feldmann, J., Quantitative Understanding of the Optical Properties of a Single, Complex-Shaped Gold Nanoparticle from Experiment and Theory. *ACS Nano* **2014,** *8* (5), 4395-4402.

21. Barbry, M.; Koval, P.; Marchesin, F.; Esteban, R.; Borisov, A. G.; Aizpurua, J.; Sánchez-Portal, D., Atomistic Near-Field Nanoplasmonics: Reaching Atomic-Scale Resolution in Nanooptics. *Nano Letters* **2015,** *15* (5), 3410-3419.

22. Chen, X.; Moore, J. E.; Zekarias, M.; Jensen, L., Atomistic electrodynamics simulations of bare and ligand-coated nanoparticles in the quantum size regime. *Nat Commun* **2015,** *6*.

23. Ershov, A. E.; Isaev, I. L.; Semina, P. N.; Markel, V. A.; Karpov, S. V., Effects of size polydispersity on the extinction spectra of colloidal nanoparticle aggregates. *Physical Review B* **2012,** *85* (4), 045421.

24. Dongjo Kim and Sunho Jeong and Jooho, M., Synthesis of silver nanoparticles using the polyol process and the influence of precursor injection. *Nanotechnology* **2006,** *17* (16), 4019.

25. Nicoletti, O.; de la Pena, F.; Leary, R. K.; Holland, D. J.; Ducati, C.; Midgley, P. A., Three-dimensional imaging of localized surface plasmon resonances of metal nanoparticles. *Nature* **2013,** *502* (7469), 80-84.

26. Doherty, M. D.; Murphy, A.; Pollard, R. J.; Dawson, P., Surface-Enhanced Raman Scattering from Metallic Nanostructures: Bridging the Gap between the Near-Field and Far-Field Responses. *Physical Review X* **2013,** *3* (1), 011001.

27. Tian, X.-D.; Chen, S.; Zhang, Y.-J.; Dong, J.-C.; Panneerselvam, R.; Zhang, Y.; Yang, Z.-L.; Li, J.-F.; Tian, Z.-Q., Self-assembly of subwavelength nanostructures with symmetry breaking in solution. *Nanoscale* **2016,** *8* (5), 2951-2959.

28. Camargo, P. H. C.; Au, L.; Rycenga, M.; Li, W.; Xia, Y., Measuring the SERS enhancement factors of dimers with different structures constructed from silver nanocubes. *Chemical Physics Letters* **2010,** *484* (4–6), 304-308.

29. Rabin, O.; Lee, S. Y., SERS Substrates by the Assembly of Silver Nanocubes: High-Throughput and Enhancement Reliability Considerations. *Journal of Nanotechnology* **2012,** *2012*, 12.

30. Lassiter, J. B.; McGuire, F.; Mock, J. J.; Ciracì, C.; Hill, R. T.; Wiley, B. J.; Chilkoti, A.; Smith, D. R., Plasmonic Waveguide Modes of Film-Coupled Metallic Nanocubes. *Nano Letters* **2013,** *13* (12), 5866-5872.

31. Moreau, A.; Ciraci, C.; Mock, J. J.; Hill, R. T.; Wang, Q.; Wiley, B. J.; Chilkoti, A.; Smith, D. R., Controlled-reflectance surfaces with film-coupled colloidal nanoantennas. *Nature* **2012,** *492* (7427), 86-89.

32. Rozin, M. J.; Rosen, D. A.; Dill, T. J.; Tao, A. R., Colloidal metasurfaces displaying near-ideal and tunable light absorbance in the infrared. *Nat Commun* **2015,** *6*.

33. Rose, A.; Hoang, T. B.; McGuire, F.; Mock, J. J.; Ciracì, C.; Smith, D. R.; Mikkelsen, M. H., Control of Radiative Processes Using Tunable Plasmonic Nanopatch Antennas. *Nano Letters* **2014,** *14* (8), 4797-4802.

34. Li, S.; Wu, D.; Xu, X.; Gu, R., Theoretical and experimental studies on the adsorption behavior of thiophenol on gold nanoparticles. *Journal of Raman Spectroscopy* **2007,** *38* (11), 1436-1443.

35. Kulkarni, T. B. a. G. U., Femtoliter silver cups as surface enhanced Raman scattering active containers. *Nanotechnology* **2009,** *20* (4), 045504.

36. Blum, C.; Opilik, L.; Atkin, J. M.; Braun, K.; Kämmer, S. B.; Kravtsov, V.; Kumar, N.; Lemeshko, S.; Li, J.-F.; Luszcz, K.; Maleki, T.; Meixner, A. J.; Minne, S.; Raschke, M. B.; Ren, B.; Rogalski, J.; Roy, D.; Stephanidis, B.; Wang, X.; Zhang, D.; Zhong, J.-H.; Zenobi, R., Tip-enhanced Raman spectroscopy – an interlaboratory reproducibility and comparison study. *Journal of Raman Spectroscopy* **2014,** *45* (1), 22-31.

37. McFarland, A. D.; Young, M. A.; Dieringer, J. A.; Van Duyne, R. P., Wavelength-scanned surface-enhanced Raman excitation spectroscopy. *Journal of Physical Chemistry B* **2005,** *109* (22), 11279-11285.

38. Banholzer, M. J.; Millstone, J. E.; Qin, L.; Mirkin, C. A., Rationally designed nanostructures for surface-enhanced Raman spectroscopy. *Chemical Society Reviews* **2008,** *37* (5), 885-897.

39. Lin, W.-C.; Liao, L.-S.; Chen, Y.-H.; Chang, H.-C.; Tsai, D. P.; Chiang, H.-P., Size Dependence of Nanoparticle-SERS Enhancement from Silver Film over Nanosphere (AgFON) Substrate. *Plasmonics* **2010,** *6* (2), 201-206.

40. McLellan, J. M.; Li, Z.-Y.; Siekkinen, A. R.; Xia, Y., The SERS Activity of a Supported Ag Nanocube Strongly Depends on Its Orientation Relative to Laser Polarization. *Nano Letters* **2007,** *7* (4), 1013-1017.

41. Sun, Y.; Xia, Y., Shape-Controlled Synthesis of Gold and Silver Nanoparticles. *Science* **2002,** *298* (5601), 2176-2179.

42. Tao, A.; Sinsermsuksakul, P.; Yang, P., Tunable plasmonic lattices of silver nanocrystals. *Nature nanotechnology* **2007,** *2* (7), 435-40.

43. Liu, M.; Guyot-Sionnest, P.; Lee, T.-W.; Gray, S. K., Optical properties of rodlike and bipyramidal gold nanoparticles from three-dimensional computations. *Physical Review B* **2007,** *76* (23), 235428.

Chapter 6

Quantum Effects Observed in mSERS Substrates with Small Gaps

6.1. Introduction

When multiple plasmonic nanostructures are placed within their respective evanescent fields, their LSPRs become electromagnetically coupled, modifying the plasmon resonance. Coupled LSPRs can lead to an increased electric near-field intensity in the nanojunction between the particles, known as a hotspot, as well as a broadened and red-shifted LSPR.[1-6] Gap-mode hotspots have found use in single molecule sensing as well as for metamaterials.[7-11] It is generally recognized that smaller gaps lead to stronger near-field enhancements as a result of stronger coupling.[12, 13] However, it was shown that there is a limit to this increasing enhancement with decreasing gap size.[14-16] Below a critical gap size, quantum effects such as electron tunneling become important and can strongly modify the LSPR.[17] Tunneling across plasmonic gaps manifests as several measurable effects. In the far-field, a blue-shift and disappearance of the coupled plasmon mode occurs as the gap distance decreases.[18-20] Simultaneously, one or more charge transfer plasmon (CTP) modes may appear.[19-21] In addition, the near-field enhancement becomes quenched.[16, 19, 22] For nanospheres, electron tunneling has only been observed up to ~0.5 nm.[14, 19, 23]

Molecular junctions offer a way to increase the critical tunneling distance and modify the LSPR. The HOMO-LUMO gap of self-assembled monolayers (SAMs) modifies the tunneling barrier height, which helps determine the distance over which electrons can tunnel. Tunneling through gaps up to several nanometer has been observed for molecular tunnel junctions.[24] In a recent example, an increase in gap conductivity is observed when a dithiol molecular SAM is used instead of the

equivalent monothiol to separate an Au nanosphere and a metal film.[25] The higher conductivity of the dithiol results in a large blue-shift of the LSPR. The large interfacial area of Ag nanocubes has been combined with a molecular tunnel junction to observe CTPs in nanocube dimers with gap distances as large as 1.1 nm, larger than the nanosphere equivalent tunnel junction.[26, 27] It has also been shown that molecular conductivity can be increased by the presence of a gap-plasmon, further increasing an electrons ability to tunnel.[28] A thorough understanding of the nature of these quantum effects could lead to improved design for sensors, new optoelectronic devices, or opportunities in nonlinear optics.[29]

Here we demonstrate plasmonic tunneling with tunable critical tunneling distances. By changing the molecular SAMs within the junction, we are able to modify the tunneling barrier height and allow tunneling in gaps as large as 2.5 nm. These large and tunable gap distances are achieved with colloidal patch nanoantennas, a type of metasurface formed when Ag nanocubes (AgNCs) are placed onto a metal film.[30]. Colloidal patch antennas function *via* a fabry-perot like resonance, which allows multiple reflections of a standing wave called a transverse cavity plasmon (TCP)[13, 31]. Colloidal patch antennas were first demonstrated as tunable near-perfect light absorbers.[30, 32] These multiple reflections also create a highly enhanced near-field within the gap which are of great importance when designing a metasurface for use in enhanced spectroscopy.[33, 34] When other nanoparticle geometries are used, such as Ag nanospheres (AgNS), we observe no tunneling, highlighting the importance of geometry in tunneling.

We achieve unprecedented control over gap thickness by fabricating our AgNC metasurfaces in two steps instead of one. AgNCs are deposited onto an elastomeric stamp (PDMS) before coming into contact with a metal film (Figure 6.1A). This allows the ligand on both metal surfaces to be modified independently, resulting in a tunable gap distance of 0.8 – 3.5 nm. This gap size tunability allows us to accurately observe the onset of tunneling. In previous studies investigating AgNC metasurfaces, the smallest gap available was 2-3 nm.[35] This gap was generated by the polyvinylpyrrolidone (PVP) layer that remains on the AgNC surface from synthesis and cannot be removed or exchanged within the junction.[35] Furthermore, by modifying only the ligand on the metal film and changing the molecular interface, we can tune the tunneling gap distance from 1.5 – 2.5 nm. We also demonstrate that these

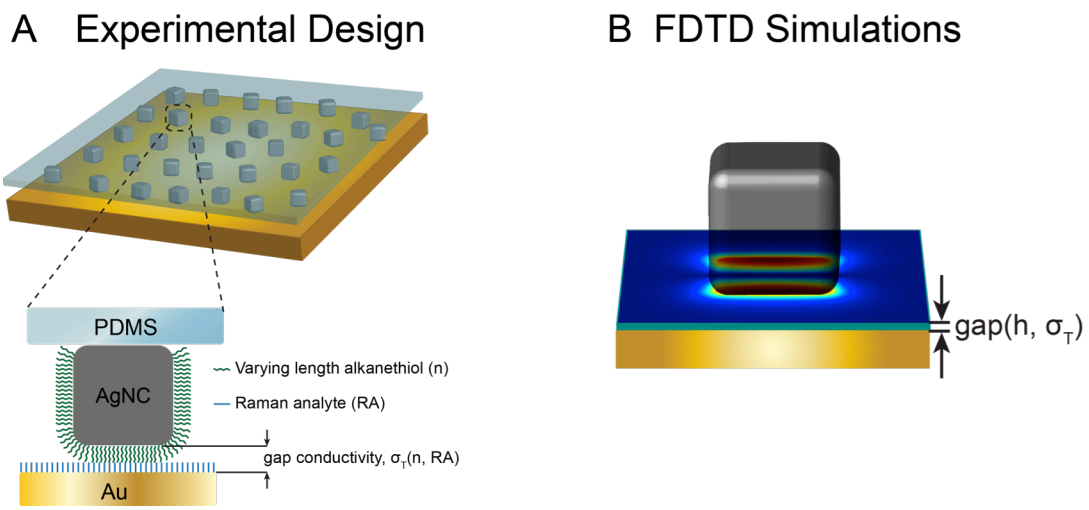

Figure 6.1. Schematic for the design and characterization of the mSERS substrate. (A) A cartoon shows a dispersion of AgNCs deposited onto a PDMS substrate, which was then inverted and adhered to an Au substrate. The schematic of the blown up AgNC shows the interface of a single AgNC. The AgNC ligand is exchanged for an alkeanthiol of chain length (n) before the AgNC comes into contact with the Au surface which can have a Raman analyte (RA). The conductivity of the gap beneath the AgNC is a function of n and RA. (B) Schematic for a classical electrodynamic simulation of an AgNC on an Au substrate separated by a gap. For a given AgNC size, the plasmon response is a function of h and σ_T.

metasurfaces operate as efficient SERS substrates. By tuning the gap distance down to the onset of tunneling, we can increase Raman signal intensity by roughly an order of magnitude. Below the critical gap distance however, the SERS intensity drops significantly. Both our near-field (SERS) and far-field (UV-Vis) measurements support the observation of tunneling.

6.2. Results & Discussion

6.2.1. Tunable Gap-Height Metasurfaces

Figure 6.1.A shows the experimental design of the AgNC metasurfaces and the molecular SAMs used to define the gap. We fabricate AgNC metasurfaces by depositing a film of AgNCs onto a thin PDMS stamp (150 μm thick), then performing a ligand exchange with an alkanethiol of length n (CH_3 (CH_2)n SH) on the AgNCs before adhering the exposed AgNC surface to an Au thin-film substrate. This Au thin-film can be functionalized with a Raman analyte layer (RA). When the two molecular surfaces come into contact, they form the gap of height h. Tunneling through the gap is treated here as analogous to a finite conductivity within the gap region (σ_T), it is a function of both n and RA. Figure 6.1.B shows a schematic of the metasurface geometry simulated *via* the finite difference time-domain (FDTD) method. An example of the near-field enhancement profile of the TCP resonance mode is shown located beneath the AgNC. The simulated plasmon resonance is a function of h and σ_T. The condition of $\sigma_T = 0$ is considered free of electron tunneling regardless of h, and is designated the classical model.

Figure 6.2. shows results from classical modelling of an AgNC metasurface with different values of h. AgNCs were modeled with an edge length of 73.6 nm and a 17 nm corner radius of curvature (ROC), representative of real AgNCs metasurfaces discussed below. The molecular gap between the metal structures is modeled as a dielectric (n= 1.4, $\sigma_T = 0$). Figures 6.2.A,B show the far-field reflectance spectra and the average near-field enhancement respectively. Both field enhancement and reflectance spectra were investigated for h = 5, 4, 3, 2.5, 2, and 1.5 nm. We observe that as h decreases, coupling between the AgNC and the Au film increases and the resonance red-shift from 678 nm (h = 5 nm) to 977 nm (h = 1.5 nm). Simultaneously, the average resonant near-field enhancement increases from 43.6 to 81.5. When the resonance peak locations are plotted against h, we find $\lambda_{Res} \propto 1/\sqrt{h}$ (Figure 6.5. black dashed line). This is consistent with previous theoretical and computational work examining TCP modes in similar structures.[13] Figure 6.2.C shows a reflectance spectra

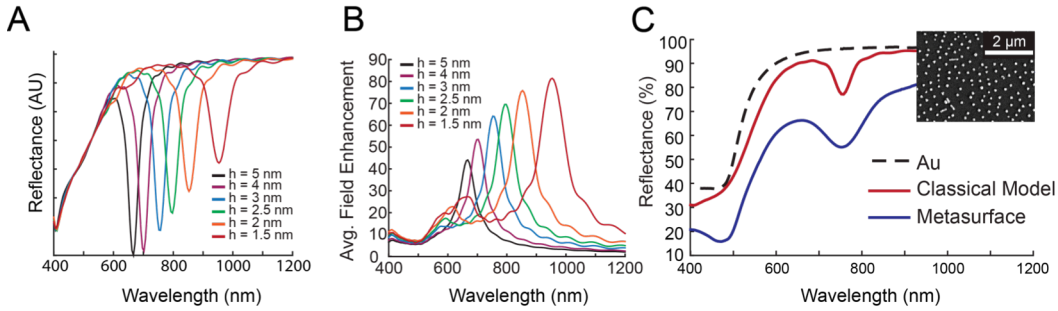

Figure 6.2. FDTD simulations for a AgNC separated by a dielectric gap (n=1.4) from an Au substrate by h. (A) Simulated reflectance spectra of an AgNC on Au for different values of h. (B) Simulated average electric field enhancements within the gap for different values of h. (C) Reflectance spectra for a fabricated AgNC metasurface with a Raman analyte layer of dHDT and an alkanethiol layer of n=11 (dodecanethiol). The inset shows an SEM image of AgNCs deposited on PDMS prior to adhesion to an Au substrate. AgNCs have an average edge length of 73.6 ± 3.7 nm, the gap is estimated at h = 3 nm, $\sigma_T = 0$ (blue line), the red line shows the FDTD simulated reflectance for h = 3 nm. The simulation was modified from (A) to reflect the surface density of AgNCs. The dashed line shows the reflectance spectra of PDMS adhered to Au with no AgNCs.

of a large-area ensemble measurement of an AgNC metasurface. The AgNCs were functionalized with 1-dodecanethiol (DDT, n=11), while the Au substrate was functionalized with deuterated 1-hexadecanethiol (dHDT). We estimate the gap size to be 3.05 nm (see methods). The dip observed in the spectra (peak at 756 nm) has been extensively shown to be the fundamental resonance (TCP) mode.[30, 32, 35] This spectra is compared to a classical simulation of h=3 nm (adjusted from 6.2.A to reflect the surface density of the AgNC metasurface shown in the inset), There is excellent agreement between the simulated and experimental data. The larger full-width half-maximum (FWHM) of the experimental data can be ascribed to the polydispersity of the AgNCs which have a size distribution of 73.6 ± 3.7 nm and corner sharpness of 17 ± 2.2 nm.

6.2.2 Quantum Tunneling in Ag Nanocube Metasurfaces

In order to investigate the gap-size dependent field enhancement and far-field (reflectance) behavior of our metasurfaces, we fabricated metasurfaces functionalized with different length alkanethiols (n = 1, 2, 3, 5, 7, 11, 15, 17). The RA SAM used to coat the Au substrate was thiophenol (PhSH). Figure 6.3.A shows an intensity plot of the reflectance spectra for n=1—17. The black dashed line shows the TCP modes, and the arrows represent decreasing h. As n decreases, we observe a red-shift of the TCP mode, in agreement with classical simulations. Unexpectedly, between n = 5 and n = 3, the TCP mode begins to blue-shift, as well as becomeing both broader and less intense. We suspect this damping is a result of a weakened near-field enhancement

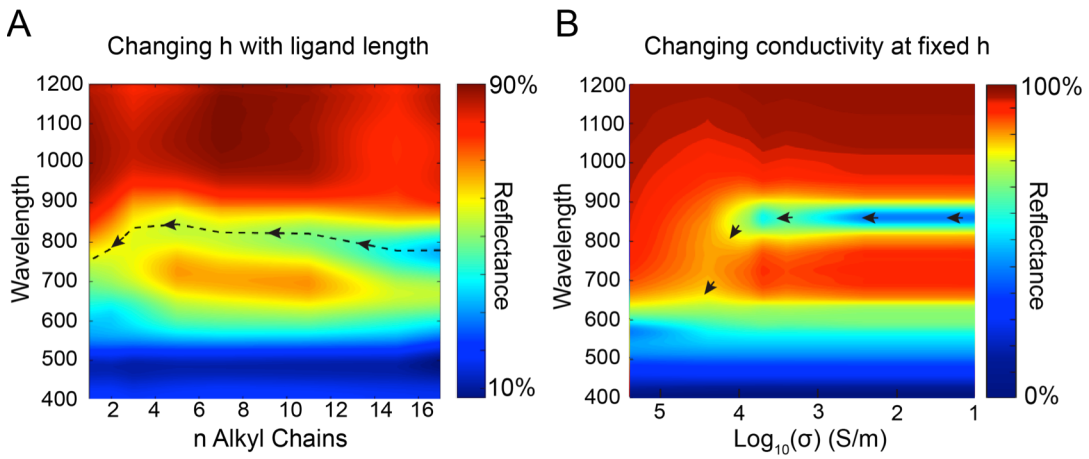

Figure 6.3. Intensity plots of reflectance for experimental and simulated metasurfaces. (A) Intensity plot of metasurfaces fabricated with alkeanethiols of n=1—17, and a Raman analyte layer of PhSH. The resonance peak locations are plotted as a dashed black line, the arrows show the direction of decreashing h. (B) Simulated Reflectance for a metasurface with h = 2 nm and a changing σ_T. The arrows show the direction of the resonance peak location as a function of σ_T.

(discussed below). We also observe for $n \leq 3$, an additional mode appears between 610 – 626 nm.

These findings can be replicated through simulations that incorporate quantum effects. We use an established method known as the quantum corrected model (QCM).[36] The QCM has been validated by comparison to full quantum calculations. The QCM replaces the dielectric gap material with a conductive material (σ_T), allowing electrons to cross the gap. Figure 6.3.B shows the QCM calcluated reflectance spectra with a fixed gap (h = 2 nm), and a σ_T ranging from $\sigma_T = 0.1 – 2.5 \times 10^5$ S/m. At low conductivities, there is no noticeable change in the spectra. In this regime, tunneling is not expected to contribute significantly to the plasmon mode, the absence of the red-shift observed in Figure 6.3.A results from the fixed h. As the conductivity reaches 2.5×10^3 S/m however, we observe a blue-shift as well as damping of the TCP mode. In addition, we observe the appearance of a higher-energy

mode at 575 nm. These observations are consistent with similar simulations perfomed for AgNC dimers.[26] This study ascribed the appearance of the higher energy mode to a CTP as the TCP mode disappears. The reflectance spectra used in Figure 6.3.A are shown in Figure 6.4.A The magnitude of the blue-shift, qualitative damping, and the location of the CTP are all in excellent agreement between experiment and simulation. The accuracy of the QCM suggests the critical tunneling gap is n = 3.

We find other phenomena that could result in the blue-shift to be unlikely. One possibility is shape change or etching of the nanoparticle. It is possible that short chain alkanethiolates are more likely to etch the AgNCs due to lower stability. We performed our alkanethiol ligand exchanges at 1 mM for 1 hr. Subsequent SEM image analysis of AgNC stamps with alkanethiol ligands (n=1-17) shows no change in average nanoparticle size, suggesting ligand based nanoparticle etching is insignificant. Selective etching has also been observed on AgNCs when an a Schottky barrier was formed with a TiO_2 surface.[37] This etch process requires a rectified photocurrent to produce Ag^+, which then diffuses away from the nanoparticle and is reduced. While it is possible that a MIM junction can have a photocurrent[38], the etching observed occurred due to a combination of rectifying junction, high humidity, and long periods light exposure. Since our reflectance measurements were taken in standard humidity environments, within minutes of the AgNCs coming into contact with the Au surface, we find that a blue-shift due to current induced etching is also unlikely.

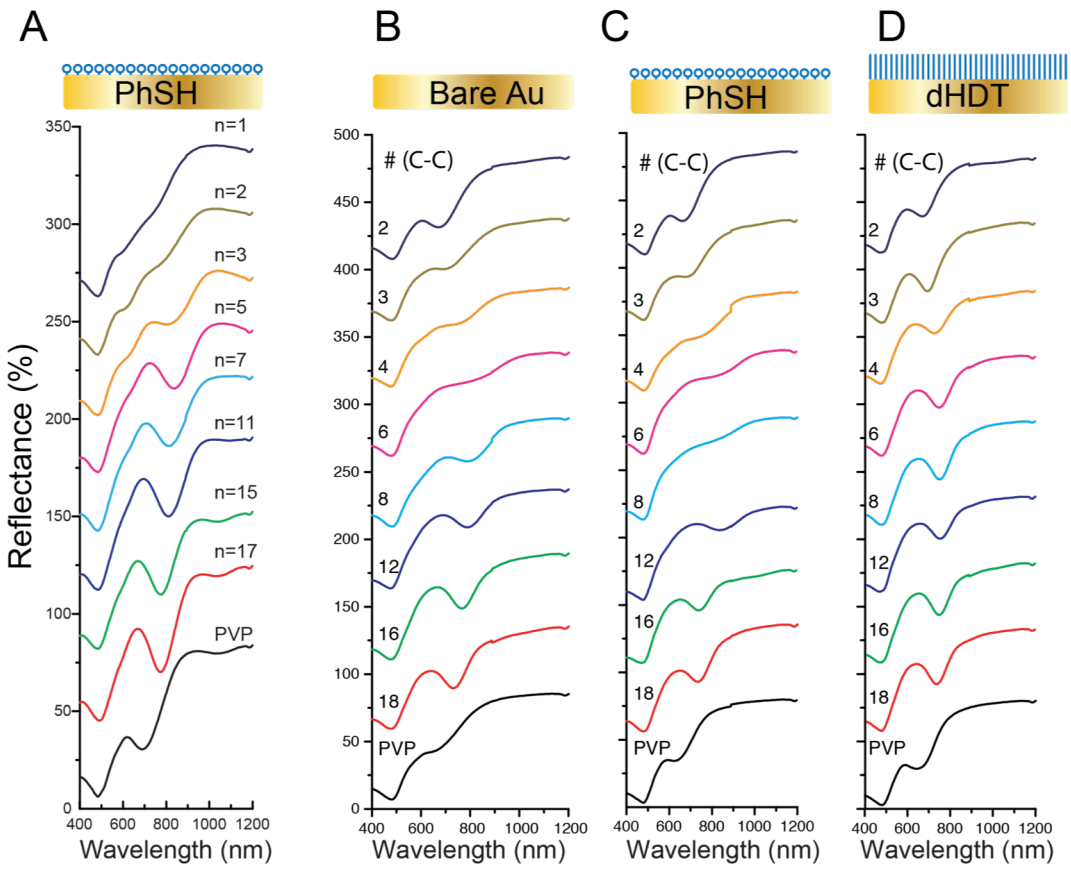

Figure 6.4. Reflectance spectra for metasurfaces fabricated from alkanethiol and PVP capped AgNCs (n = 1—17) on an Au thin-film functionalized with different Raman analyte layers. (A) Reflectance spectra for metasurfaces fabricated with AgNCs of edge length 109 nm ± 10 nm and a PhSH Raman analyte layer. (B-D) Reflectance spectra for metasurfaces fabricated with AgNCs of edge length 73.6± __ nm and a (B) Bare Au, (C) PhSH, and (D) dHDT Raman analyte layer.

Another possible cause for a blue-shift is the lowering of the dielectric constant in the gap. For a specific Au substrate, the only change between metasurfaces is the length of the alkanethiol ligand capping the AgNC. A change in alkanethiol length should have minimal effect on refractive index within the gap relative to the effect it has on h. Control simulations additionally suggest that small changes in refractive index would not result in a resonance shift of more than several nanometers. Thus we

believe changes in refractive index within the gap to be unlikely to affect the LSPR significantly.

6.2.3. The Effect of Surface Chemistry on Tunneling

Figure 6.5. shows the effect of interfacial chemistry on the critical tunneling gap. Metasurfaces are fabricated with alkanethiols (n = 1—17) and PVP (the polymer capping ligand on the AgNC surfaceremaining from synthesis), and are brought into contact with Au substrates functionalized with three different RA layers: bare Au (unfunctionalized), PhSH, and dHDT. The TCP mode is fitted from reflectance data (Figure 6.4.B-D) and plotted against h. We estimated h using literature values (See section 6.3. for details). There are significant differences in the value of h for the critical tunneling gap between RA layers. This difference is dependent only on the

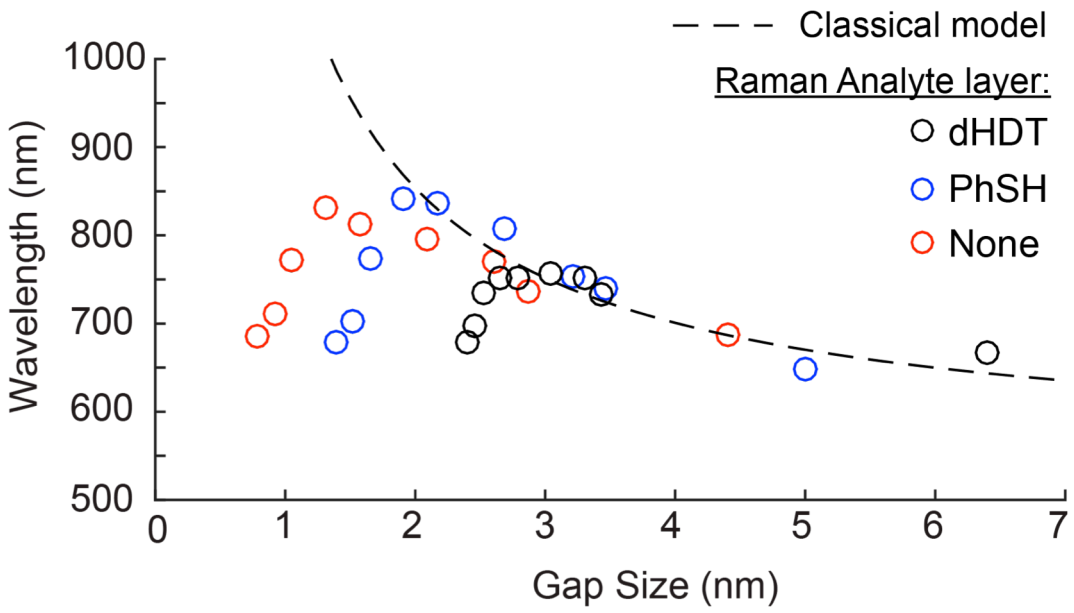

Figure 6.5. Experimentally determined gap-mode resonance (circles) for metasurfaces fabricated from alkanethiol and PVP capped AgNCs (n= 1—17) on an Au thin-film substrate with Raman analyte layers of dHDT (black circles), PhSH (blue circles), and bare Au (red circles). The black dashed line shows the reflectance peak determined by the classical model for AgNCs.

chemistry of the Au surface and the resulting interface between the alkanethiol on the AgNC and the RA on the Au. We observe the critical tunneling gap at 1.3 nm for a bare Au surface, 1.9 nm for a PhSH coated Au surface, and 2.7 nm for a dHDT coated Au surface. This suggests that by varying interfacial chemistry, the conductivity of the gap can be significantly affected. We observe that junction conductivity is highest for a bilayer of interdigitated alkanethiols, followed by an alkanethiol interacting with an aromatic thiol, and lowest for an alkanethiol on an untreated Au surface. It has been previously shown that for DC tunneling, a bilayer of alkanethiols on Hg electrodes will conduct a significantly larger current than the equal thickness equivalent monolayer of alkanethiol.[39] This is in qualitative agreement with the larger critical tunneling gap observed for an RA of dHDT than bare Au. It is also likely that the bare Au surface has several monolayers of H_2O adsorbed to the surface, which could dramatically affect the molecular interface. We hypothesize that CH-CH interactions between interdigitated alkanethiols may play a role in the larger critical tunneling gap for dHDT than PhSH. This significant increase in conductivity over vacuum/air gaps as well as the large interfacial geometry of an AgNC allows plasmonic tunneling at unprecedented and tunable gap distances of several nanometers.

6.2.4. Quantum Tunneling is Only Observed for Ag Nanocubes

AgNC metasurfaces displaying large interfaces and TCPs may enable Quantum effects at larger distances than those of nanospheres. In order to investigate the geometric dependence of our metasurfaces, we repeated our experiments with Ag nanospheres (AgNS) synthesized using a similar polyol method.[40, 41] We simulated Ag

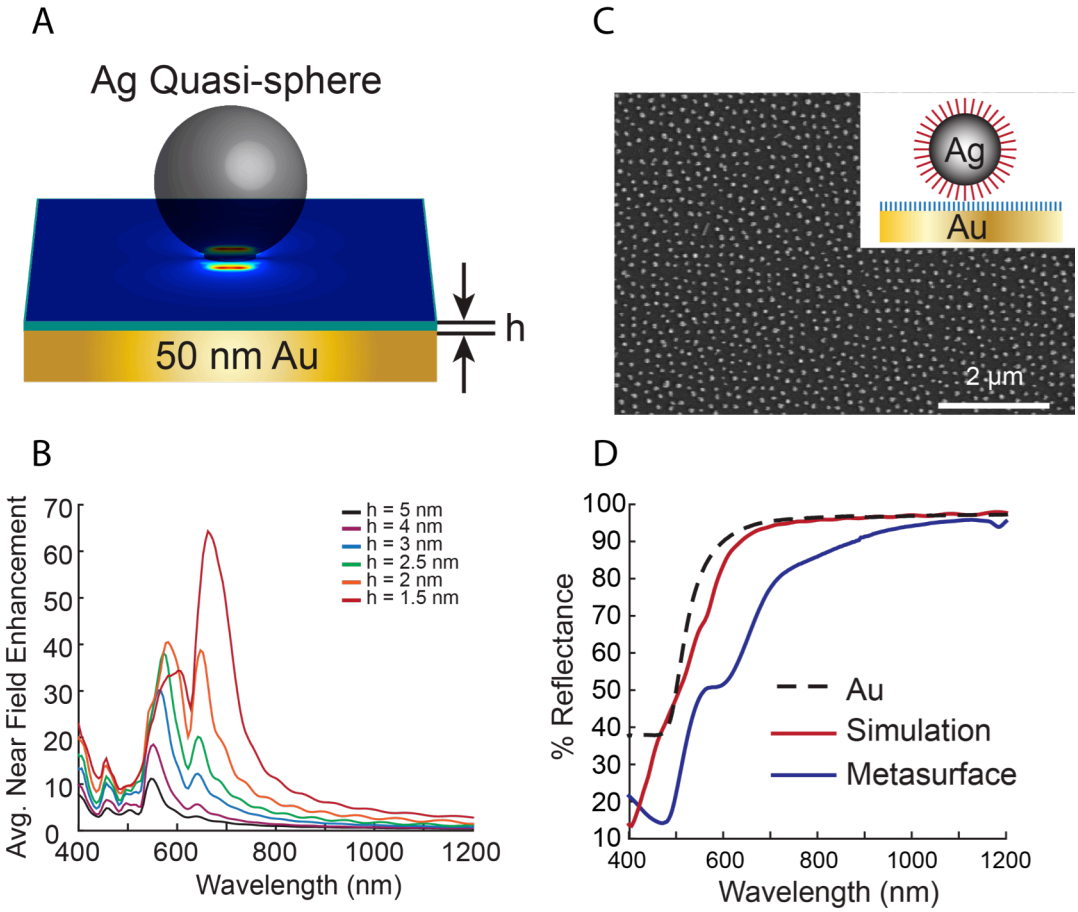

Figure 6.6. FDTD Simulations and reflectance data of a metasurface fabricated from AgNS on an Au thin-film. (A) Schematic showing a sphere separated by a dielectric gap (n=1.4) from an Au substrate by h. (B) Simulated average electric field enhancements within the gap for different values of h. (C) an SEM image showing AgNS deposited onto a PDMS substrate prior to adhesion to an Au thin-film. The AgNS have an average size of 58 ± 12 nm. (D) Reflectance spectra for a fabricated AgNS metasurface with a Raman analyte layer of dHDT and an alkanethiol layer of n=11 (dodecanethiol). The gap is estimated at h = 3 nm, $\sigma_T = 0$ (blue line), the red line shows the FDTD simulated reflectance for h = 3 nm. The dashed line shows the reflectance spectra of PDMS adhered to Au with no AgNCs.

quasi-spheres to reflect the faceted nature of the synthesized AgNS (Figure 6.6.A). Ag quasi-spheres were simulated to include a regular hexagonal facet at the interface with a diameter of 18 nm. The Ag quasi-sphere displays two distinct plasmon resonances (Figure 6.6.B). The higher energy resonance peak position fits well to $1/h^3$, consistent with a dipole-dipole interaction[2]. However, the lower energy resonance peak position

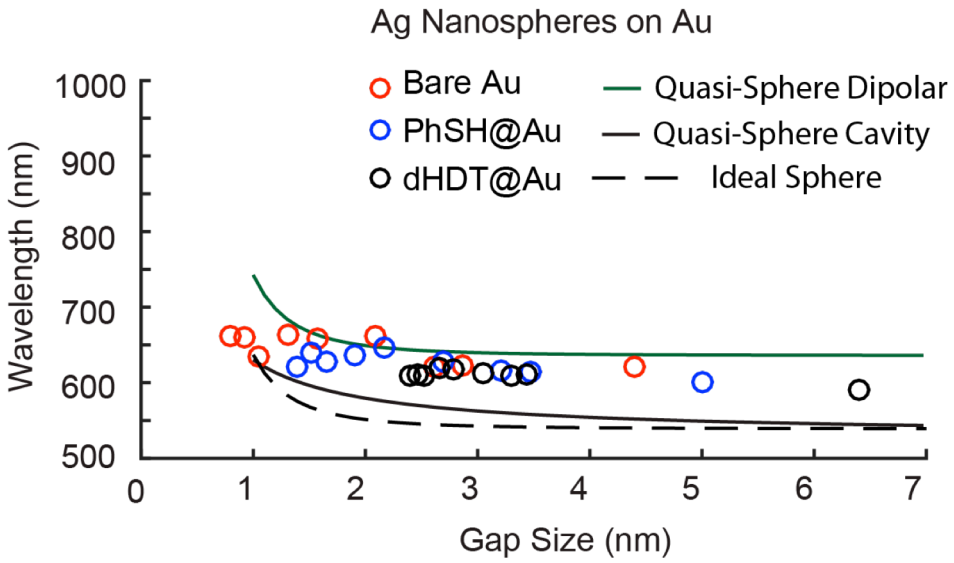

Figure 6.7. Experimentally determined gap-mode resonance (circles) for metasurfaces fabricated from alkanethiol and PVP capped AgNS (n= 1—17) on an Au thin-film substrate with Raman analyte layers of dHDT (black circles), PhSH (blue circles), and bare Au (red circles). The black dashed line shows the reflectance peak determined by the classical model for ideal AgNCs, the black solid line shows the cavity resonance reflectance peak determined for a quasi-sphere, the green solid line shows the dipolar resonance reflectance peak determined for a quasi-sphere.

fits well to $1/d^{1/2}$, consistent with a TCP (a similar mode to the AgNC, although weaker in intensity).[13] We fabricated AgNS metasurfaces (Figure 6.6.C) using spheres of 58 ± 12 nm diameter. As opposed to the AgNC metasurfaces, we observe a monotonically red-shifting resonance with decreasing gap-size down to our smallest gap of 8 Å (Figure 6.7.). These resonances fall between the simulated TCP and dipolar modes of the quasi-sphere. This is likely due to polydispersity of the AgNS and many different possible sizes and shapes of crystalline facet being in contact with the Au substrate. The only observable difference between our AgNC and AgNS metasurfaces are the nanoparticle size and geometry, 58 ± 12 nm diameter for the AgNS and 73.6 ± 3.7 nm the AgNCs. We suspect the primary cause for the increase in gap conductivity is the increased surface area in which there is a uniformly small gap. For an ideal

AgNS, the point of contact is infinitesimal, while for a real AgNS it is likely a crystalline facet lying in contact with the Au thin-film. This facet is small relative to the AgNC face area, we estimate over an order of magnitude difference in most cases. Classical simulations (h = 1.5 nm) indicate that the average near-field enhancement is 81.4 for AgNCs with an interfacial area of 5,400 nm^2. For AgNS we estimate an average near-field enhancement of 38 over an area of 280 nm^2. A larger near-field enhancement over a larger area may enable tunneling in the AgNC metasurface. It is also possible that the plasmon mode plays a role. The fundamental mode for an AgNC metasurface is a TCP, while the AgNS substrate resonance is a dipolar bonding plasmon (DBP).[13] It is possible that the polarity of the plasmon is important to the distance across which plasmons can induce tunneling. A third possibility is that the single crystalline nature of the AgNC allows for better tunneling than the polycrystalline AgNS. Single crystal particles have previously shown longer plasmon decay lifetimes, suggesting a larger population of high energy electrons can exist.[42]

6.2.5. Tunneling Effects on Near-Field Enhancement

We can indirectly measure the effects of tunneling on the near-field enhancement *via* SERS. We took SERS measurements for alkanethiol (n = 1—17) and PVP functionalized AgNC metasurfaces with a RA layer of PhSH, and recorded the intensity of the PhSH ring vibrational mode (999 cm^{-1}). PhSH is constant relative to the changing alkanethiol molecules and so can be used as a gauge for near-field enhancement at a constant distance from the Au substrate. SERS measurements are taken with two different excitation sources 785 and 633 nm in order to ensure

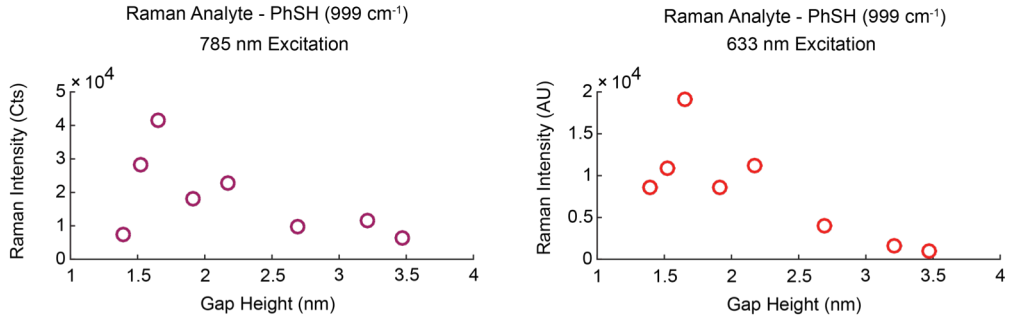

Figure 6.8. Raman intensity for metasurfaes fabricated from alkanethiol capped AgNCs on an Au thin-film with a PhSH Raman analyte layer. The Raman intensity plotted is for the 999 cm^{-1} ring breathing. (A) SERS intensites at 785 nm excitation, and (B) 633 nm excitation.

resonance effects do not become convoluted with near-field strengths. Figure 6.8. show SERS intensities for 785 and 633 nm excitations respectively. For both laser excitations, PhSH intensities increase with decreasing gap size until n = 3, where the SERS intensity rapidly decreases, suggesting a loss of near-field enhancement as the metasurface experiences tunneling. From n = 17 to n = 3 the Raman signal intensity increases 15x for 785 nm excitation and 31x for 633 nm excitation. These results indicate that although a smaller h can provide a higher near-field strength and Raman enhancement factor (EF), the strength of the near-field decreases quickly below a critical h, at which tunneling negatively affects SERS intensity.

6.3 Experimental and Computational Methods

Ag nanocubes and nanospheres were synthesized using the polyol method. Details of the Ag nanocube synthesis can be found in chapter 2. Ag nanosphere synthesis was carried out as previously described.[41] Briefly, 1.28 g of PVP (55000 MW) is dissolved in 50 mL of ethylene glycol and heated to 150° C. The solution is allowed to preheat for 10 min. Under vigorous stirring, 0.2 g of $AgNO_3$ dissolved in

deionized (DI) water is rapidly injected into the PVP solution. After 30 minutes of reaction time the solution is removed from heat and allowed to cool.

Metasurface fabrication: Ag nanoparticles are repeatedly washed by centrifugation in ethanol and finally redispersed in chloroform. The nanoparticle solution is then carefully drop-cast onto a DI water sub-phase and allowed to equilibrate. Thin (150 μm) PDMS adhered to a silicon backing was then mechanically dipped through the film to transfer it to the substrate. Alkanethiols were used to displace the PVP and form controlled SAMs on the nanoparticle surfaces. Nanoparticle coated PDMS surfaces were submerged in a 1 mM ethanolic solution of the desired alkanethiol for 1 hour. They were then rinsed copiously with ethanol, dried in N_2, and adhered immediately to an Au thin-film substrate. The Au thin-film was prepared by DC sputtering a Si substrate with a 10 nm Ti adhesion layer followed by 50 nm of Au. The Au thin-film was then either treated with a 1 mM ethanolic solution of a desired thiolated molecule prior to adhesion to the Ag nanoparticle PDMS surface, or immediately adhered to form the metasurface.

UV-Vis and SERS measurements: a Perkin-Elmer Lambda 1050 was used for all reflectance measurements. Data was collected with an 8° angle of incidence. Raman measurements were collected on a Renishaw inVia Raman microscope, either with a 633 nm HeNe laser or a 785 nm diode laser. All measurements were collected with < 1 mW with a 0.9 NA 50x objective. 100 measurements were collected at random for each substrate.

FDTD Simulations were carried out according to the same procedure described in Chapter 2.

6.4 Conclusions

We have observed quantum tunneling gap distances of up to 2.5 nm, where the critical tunneling distance is tunable by modifying the gap ligand chemistry. This effect is only observed for metasurfaces fabricated with AgNCs, a plasmonic nanostructure with high crystallinity and a large interfacial gap surface area. The quantum tunneling affects not only far-field properties like absorption, but the near-field enhancement as well. By decreasing the metasurface gap to only slightly larger than the critical tunneling gap distance, we have been able to increase SERS intensity by over an order of magnitude. A thorough understanding of the mechanisms that allow electrons to tunnel across the molecular tunnel junction can help to engineer plasmonic systems. It may also be possible to leverage high-energy electrons tunneling across the gap to create high-sensitivity sensors, plasmonic-electronic devices, or photocatalytic reactors.

Chapter 6, in full, is currently being prepared for submission for publication of the material. **Dill, T. J.**., Rodarte, A. L., Tao, A. R. The dissertation author was the principal researcher and author of this material.

6.5 References

1. Mock, J. J.; Hill, R. T.; Degiron, A.; Zauscher, S.; Chilkoti, A.; Smith, D. R., Distance-Dependent Plasmon Resonant Coupling between a Gold Nanoparticle and Gold Film. *Nano Letters* **2008,** *8* (8), 2245-2252.

2. Maier, S., *Plasmonics: Fundamentals and Applications*. 1 ed.; Springer US: 007; p 224.

3. Tao, A.; Sinsermsuksakul, P.; Yang, P., Tunable plasmonic lattices of silver nanocrystals. *Nature nanotechnology* **2007,** *2* (7), 435-40.

4. Pettinger, B.; Domke, K. F.; Zhang, D.; Schuster, R.; Ertl, G., Direct monitoring of plasmon resonances in a tip-surface gap of varying width. *Physical Review B* **2007,** *76* (11), 113409.

5. Fromm, D. P.; Sundaramurthy, A.; Schuck, P. J.; Kino, G.; Moerner, W. E., Gap-Dependent Optical Coupling of Single "Bowtie" Nanoantennas Resonant in the Visible. *Nano Letters* **2004,** *4* (5), 957-961.

6. Kleinman, S. L.; Sharma, B.; Blaber, M. G.; Henry, A.-I.; Valley, N.; Freeman, R. G.; Natan, M. J.; Schatz, G. C.; Van Duyne, R. P., Structure Enhancement Factor Relationships in Single Gold Nanoantennas by Surface-Enhanced Raman Excitation Spectroscopy. *Journal of the American Chemical Society* **2013,** *135* (1), 301-308.

7. Zhang, W.; Yeo, B. S.; Schmid, T.; Zenobi, R., Single Molecule Tip-Enhanced Raman Spectroscopy with Silver Tips. *The Journal of Physical Chemistry C* **2007,** *111* (4), 1733-1738.

8. Zhang, R.; Zhang, Y.; Dong, Z. C.; Jiang, S.; Zhang, C.; Chen, L. G.; Zhang, L.; Liao, Y.; Aizpurua, J.; Luo, Y.; Yang, J. L.; Hou, J. G., Chemical mapping of a single molecule by plasmon-enhanced Raman scattering. *Nature* **2013,** *498* (7452), 82-86.

9. Schlücker, S., Surface-Enhanced Raman Spectroscopy: Concepts and Chemical Applications. *Angewandte Chemie International Edition* **2014,** *53* (19), 4756-4795.

10. Alaee, R.; Menzel, C.; Huebner, U.; Pshenay-Severin, E.; Bin Hasan, S.; Pertsch, T.; Rockstuhl, C.; Lederer, F., Deep-Subwavelength Plasmonic Nanoresonators Exploiting Extreme Coupling. *Nano Letters* **2013,** *13* (8), 3482-3486.

11. Liu, Y.; Zhang, X., Metamaterials: a new frontier of science and technology. *Chemical Society Reviews* **2011,** *40* (5), 2494-2507.

12. Lee, S. Y.; Hung, L.; Lang, G. S.; Cornett, J. E.; Mayergoyz, I. D.; Rabin, O., Dispersion in the SERS Enhancement with Silver Nanocube Dimers. *ACS Nano* **2010,** *4* (10), 5763-5772.

13. Esteban, R.; Aguirregabiria, G.; Borisov, A. G.; Wang, Y. M.; Nordlander, P.; Bryant, G. W.; Aizpurua, J., The Morphology of Narrow Gaps Modifies the Plasmonic Response. *ACS Photonics* **2015,** *2* (2), 295-305.

14. Ciracì, C.; Hill, R. T.; Mock, J. J.; Urzhumov, Y.; Fernández-Domínguez, A. I.; Maier, S. A.; Pendry, J. B.; Chilkoti, A.; Smith, D. R., Probing the Ultimate Limits of Plasmonic Enhancement. *Science* **2012,** *337* (6098), 1072.

15. Mao, L.; Li, Z.; Wu, B.; Xu, H., Effects of quantum tunneling in metal nanogap on surface-enhanced Raman scattering. *Applied Physics Letters* **2009,** *94* (24), 243102.

16. Zhu, W.; Crozier, K. B., Quantum mechanical limit to plasmonic enhancement as observed by surface-enhanced Raman scattering. *Nature Communications* **2014,** *5*, 5228.

17. Zhu, W.; Esteban, R.; Borisov, A. G.; Baumberg, J. J.; Nordlander, P.; Lezec, H. J.; Aizpurua, J.; Crozier, K. B., Quantum mechanical effects in plasmonic structures with subnanometre gaps. *Nature Communications* **2016,** *7*, 11495.

18. Pérez-González, O.; Zabala, N.; Borisov, A. G.; Halas, N. J.; Nordlander, P.; Aizpurua, J., Optical Spectroscopy of Conductive Junctions in Plasmonic Cavities. *Nano Letters* **2010,** *10* (8), 3090-3095.

19. Zuloaga, J.; Prodan, E.; Nordlander, P., Quantum Description of the Plasmon Resonances of a Nanoparticle Dimer. *Nano Letters* **2009,** *9* (2), 887-891.

20. Cha, H.; Yoon, J. H.; Yoon, S., Probing Quantum Plasmon Coupling Using Gold Nanoparticle Dimers with Tunable Interparticle Distances Down to the Subnanometer Range. *ACS Nano* **2014,** *8* (8), 8554-8563.

21. Savage, K. J.; Hawkeye, M. M.; Esteban, R.; Borisov, A. G.; Aizpurua, J.; Baumberg, J. J., Revealing the quantum regime in tunnelling plasmonics. *Nature* **2012,** *491* (7425), 574-577.

22. Hajisalem, G.; Nezami, M. S.; Gordon, R., Probing the Quantum Tunneling Limit of Plasmonic Enhancement by Third Harmonic Generation. *Nano Letters* **2014,** *14* (11), 6651-6654.

23. Scholl, J. A.; García-Etxarri, A.; Koh, A. L.; Dionne, J. A., Observation of Quantum Tunneling between Two Plasmonic Nanoparticles. *Nano Letters* **2013,** *13* (2), 564-569.

24. Wang, T.; Nijhuis, C. A., Molecular electronic plasmonics. *Applied Materials Today* **2016,** *3*, 73-86.

25. Benz, F.; Tserkezis, C.; Herrmann, L. O.; de Nijs, B.; Sanders, A.; Sigle, D. O.; Pukenas, L.; Evans, S. D.; Aizpurua, J.; Baumberg, J. J., Nanooptics of Molecular-Shunted Plasmonic Nanojunctions. *Nano Letters* **2015,** *15* (1), 669-674.

26. Knebl, D.; Hörl, A.; Trügler, A.; Kern, J.; Krenn, J. R.; Puschnig, P.; Hohenester, U., Gap plasmonics of silver nanocube dimers. *Physical Review B* **2016,** *93* (8), 081405.

27. Tan, S. F.; Wu, L.; Yang, J. K. W.; Bai, P.; Bosman, M.; Nijhuis, C. A., Quantum Plasmon Resonances Controlled by Molecular Tunnel Junctions. *Science* **2014,** *343* (6178), 1496.

28. Vadai, M.; Nachman, N.; Ben-Zion, M.; Bürkle, M.; Pauly, F.; Cuevas, J. C.; Selzer, Y., Plasmon-Induced Conductance Enhancement in Single-Molecule Junctions. *The Journal of Physical Chemistry Letters* **2013,** *4* (17), 2811-2816.

29. Tame, M. S.; McEnery, K. R.; Ozdemir, S. K.; Lee, J.; Maier, S. A.; Kim, M. S., Quantum plasmonics. *Nat Phys* **2013,** *9* (6), 329-340.

30. Moreau, A.; Ciraci, C.; Mock, J. J.; Hill, R. T.; Wang, Q.; Wiley, B. J.; Chilkoti, A.; Smith, D. R., Controlled-reflectance surfaces with film-coupled colloidal nanoantennas. *Nature* **2012,** *492* (7427), 86-89.

31. Rose, A.; Hoang, T. B.; McGuire, F.; Mock, J. J.; Ciracì, C.; Smith, D. R.; Mikkelsen, M. H., Control of Radiative Processes Using Tunable Plasmonic Nanopatch Antennas. *Nano Letters* **2014,** *14* (8), 4797-4802.

32. Rozin, M. J.; Rosen, D. A.; Dill, T. J.; Tao, A. R., Colloidal metasurfaces displaying near-ideal and tunable light absorbance in the infrared. *Nat Commun* **2015,** *6*.

33. Dill, T. J.; Rozin, M. J.; Brown, E. R.; Palani, S.; Tao, A. R., Investigating the effect of Ag nanocube polydispersity on gap-mode SERS enhancement factors. *Analyst* **2016,** *141* (12), 3916-3924.

34. Akselrod, G. M.; Argyropoulos, C.; Hoang, T. B.; Ciracì, C.; Fang, C.; Huang, J.; Smith, D. R.; Mikkelsen, M. H., Probing the mechanisms of large Purcell enhancement in plasmonic nanoantennas. *Nat Photon* **2014,** *8* (11), 835-840.

35. Lassiter, J. B.; McGuire, F.; Mock, J. J.; Ciracì, C.; Hill, R. T.; Wiley, B. J.; Chilkoti, A.; Smith, D. R., Plasmonic Waveguide Modes of Film-Coupled Metallic Nanocubes. *Nano Letters* **2013,** *13* (12), 5866-5872.

36. Esteban, R.; Borisov, A. G.; Nordlander, P.; Aizpurua, J., Bridging quantum and classical plasmonics with a quantum-corrected model. *Nature Communications* **2012,** *3*, 825.

37. Saito, K.; Tanabe, I.; Tatsuma, T., Site-Selective Plasmonic Etching of Silver Nanocubes. *The Journal of Physical Chemistry Letters* **2016,** *7* (21), 4363-4368.

38. Wang, F.; Melosh, N. A., Power-independent wavelength determination by hot carrier collection in metal-insulator-metal devices. *Nature Communications* **2013,** *4*, 1711.

39. York, R. L.; Nguyen, P. T.; Slowinski, K., Long-Range Electron Transfer through Monolayers and Bilayers of Alkanethiols in Electrochemically Controlled Hg−Hg Tunneling Junctions. *Journal of the American Chemical Society* **2003,** *125* (19), 5948-5953.

40. Liang, H.; Wang, W.; Huang, Y.; Zhang, S.; Wei, H.; Xu, H., Controlled Synthesis of Uniform Silver Nanospheres. *The Journal of Physical Chemistry C* **2010,** *114* (16), 7427-7431.

41. Dongjo Kim and Sunho Jeong and Jooho, M., Synthesis of silver nanoparticles using the polyol process and the influence of precursor injection. *Nanotechnology* **2006,** *17* (16), 4019.

42. Huang, W.; Qian, W.; El-Sayed, M. A.; Ding, Y.; Wang, Z. L., Effect of the Lattice Crystallinity on the Electron−Phonon Relaxation Rates in Gold Nanoparticles. *The Journal of Physical Chemistry C* **2007,** *111* (29), 10751-10757.

Appendix A

Colloidal Nanoantenna Data

Table S3: Data from Individual TERS Nanoantenna

Tip #	Wavelength (nm)	Spectra #	Peak (cm^-1)	Noise	Peak Height	SNR	Int time (s)	lPower (nW)	EF (Probe Average) Normalized SNR
1	633	1	999	23.7	1690.1	71.31	10	8.00E+05	1.40E+07
1	633	2	999	25.9	780.7	30.14	10	8.00E+05	179
1	633	3	999	37.6	1447	38.48	10	8.00E+05	
2	633	1	999	90.82	2131.4	23.47	10	8.00E+05	2.61E+07
2	633	2	999		3077.31		10	8.00E+05	95
2	633	3	999	98.1	1481.5	15.10	10	8.00E+05	
2	633	4	999	86.89	3081.3	35.46	10	8.00E+05	
3	633	1	999	45.2	821.3	18.17	10	4.00E+05	2.28E+07
3	633	2	999	52.7	1267.6	24.05	10	4.00E+05	296
3	633	3	999	50.7	1189	23.45	10	4.00E+05	
3	633	4	999	59.29	5256	88.65	10	4.00E+05	
4	633	1	999	73.1	5457.3	74.66	10	4.00E+05	5.03E+07
4	633	2	999	78	5896.3	75.59	10	4.00E+05	553
4	633	3	999	80.3	5503.9	68.54	10	4.00E+05	
4	633	4	999	27.9	1951.8	69.96	10	4.00E+05	
5	633	1	999	15.32	533	34.79	10	4.00E+05	8.12E+06
5	633	2	999	15.7	480	30.57	10	4.00E+05	325
5	633	3	999	18.4	510	27.72	10	4.00E+05	
5	633	4	999	19.8	320	16.16	10	4.00E+05	

5	633	5	999	17.5	854	48.80	10	4.00E+05	
5	633	6	999	16.4	968	59.02	10	4.00E+05	
5	633	7	999	20.6	1650	80.10	10	4.00E+05	
6	633	1	999	21.5	926	43.07	10	4.00E+05	1.07E+07
6	633	2	999	21	1761	83.86	10	4.00E+05	365
6	633	3	999	20.8	368	17.69	10	4.00E+05	
6	633	4	999	16.1	362	22.48	10	4.00E+05	
6	633	5	999	16.5	571	34.61	10	4.00E+05	
6	633	6	999	23	1961	85.26	10	4.00E+05	
6	633	7	999	24	877	36.54	10	4.00E+05	
6	633	8	999	20.5	1181	57.61	10	4.00E+05	
7	633	1	999	26.6	346	13.01	10	4.00E+05	3.88E+06
7	633	2	999	28.8	368	12.78	10	4.00E+05	118
7	633	3	999	24.3	183	7.53	10	4.00E+05	
7	633	4	999	23.3	269	11.55	10	4.00E+05	
7	633	5	999	23.4	376	16.07	10	4.00E+05	
7	633	6	999	24.5	371	15.14	10	4.00E+05	
7	633	7	999	19.9	626	31.46	10	4.00E+05	
8	633	1	999	18.3	661.5	36.15	10	4.00E+05	1.00E+07
8	633	2	999	16.2	401.4	24.78	10	4.00E+05	286
8	633	3	999	33.8	1731.6	51.23	10	4.00E+05	
9	633	1	999	14.8	130.2	8.80	10	4.00E+05	1.39E+06
9	633	2	999	14	126.3	9.02	10	4.00E+05	66
9	633	3	999	15.3	189.6	12.39	10	4.00E+05	

9	633	4	999	17.1	124	7.25	10	4.00E+05	
9	633	5	999	15.9	129	8.11	10	4.00E+05	
9	633	6	999	15.8	85	5.38	10	4.00E+05	
9	633	7	999	12.9	102.7	7.96	10	4.00E+05	
9	633	8	999	16	155.5	9.72	10	4.00E+05	
10	633	1	999	17.74	143.5	8.09	10	4.00E+05	2.84E+06
10	633	2	999	14	239.5	17.11	10	4.00E+05	141.1
10	633	3	999	14.4	453.7	31.51	10	4.00E+05	
10	633	4	999	16	165.1	10.32	10	4.00E+05	
10	633	5	999	12.9	323.8	25.10	10	4.00E+05	
11	633	1	999	14.3	303	21.19	5	4.00E+05	5.90E+06
11	633	2	999	17.5	265	15.14	5	4.00E+05	240
11	633	3	999	24.1	518	21.49	10	4.00E+05	
12	633	1	999	31.76	4266	134.32	10	4.00E+05	3.13E+07
12	633	2	999	37.22	2392	64.27	10	4.00E+05	667
12	633	3	999	33.7	2114	62.73	10	4.00E+05	
13	633	1	999	16.5	855.7	51.86	5	4.00E+05	1.77E+07
13	633	2	999	15.6	844	54.10	5	4.00E+05	871
13	633	3	999	13	808	62.15	5	4.00E+05	
13	633	4	999	13.5	800	59.26	5	4.00E+05	
14	785	1	999	21.6	1975	91.44	10	8.00E+05	6.78E+08
14	785	2	999	20.2	2970	147.03	10	8.00E+05	608.4
14	785	3	999	21.4	3278	153.18	10	8.00E+05	

14	785	4	999	21.1	1536	72.80	10	8.00E+05	
14	785	5	999	26.6	2232	83.91	10	8.00E+05	
14	785	6	999		2648	#DIV/0!	10	8.00E+05	
14	785	7	999	26.7	1904	71.31	10	8.00E+05	
15	514	1	999		28		30	38000	1.46E+06
15	514	2	999		25				NA
15	514	3	999	11.98	38	3.17	30	38000	
15	785	1	999	43.9	1977	45.03	10	8.00E+05	5.34E+08
15	785	2	999	30.7	1068	34.79	10	8.00E+05	296
15	785	3	999	30.8	1584	51.43	10	8.00E+05	
15	785	4	999	37.4	2615	69.92	10	8.00E+05	
15	633	1	999	17	440	25.88	10	8.00E+04	1.33E+07
15	633	2	999	15.8	336	21.27	10	8.00E+04	871
15	633	3	999	11.87	386	32.52	10	8.00E+04	
15	633	4	999	17.21	195	11.33	10	8.00E+04	
16	633	1	999	15	106	7.07	10	8.00E+04	2.79E+06
16	633	2	999	12.4	92	7.42	10	8.00E+04	281
16	633	3	999	11.7	78	6.67	10	8.00E+04	
16	633	4	999	12.6	103	8.17	10	8.00E+04	
16	785	1	999	31	2428	78.32	10	8.00E+05	4.99E+08
16	785	2	999	29.5	2715	92.03	10	8.00E+05	502
16	633	1	999	14.4	135	9.38	10	8.00E+04	3.61E+06

									415
16	633	2	999	10.5	129	12.29	10	8.00E+04	Average of 4 spectra (used for EF)
16	785	1	999	21	1022	48.67	10	8.00E+05	2.64E+08
16	785	2	999	25	816	32.64	10	8.00E+05	240
17	785	1	999	27.8	873	31.40	10	1.50E+05	1.91E+09
17	785	2	999	34.9	12554	359.71	10	1.50E+05	986
17	785	3	999	28.6	5190	181.47	10	1.50E+05	
17	785	4	999	42.3	19250	455.08	10	1.50E+05	
17	785	5	999	77.2	9126	118.21	10	1.50E+05	
17	785	6	999	37.7	20425	541.78	10	1.50E+05	
18	785	1	999	19.7	1002	50.86	10	1.60E+05	2.65E+09
18	785	2	999	21.3	845	39.67	10	1.60E+05	1333
19	785	1	999	14.4	1666.8	115.75	10	1.60E+05	3.95E+09
19	785	2	999	10.6	1921	181.23	1	8.00E+05	7043
20	785	1	999	37	771	20.84	10	8.00E+05	3.63E+08
20	785	2	999	22	750.1	34.10	10	8.00E+05	363
20	785	3	999	18	1100	61.11	10	8.00E+05	
20	785	4	999	19	2915	153.42	10	8.00E+05	
20	785	5	999	20.5	794	38.73	10	8.00E+05	
21	785	1	999	21.9	466.4	21.30	10	8.00E+05	1.01E+08
21	785	2	999	25.24	236	9.35	10	8.00E+05	111

21	785	3	999	19	330	17.37	10	8.00E+05	
21	785	4	999	15	398	26.53	10	8.00E+05	
21	785	5	999	16.6	323.5	19.49	10	8.00E+05	
22	785	1	999	54	15856	293.63	10	8.00E+05	2.82E+09
22	785	2	999	26	1588	61.08	10	8.00E+05	1266
22	785	3	999	85.7	15673	182.88	10	8.00E+05	
22	785	4	999	30.6	7881	257.55	10	8.00E+05	
22	785	5	999	28.9	8062	278.96	10	8.00E+05	
23	785	1	999	25.6	631	24.65	10	8.00E+05	9.61E+08
23	785	2	999	27.1	2159	79.67	10	8.00E+05	771
23	785	3	999	30.8	5639	183.08	10	8.00E+05	
23	785	4	999	26	3646	140.23	10	8.00E+05	
23	785	5	999	20.6	4668	226.60	10	8.00E+05	
24	785	1	999	23.9	2920	122.18	10	8.00E+05	3.43E+08
24	785	2	999	24.9	769	30.88	10	8.00E+05	351
24	785	3	999	13.4	1006	75.07	10	8.00E+05	
24	785	4	999	20.6	6564	318.64	10	8.00E+05	
24	785	5	999	16.6	6214	374.34	10	8.00E+05	
25	785	1	999	23.1	702	30.39	10	8.00E+05	4.78E+08
25	785	2	999	27	5256	194.67	10	8.00E+05	375
25	785	3	999	25.4	1322	52.05	10	8.00E+05	
25	785	4	999	27.8	5275	189.75	10	8.00E+05	
25	785	5	999	23.2	5214	224.74	10	8.00E+05	

26	785	1	999	18.45	1079	58.48	10	8.00E+05	8.29E+08
26	785	2	999	21.18	1065	50.28	10	8.00E+05	786
26	785	3	999	22.8	592	25.96	10	8.00E+05	
26	785	4	999	22.6	7132	315.58	10	8.00E+05	
26	785	5	999	21.1	4581	217.11	10	8.00E+05	
27	785	1	999	29	1163	40.10	10	8.00E+05	2.40E+08
27	785	2	999	22.6	473	20.93	10	8.00E+05	192
27	785	3	999	23	557	24.22	10	8.00E+05	
27	785	4	999	27	1562	57.85	10	8.00E+05	
27	785	5	999	21.8	435	19.95	10	8.00E+05	